A Search for Supersymmetry and Universal Extra Dimensions in Final States with Three Leptons and Missing Transverse Momentum in 20.7 fb^{-1} of $\sqrt{s}$ =8 TeV pp Collisions with the ATLAS Detector

by

Samuel King

BSc, McGill University, 2009

A THESIS SUBMITTED IN PARTIAL FULFILLMENT
OF THE REQUIREMENTS FOR THE DEGREE OF

Doctor of Philosophy

in

THE FACULTY OF GRADUATE AND POSTDOCTORAL STUDIES
(Physics)

The University Of British Columbia
(Vancouver)

April 2014

© Samuel King, 2014

Abstract

This dissertation presents a search for direct production of charginos and neutralinos in final states with three leptons and missing transverse momentum in 20.7 fb^{-1} of $\sqrt{s}$ =8 TeV proton-proton collisions delivered by the Large Hadron Collider and collected with the ATLAS detector. The Standard Model augmented with the minimal formulation of universal extra dimensions (MUED) is phenomenologically similar to supersymmetry. This search is also sensitive to MUED cascades characterized by the presence of n =1 Kaluza-Klein excitations of Standard Model W and Z bosons. No significant excess over Standard Model predictions is observed. The results are interpreted in the context of simplified supersymmetric models and MUED. New limits are set at the 95% confidence level on the parameter spaces of these models.

Preface

Because of the immense complexity of the Large Hadron Collider (LHC) and A Toroidal LHC Apparatus (ATLAS), it is necessary that all ATLAS physics analyses are collaborative endeavors. This includes the analysis presented herein. The author played a key role in almost all aspects of the analysis: signal region optimization, Monte Carlo-based background estimation, calculation of uncertainties, and the statistical interpretation of the results.

The work would not have been possible, however, without major contributions from colleagues and advisors. The present iteration of the analysis was led by Zoltan Gecse (UBC) and Tina Potter (Sussex). Steve Farrell (UCI) provided the reducible background estimate and was largely responsible for implementing the SUSYNT framework used for data analysis. Sigve Haug, Basil Schneider, and Lukas Marti (Bern) were instrumental in writing useful scripts for performing limit calculations using the HistFitter software. Stewart Martin-Haugh (Sussex) provided help with systematics computations as well as final signal region plots with full systematics. All other work presented herein has been primarily performed by the author.

Earlier iterations of the analysis were performed with smaller datasets [1] [2] [3], and the author contributed to all of these. A public report on the present analysis exists as an ATLAS conference note [4]. The minimal universal extra dimensions interpretation is entirely the work of the author and is not found in any publication, although a smaller dataset interpretation in this model was performed by the author for an ATLAS conference note [5].

Table of Contents

List of Tables

List of Figures

Glossary

ADD	Arkani-Hamed–Dimopoulos–Dvali
ATLAS	A Toroidal LHC Apparatus
BG	background
BKT	brane kinetic term
BSM	beyond the Standard Model
CDF	cumulative distribution function
CERN	The European Organization for Nuclear Research
CL	confidence level
CM	center of mass
CMS	Compact Muon Solenoid
CSC	cathode strip chambers
DGP	Dvali-Gabadadze-Porrati
ECal	electromagnetic calorimeter
EF	event filter
EFE	Einstein field equations
EW	electroweak

EWSB	electroweak symmetry breaking
FCal	forward calorimeter
GR	General Relativity
GRL	good runs list
HCal	hadronic calorimeter
HEC	hadronic endcap
HF	heavy flavor
ID	inner detector
IP	interaction point
ISR	initial state radiation
JVF	jet vertex fraction
KK	Kaluza-Klein
LAr	liquid argon
LEP	Large Electron-Positron Collider
LF	light flavor
LHC	Large Hadron Collider
LKP	lightest Kaluza-Klein particle
LO	leading order
LSP	lightest supersymmetric particle
MC	Monte Carlo
MDT	monitored drift tubes
MLE	maximum likelihood estimator

MSSM	minimal supersymmetric Standard Model
MUED	minimal universal extra dimensions
NLO	next-to-leading order
NNLO	next-to-next-to-leading order
PDF	parton distribution function or probability density function
PV	primary vertex
QCD	quantum chromodynamics
QFT	quantum field theory
RF	radio frequency
ROI	region of interest
RPC	R-parity conserving supersymmetry or resistive plate chambers
RS	Randall-Sundrum
SCT	semiconductor tracker
SFOC	same flavor—opposite charge
SIM	simplified model
SM	Standard Model
SSB	spontaneous symmetry breaking
STM	space-time-matter
SPS	Super Proton Synchrotron
SR	signal region
SUSY	supersymmetry
TDAQ	trigger and data acquisition

TGC	thin gap chambers
TRT	transition radiation tracker
VEV	vacuum expectation value
VR	validation region
WIMP	weakly interacting massive particle
WMAP	Wilkinson Microwave Anisotropy Probe
XD	extra dimensions

Acknowledgments

Working within the ATLAS Collaboration has been a rewarding and eye-opening experience. There are so many collaborators worthy of thanks that it would be impractical to list them all here. I must first thank my advisors, Colin and Anadi, for their tireless help and guidance. I also extend a hearty thanks to Zoltan and Tina for their countless words of wisdom and enlightening discussions (often at 4:30 am on Skype).

I am endlessly indebted to my family, Mark, Laura, and Hannah, without whom this thesis would not exist. I thank the beautiful Karly for putting up with the then-seemingly endless nights featuring yours truly hunched over a laptop, and my best bro Josh for being a great, robust pal.

I would be remiss if I didn't mention the friends I've made in the UBC ATLAS lab: Stephen Swedish, Bill Mills, Simon Viel, Chang Wei Loh, Arash Khazraie, Matt Gignac, and Ricardo Chávez-González. All of you guys played a key role in shaping my "Ph.D. experience" and you will not soon be forgotten.

Finally, I'd like to thank Klaus Kinski, The Stone Roses, Brian De Palma, Teenage Fanclub, Slowdive, Dario Argento, Béla Tarr, The Jesus and Mary Chain, Andrei Tarkovsky, Claudio Simonetti, Small Black, John Carpenter, Hash Jar Tempo, Lilys, and Ian "Shotgun" Jones for helping to make life more palatable.

Chapter 1

Introduction

It is an exciting era for particle physics. The 2009 turn-on of the LHC at the European Organization for Nuclear Research (CERN) has enabled proton-proton (pp) collisions with center of mass (CM) energies as high as $\sqrt{s} = 8$ TeV. By 2015, this is expected to increase to almost 14 TeV. This unprecedented energy scale has enabled particle physicists working within the ATLAS and Compact Muon Solenoid (CMS) collaborations to discover a new boson which, at the time of this writing, is in agreement with the Standard Model (SM) Higgs hypothesis [6] [7].

While discovery of a Higgs boson is surely the triumph of these early days of the LHC, it is possible that discovery of phenomena beyond the Standard Model (BSM) is imminent. There has been much speculation from the theory community since the 1970s as to what shape this "new physics" may take. The work in this dissertation is focused on particular instances of two of the most popular classes of BSM physics hypotheses: supersymmetry (SUSY) and extra dimensions (XD). Of course, a wide range of other BSM scenarios have been proposed. These include, but are not limited to, compositeness (*e.g.* technicolor), little Higgs models, heavy exotic resonances, and hidden sector models. A detailed theoretical overview summarizing the state of the field has been compiled by Morrissey *et al.* [8].

Both ATLAS and CMS, as well as the other LHC-based detector collaborations and many other notable worldwide particle physics experiments, have devised and implemented sophisticated programs to facilitate potential BSM discoveries. Indeed, with so much effort from so many involved parties, discovering phenomena for which the Standard Model cannot account has become the holy grail of experimental particle physics.

To this end, the present work will elucidate a search for new physics in final states characterized by three light, charged leptons ($e^\pm$, $\mu^\pm$) and missing transverse momentum ($\not\!\!E_T$). This final state has been chosen principally because multilepton production is a rare process at hadron colliders and the SM backgrounds are therefore small. The analysis, performed on 20.7 fb^{-1} of 8 TeV pp collisions collected by ATLAS, is optimized for and subsequently interpreted in electroweak (EW) SUSY and minimal universal extra dimensions (MUED). In the SUSY case, the desired final state is produced by cascade decays of directly produced charginos and neutralinos. MUED produces this final state via cascades involving excited states of SM W and Z bosons. Motivation for this work, as well as further details clarifying the exact models under consideration, will be provided in the next chapter.

This thesis constitutes a re-optimized, higher energy or luminosity update of three previous ATLAS searches to which the author contributed substantially [1] [2] [3]; supporting documentation can be found in an ATLAS conference note [4]. It should also be emphasized that this thesis presents the first search for MUED in the trilepton final state with 8 TeV LHC data.

Previous collider searches for MUED have been performed at both the Tevatron [9] and LHC [10]. The most stringent of these is a 2013 ATLAS dilepton search [11] which has placed a 95% CL lower bound on the inverse length of the extra dimension $R^{-1} \gtrsim 900$ GeV. Cosmic microwave background data collected by the Wilkinson Microwave Anisotropy Probe (WMAP) have been used to set an upper bound $R^{-1} \lesssim 1.4$ TeV [12]. These existing limits strongly constrain the available MUED parameter space.

Many previous searches for EW SUSY have been performed both in the trilepton [13] [14] and various other channels [15] [16] [17]. Of these searches, the 2013 iteration of the trilepton analysis performed by CMS is directly comparable to (and most competitive with) the work in this thesis. A much weaker but less model–dependent limit was also set by various collaborations previously working with the precision electroweak data delivered by the Large Electron-Positron Collider (LEP) $m_{\tilde{\chi}_1^\pm} \gtrsim 103.5$ GeV [18]. Note that a further optimized trilepton search using 20.7 fb^{-1} is currently in preparation by ATLAS.

Chapter 2

Theoretical Preliminaries

This chapter will provide a basic overview of qualitative theoretical concepts. The Standard Model is the keystone for all contemporary particle physics; this will be reviewed first. MUED is then presented as a straightforward extension of the SM. Finally, a discussion of SUSY will be provided. Each of these topics are associated with vast literatures, so the focus will be on details relevant for the present search. Motivation for studying both aforementioned BSM scenarios will be recounted.

2.1 The Standard Model of Particle Physics

The Standard Model arose from the work of theorists in the 1960s [19] [20]. This model describes the strong and EW interactions as a non-Abelian gauge theory with gauge group $SU(3)_c \times SU(2)_L \times U(1)_Y$. Here "$c$" refers to quantum chromodynamics (QCD), "L" indicates the chirality of the weak force, and "Y" is a reminder that this $U(1)$ factor is associated with weak hypercharge rather than electric charge. The SM describes a universe wherein the fundamental interactions of fermionic matter fields are mediated by gauge bosons. A schematic [21] outlining the particle content of the SM is shown in figure 2.1.

In the many years since its conception, the predictive power of the SM has

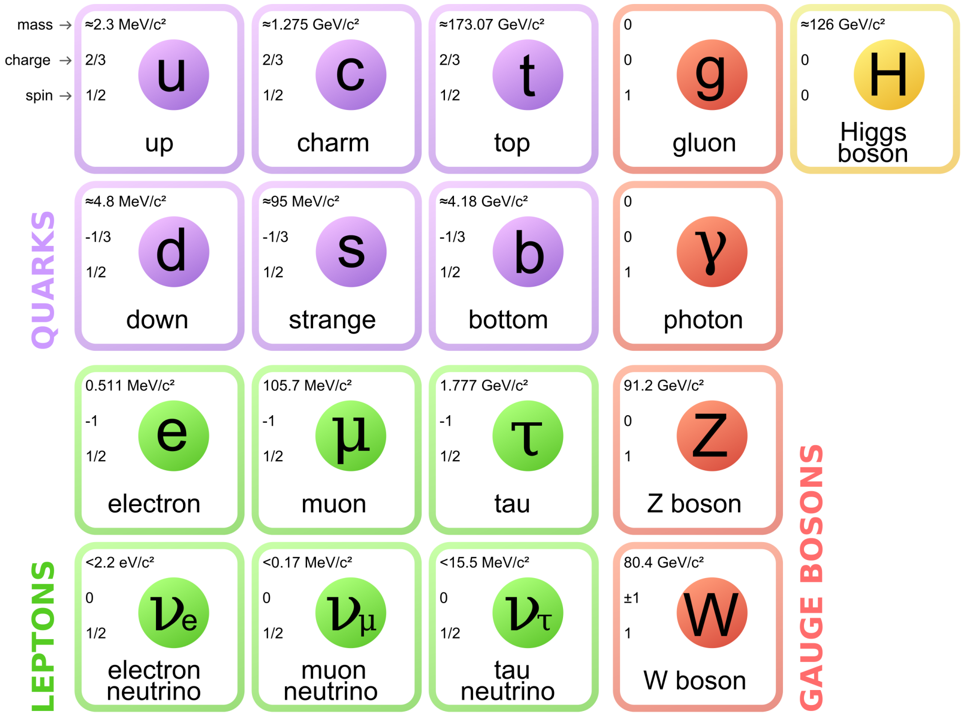

Figure 2.1: A schematic illustrating the fundamental particle content of the SM.

been subjected to myriad experimental tests. With the noteworthy exception of neutrino oscillations (see, *e.g.*, recent T2K $\nu_\mu - \nu_e$ results [22]), the theory has proven to be remarkably robust. Indeed, the history of experimental particle physics in the latter half of the twentieth century is summarized by recalling the most famous of these experiments. Deep inelastic scattering experiments at SLAC in the late 1960s [23] provided evidence for hadronic substructure in the form of light flavor quarks. Gluons and the W/Z bosons were discovered and characterized in the 1970s and '80s at DESY [24] and CERN [25], respectively. In 1995, the top quark was discovered at Fermilab's Tevatron [26]. Most recently, a particle which so far agrees with the SM Higgs boson hypothesis was discovered by ATLAS [6] and CMS [7], thereby completing the spectrum of figure 2.1.

It is clear that these experimental triumphs would be meaningless without a corresponding theoretical framework in which to understand them. As with any gauge theory, the first concrete step towards such a framework is writing down a Lagrangian. The pre-spontaneous symmetry breaking (SSB) SM Lagrangian density can be written in the following highly condensed but convenient form [27]:

$$\mathcal{L}_{SM} = -\frac{1}{4}F_{i\mu\nu}F_i^{\mu\nu} + i\bar{\psi}\not{D}\psi + \psi_i y_{ij}\psi_j\phi + h.c. + |D_\mu\phi|^2 - V(\phi) \tag{2.1}$$

This Lagrangian, symmetric under local $SU(3)_c \times SU(2)_L \times U(1)_Y$ gauge transformations, is most easily understood by considering each term in turn. First note that $F_i^{\mu\nu}$ with gauge index $i = 1, 2, 3$ are the gauge boson field strengths. In the second operator (understood implicitly as a sum of similar operators), the gauge covariant derivatives D_μ are used to describe fermonic (ψ) and scalar (ϕ) kinetic terms and interactions via gauge bosons. Each y_{ij} with generational indices $i, j \in \{1, 2, 3\}$ is a Yukawa coupling encoding the interactions between fermions and the scalar Higgs field ϕ. Note that the convention of using Weyl fermions has been adopted here; more will be said about this below. The final two terms encapsulate Higgs—gauge boson and Higgs self-interactions, respectively.

Since it will be useful later, it is a convenient time to recall the general definition of a gauge covariant derivative in quantum field theory:

$$D_\mu \equiv \partial_\mu - igA_\mu^a T^a, \tag{2.2}$$

where g is the coupling constant associated with the vector A_μ^a and the generator T^a of the relevant Lie algebra. The SM gauge group, and therefore Lie algebra, is $8 + 3 + 1 = 12$-dimensional, and the T_{SM}^a can conveniently be taken to be the tensor products of the generators λ^b (σ^c, s) of $SU(3)$

$(SU(2), U(1))$:

$$T^a_{SM} \in \{\lambda^{1,\ldots,8} \otimes I_{SU(2)} \otimes 1, I_{SU(3)} \otimes \sigma^{9,10,11} \otimes 1, I_{SU(3)} \otimes I_{SU(2)} \otimes s\}. \quad (2.3)$$

While its precision is appealing, thinking in terms of this sort of language requires usage of many indices or tensor products when it comes time to write invariant Lagrangian terms like those in equation 2.1. Flavor, gauge, spinor, generation, and Lorentz indices will therefore be suppressed in this thesis whenever it is possible to do so without sacrificing clarity.

In its simplest formulation, the Higgs mechanism is a process by which $SU(2)_L \times U(1)_Y$ EW symmetry is spontaneously broken to $U(1)$. This breaking occurs because the vacuum state of the Higgs potential $V(\phi)$ does not share the symmetry of the Lagrangian. In this way the $W^\pm$ and Z are imbued with mass, while the photon remains massless [28] [29]. It's important to note that the fermions in equation 2.1 are massless. Inserting typical fermionic mass terms of the form $-m_\psi \bar{\psi}\psi$ would violate gauge invariance. In particular, such an operator mixes L and R fermion chiralities in a way which does not respect $SU(2)_L$ symmetry [27]. It turns out [30] that the Higgs mechanism allows desired mass terms of this form to emerge, where the masses are proportional to the Higgs vacuum expectation value (VEV) $m_\psi \propto$ VEV. The constants of proportionality are y_{ij}. With the renormalizable [31] SM Lagrangian in place, it is then a straightforward endeavor to perturbatively derive a computationally useful set of associated Feynman rules.

This formulation of the SM (with modifications to accommodate small neutrino masses [32]) has proven to be sufficiently robust so as to account for the results of all subatomic physics experiments to date. Although this is an impressive theoretical achievement, the SM provides no answers to a number of difficult open questions; those which are most relevant to the present analysis will now be mentioned.

It was Zwicky [33] who first postulated the existence of unseen dark matter (DM) based upon then–anomalous galactic rotation curve behavior. According to the latest Planck results [34], the universe is comprised of 26.8% DM. It is therefore no surprise that characterizing DM is one of the key open problems in both particle physics and cosmology. A wide variety of candidates have emerged from the theory community, but the most commonly accepted hypothesis classifies DM as a weakly interacting massive particle (WIMP). Although the SM offers no suitable WIMPs, it will be shown below that both SUSY and MUED do.

The ultimate project of fundamental physics is to write down a natural theory which explains all known interactions. Unfortunately, when the SM couplings are run up to large energies, nowhere do they converge to a single, "grand unified" value. Prediction of grand unification is a necessary (but not sufficient) condition for a candidate fundamental theory.

Perhaps the most glaring reminder that the SM is indeed not a theory of everything is its failure to model gravitation. Attempts to quantize General Relativity (GR) via a spin-2 boson, the graviton, lead to a classic example of non-renormalizability in QFT. Several approaches to rectifying this situation (*e.g.* string theory) are under investigation by theorists.

One of the most intriguing open questions in high energy physics is the hierarchy problem [35]. This pertains to the poorly understood 15-order-of-magnitude discrepancy between the EW and Planck scales. As a problem which threatens naturalness, its solution is of particular importance for aesthetically pleasing BSM scenarios. Naturalness is the idea that a maximally beautiful physics theory is one wherein a minimum amount of "fine-tuning" has been performed on its parameters. This means that aesthete physicists should be skeptical of a model whose parameters require arbitrary, extremely specific values to give agreement with experiments—or, worse still, to even make sense at all. Potential solutions to all of these problems will be discussed in the context of SUSY and MUED below.

2.2 Minimal Universal Extra Dimensions

This section begins with an overview of TeV scale extra dimensions in particle physics. Pertinent features (mass spectrum, loop structure, *etc.*) of MUED will then be explored in some detail.

2.2.1 TeV Scale Extra Dimensions

In most areas of physics it is usually assumed that our universe is (3+1)-dimensional. Certainly this is the case in the SM and GR. Nearly a century ago this assumption was notably challenged by the seminal work of Nordström [36], Kaluza [37], and Klein [38]. The famous contribution of these authors was a unification of two classical field theories, GR and classical electrodynamics, via an extra spatial dimension. Details of this are explored below. After a period of dormancy, interest in extra dimensions was renewed towards the end of the twentieth century when string theory began its rise to prominence. Additional dimensions in stringy models, however, are highly compactified and therefore impractical for discovery at LHC energies.

For completeness, it is worth mentioning in passing that theories incorporating extra timelike dimensions have been explored in the literature [39]. These exotic models will not be considered in this thesis, and the word "dimension" should be understood to mean "spacelike dimension" in all that follows.

It is natural at this stage to wonder what benefits may be obtained by considering extra dimensions. It turns out [40] that model builders have been able to address a surprisingly large number of important questions in this way. Perhaps the most important motivation is that XD scenarios often provide natural dark matter candidates. Many models also suggest elegant solutions to the hierarchy problem. These considerations will be explored further below.

Kaluza-Klein Theory

As mentioned above, the first fruitful attempt to employ XD as a unification mechanism dates back to the work of Kaluza and Klein in the 1920s. Since the terminology and philosophy of this work remain useful today, its basic principles will be outlined before turning to modern developments.

Recall that in GR a line element is defined as

$$ds^2 \equiv g_{\mu\nu}(x)dx^\mu dx^\nu, \tag{2.4}$$

where $g_{\mu\nu}$ is the metric tensor (a field on the 4D spacetime manifold) and x^μ are the spacetime coordinates. Kaluza's physical insight was to extend this definition by allowing spacetime to be 5-dimensional:

$$d\hat{s}^2 \equiv \hat{g}_{MN}(x)dx^M dx^N, \tag{2.5}$$

where the coordinates now specify points on a 5D manifold ($M, N \in \{0, ..., 4\}$), and the new metric $\hat{g}_{MN}$ is given in terms of $g_{\mu\nu}$, the electromagnetic 4-potential A_μ, a scalar radion field Φ, and Newton's constant G:

$$\hat{g}_{MN} = \begin{pmatrix} g_{\mu\nu} + 16\pi G\Phi^2 A_\mu A_\nu & 4\sqrt{\pi G}\Phi^2 A_\mu \\ 4\sqrt{\pi G}\Phi^2 A_\nu & \Phi^2 \end{pmatrix}. \tag{2.6}$$

As with any XD scenario, an explanation as to why all previous experiments—and day-to-day human perceptions—agree with the hypothesis that the universe is (3+1)-dimensional is in order. Kaluza's only recourse was simply to assume that the 5th dimension differential operator ∂_4 annihilates all of the fields appearing in equation 2.6, so that physics is effectively 4D. This framework provides a unified description of classical electrodynamics and GR in the sense that the Einstein field equations (EFE) and the Maxwell equations can be recovered if the 5-dimensional EFE are assumed to take a source-free form

$$\hat{R}_{MN} - \frac{\hat{R}}{2}\hat{g}_{MN} = 0, \tag{2.7}$$

where $\hat{R}_{MN}$ is the 5D Ricci tensor, and $\hat{R}$ is the 5D Ricci scalar.

This framework was later quantized by Klein, who realized that the 5th dimension could be "hidden" by compactifying it on a sufficiently small topology. His proposal was a spacetime which factorizes as $R^4 \times S^1$, where R^4 is a 4D manifold and S^1 is a circle of radius R. Denote the coordinates on $R^4 \times S^1$ by $(x^\mu, \alpha) \equiv (x, \alpha)$. It is reasonable to demand that physical tensor fields $f_{\mu\ldots\nu}(x,\alpha)$ satisfy a periodic boundary condition: $f_{\mu\ldots\nu}(x, \alpha + 2\pi R) = f_{\mu\ldots\nu}(x,\alpha)$. Fields on such a spacetime then admit Fourier mode expansions:

$$f_{\mu\ldots\nu}(x,\alpha) = \sum_{n\in\mathbb{Z}} e^{in\alpha/R} f^{(n)}_{\mu\ldots\nu}(x). \tag{2.8}$$

The infinite set of R^4-dependent Fourier modes are said to comprise a so-called Kaluza-Klein (KK) tower of states. Much like a quantum mechanical particle on a ring, the α-component of momentum is discretized in multiples of R^{-1}. Effectively 4D physics can be recovered if R is small enough, because then even the $n = 1$ KK tower states will have α-momenta too large to be produced at the LHC.

To make all of this more explicit, it is convenient to consider the simplest case of a complex scalar field ϕ of mass m_0. The full 5-dimensional action is

$$S_5 = \int_0^{2\pi R} d\alpha \int d^4x (\partial_M \phi^*(x,\alpha)\partial^M \phi(x,\alpha) - m_0^2 |\phi(x,\alpha)|^2). \tag{2.9}$$

Expanding ϕ in a Fourier series then gives

$$
\begin{aligned}
S_5 = \frac{1}{2\pi R}\int_0^{2\pi R} d\alpha\, e^{i(n-m)\alpha/R} \int d^4x \Bigg(\sum_{m,n} \partial_\mu \phi^{(m)*}(x)\partial^\mu \phi^{(n)}(x) + \\
\sum_{m,n} \frac{im}{R}\frac{in}{R}\phi^{(m)*}(x)\phi^{(n)}(x) - m_0^2 \sum_{m,n} \phi^{(m)*}(x)\phi^{(n)}(x) \Bigg) \qquad (2.10) \\
= \sum_n \int d^4x \left(\partial_\mu \phi^{(n)*}(x)\partial^\mu \phi^{(n)}(x) - \left[m_0^2 + \frac{n^2}{R^2} \right] |\phi^{(n)}(x)|^2 \right)
\end{aligned}
$$

Thus, the effective 4D action for a single 5D scalar field corresponds to a KK tower of increasingly heavy 4D scalars with masses $m_0 \oplus n/R$. Notice that each tower state is labeled by a number $n \in \mathbb{N}$. Larger n corresponds to larger 5th dimension momentum; this is manifested as a larger mass in 4 dimensions.

KK theory is obviously no longer viewed as a viable theory of the universe. For instance, it has nothing to say about the strong and weak interactions. It also turns out that the extra dimensions of KK theory have a very large ($\gg$ TeV) compactification scale. However, the idea of using XD as a means of answering difficult questions in physics has persisted.

Widespread interest in TeV scale extra dimensions began in 1998 with the work of Arkani-Hamed *et al.* [41]. These authors hypothesized the existence of so-called large extra dimensions, and such models are now eponymously referred to as ADD. ADD addresses the constraint of apparently-4D physics by confining SM fields to a 3-brane, and addresses the hierarchy problem by allowing gravity to spread through $n \geq 1$ extra dimensions.

Several new physics scenarios incorporate so-called warped extra dimensions. Such theories are often referred to as Randall-Sundrum (RS) models after their originators [42]. In the most basic type of RS model, the topology of spacetime is that of two 3-branes separated by a single extra dimension. The metric changes rapidly along the extra dimension (spacetime is “warped”) which suppresses the graviton wave function on the SM brane.

2.2.2 Features of MUED

Several XD scenarios were briefly introduced in the previous section. The present section serves as a more in-depth presentation of the scenario with which this dissertation is concerned: universal extra dimensions. A brief overview will be presented first. It will then be possible to show some sample MUED KK towers, characterize the mass spectrum, and illustrate explicitly the cascade processes which contribute to the three lepton final state of interest.

Overview

Models with extra dimensions in which all SM fields are free to propagate are said to possess universal extra dimensions. The idea was first proposed by Dobrescu *et al.* in 2001 [43]. It is a radical idea, because it implies that all SM fields are associated with KK towers (unlike, say, in ADD style models where the SM is brane-localized). UED therefore has an intricate mass spectrum. Each SM particle has access to states of increasingly large effective mass labeled by natural numbers n. It will be shown below that only the $n = 1$ tower states are practical for LHC discovery. Apparently-4D physics is then recovered by compactifying the dimensions at a sufficiently small length scale $R \sim \text{TeV}^{-1} \sim 10^{-19}$ m. Notice that this picture of "SM+partner fields" is reminiscent of supersymmetric models. Phenomenologically, the two models turn out to be quite similar; this will be a recurring theme in this chapter.

The simplest and most extensively studied UED scenario is called minimal UED. It is characterized by three parameters: R, a cutoff scale $\Lambda > R^{-1}$, and the Higgs mass (which will always be set to $m_h = 125$ GeV here). An explicit cutoff Λ is needed because the theory, like many extra dimensions scenarios, is non-renormalizable [44]. This implies that UED should be understood as an effective low energy theory which is embedded in a complete higher energy theory. A single extra dimension which is compactified on a $S^1/\mathbb{Z}_2$ orbifold is the defining characteristic of MUED. As shown in figure 2.2, this modular structure can be roughly conceptualized as a circle with diametrical identifications so that it becomes a line segment with well-defined endpoints. The fundamental domain of this structure can then be taken to be $[0, \pi R]$ [45]. With this topology in place, a set of Feynman rules has been derived and used to compute leading order (LO) cross sections for various collider-relevant processes [46] [47]. At the time of this writing, next-to-LO (NLO) cross sections have not been computed for MUED.

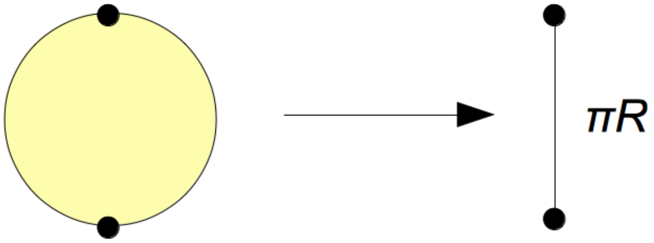

Figure 2.2: Schematic illustrating the topology of the $S^1/\mathbb{Z}_2$ orbifold.

Naively, it could be argued that momentum should be conserved in universal XDs because all fields propagate in them. Recalling the discussion of KK theory in section 2.2.1, conservation of momentum in the extra dimension implies that the KK (mode) number n is an exactly conserved quantity at tree level in 4D. This means that the aforementioned Feynman rules do not include vertices involving a single KK tower state. The tree level masses of these states are therefore almost degenerate (dominated by R^{-1}) and given by:

$$m_n = m_0 \oplus \frac{n}{R}, \tag{2.11}$$

where m_0 is the mass of the SM field in question.

However, complications arise when quantum corrections are considered. To see this, note that translational symmetry is manifestly broken by the existence of the fixed points $\alpha = 0,\ \pi R$ of $S^1/\mathbb{Z}_2$. More precisely, boundary-localized terms known as brane kinetic terms (BKTs) must be introduced into the Lagrangian in order to allow renormalization of the fields in the bulk [45]. These terms have a simple form; for example [48]:

$$\mathcal{L}_{UED} \supset \frac{\delta(\alpha) + \delta(\alpha - \pi R)}{\Lambda} \left(G_3 (F_{\mu\nu})^2 + i F_3 \bar{\psi} \not{D} \psi + i F_4 \bar{\psi} \Gamma^4 \partial_4 \psi \right), \quad (2.12)$$

where the couplings G_3 and $F_{3,4}$ are arbitrary field–specific parameters of the theory. Since these new couplings are localized to the boundaries, their associated corrections are volume-suppressed. It turns out that their effects are roughly the same size as corrections due to loops, and both effects end up breaking the mass degeneracy of equation 2.11. More details are given below.

This explicit violation of translational invariance means that n is not a conserved quantity in MUED. In the next subsection it will be shown that use of orbifolds in UED models is necessary to replicate the SM's 4D chirality. For now it is enough to note that this orbifolding, along with the assumption—built into equation 2.12—that the BKTs are invariant under a swap of the fixed points (an additional $\mathbb{Z}_2$ symmetry), implies that the so-called KK-parity $P_{KK} \equiv (-1)^n$ is conserved. This fact is of particular importance for collider searches. It immediately implies that $n = 1$ states cannot be singly produced, and also that the lightest $n = 1$ KK particle (LKP) is stable. The analogy to R-parity conserving (RPC) SUSY is again seen to arise naturally.

In MUED, the LKP is usually the excited photon γ_1 [49]. The γ_1 mass is large ($\sim R^{-1}$), and the cross section for EM interaction with the detector is therefore small. Since this field is also stable, it can generate large $\not{E}_T$ in the final state. It will be seen below that large mass splittings between various $n = 1$ states create the necessary phase space for production of high transverse momentum (p_T) leptons.

Before presenting further details, it is worthwhile to pause and make a few motivating comments. Since the LKP is stable, heavy, and neutral, it is a WIMP DM candidate [50]. This property, coupled with the theory's simplicity and predictive power, is the most important motivating factor for the MUED search presented in this thesis. UED's other important features include an explanation of the number of fermion generations [51], insights into neutrino oscillations [52], and a natural way to understand the existence of the scalar Higgs doublet [53].

Because the LKP is a DM candidate, its relic abundance can be computed and compared with cosmological observations. This computation has been performed for $\Lambda R = 20$ and 50, and the results were compared with WMAP data [12]. An illustrative plot from this work is reproduced in figure 2.3. The contours in this figure are drawn through the WMAP 7 year average physical dark matter density parameter $\Omega_c h^2 = 0.1120 \pm 0.0056$, where $h \sim 0.719$ is the reduced Hubble constant. These results suggest that $R^{-1} \sim 1.4$ TeV is the preferred scale when $n \leq 2$ KK tower states are included. The goal for collider searches is therefore—barring discovery—to push the lower bound on R^{-1} past 1.4 TeV. Note that the scale 1.4 TeV is obtained assuming that DM is entirely γ_1 and should therefore be treated as an upper bound.

Several other flavors of UED have been studied extensively in the literature [54]. Of particular experimental interest is a scenario wherein the SM and a single UED are embedded in a higher dimensional space where the bulk is only accessible to gravitons G. A KK-parity violating LKP decay is allowed $\gamma_1 \to \gamma + G$, and the corresponding signature is 2 photons and $\not{E}_T$. Stringent limits have been set on this scenario by ATLAS [55].

Mass Spectrum

Now that a general overview of MUED has been given, the next project is to write down the explicit KK towers and understand their quantum corrections. In particular, it is important to understand the mass spectrum of the theory and its implications for collider phenomenology.

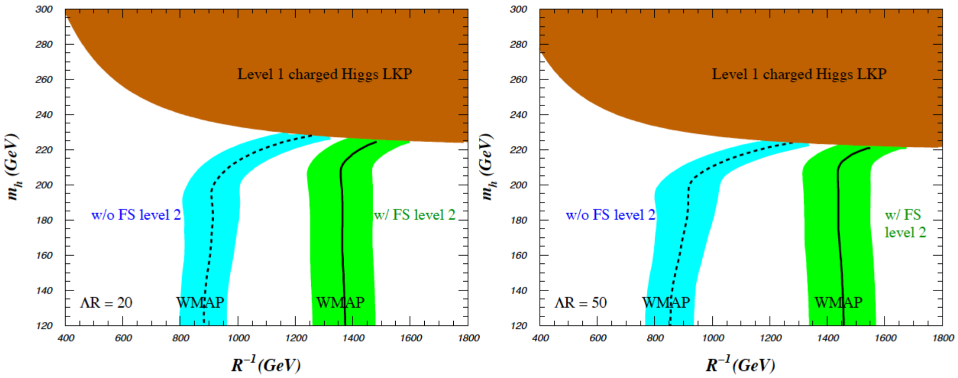

Figure 2.3: The MUED γ_1 relic abundance is computed and compared with 7 year average WMAP results for two values of ΛR. The preferred scale is $R^{-1} \lesssim$1.4 TeV. "FS level 2" refers to the inclusion of $n = 2$ KK tower states in the calculations.

It is helpful to begin by writing down the effective 4D MUED Lagrangian. As usual, this is obtained by integrating the full Lagrangian $\mathcal{L}_{MUED}$ over the extra dimension. The form of the Lagrangian is a straightforward generalization of equation 2.1:

$$\mathcal{L}^{eff}_{MUED} = \int_0^{\pi R} d\alpha \left[-\frac{1}{4} F_{i\mu\nu}(x,\alpha) F_i^{\mu\nu}(x,\alpha) + i\bar{\psi}(x,\alpha)\Gamma^M D_M \psi(x,\alpha) \right. \\ \left. + \psi_i(x,\alpha) y_{ij} \psi_j(x,\alpha)\phi(x,\alpha) + h.c. + |D_M \phi(x,\alpha)|^2 - V(\phi) \right], \tag{2.13}$$

where $M \in \{0, 1, 2, 3, 4\}$, and Γ_M are a set of Dirac matrices satisfying the 5-dimensional Clifford algebra $\{\Gamma_M, \Gamma_N\} = 2\eta_{MN}$ [43].

Recall that the KK tower emerges explicitly when the α integral in equation 2.13 is performed by exploiting the periodicity of the XD to perform Fourier expansions of the fields along the orbifold. The next task is then to write out these expansions in such a way that it is possible to recover the SM with the various zero modes. In particular, it must be decided whether each field is even or odd under the $\alpha \to -\alpha$ $\mathbb{Z}_2$ symmetry of the orbifold (*i.e.* boundary conditions must be chosen to describe 5D parity). Following Cheng *et al.* [56], note that odd fields are subject to Dirichlet boundary conditions $\Phi|_{\alpha=0,\pi R} = 0$ and even fields are subject to Neumann boundary conditions $\partial_4\Phi|_{\alpha=0,\pi R} = 0$. For general even (+) or odd (−) fields $\Phi_\pm(x,\alpha)$, the Fourier expansions are then

$$\begin{aligned}
\Phi_+(x,\alpha) &= \frac{1}{\sqrt{\pi R}}\phi_+^{(0)}(x) + \sqrt{\frac{2}{\pi R}}\sum_{n=1}^{\infty}\cos\left(\frac{n\alpha}{R}\right)\phi_+^{(n)}(x), \qquad (2.14)\\
\Phi_-(x,\alpha) &= \sqrt{\frac{2}{\pi R}}\sum_{n=1}^{\infty}\sin\left(\frac{n\alpha}{R}\right)\phi_-^{(n)}(x).
\end{aligned}$$

It is seen that zero modes of odd fields are projected out; this fact allows recovery of SM fermion chirality. Solutions of the 5D Dirac equation on $\mathbb{R}^{1,3} \times (S^1/\mathbb{Z}_2)$ can be written as Dirac spinors $\psi = (\psi_L, \psi_R)$. Only one of ψ_L or ψ_R can consistently be assigned a zero mode [9], which gives the desired chiral 4D fermion structure. The zero mode of the vector's 5th component A^4 must also be odd (projected out) to remove the possibility of a massless adjoint scalar which is not part of the SM [56] [46]. The $0, ..., 3$ vector components A^μ are even.

In summary, each field must be KK decomposed in such a way that the zero modes are the SM, and the topology of the orbifold makes it possible to do this in a self-consistent way via boundary conditions. As an explicit example of equation 2.14, the MUED quark fields Q ($SU(2)$ doublets), U, and D ($SU(2)$ singlets) can be written as

$$\begin{aligned}
Q(x,\alpha) &= \frac{1}{\sqrt{\pi R}}\left[\begin{pmatrix} u(x) \\ d(x) \end{pmatrix}_L + \sqrt{2}\sum_{n=1}^{\infty}\left(Q_L^n(x)\cos\frac{n\alpha}{R} + Q_R^n(x)\sin\frac{n\alpha}{R}\right)\right], \\
U(x,\alpha) &= \frac{1}{\sqrt{\pi R}}\left[u_R(x) + \sqrt{2}\sum_{n=1}^{\infty}\left(U_R^n(x)\cos\frac{n\alpha}{R} + U_L^n(x)\sin\frac{n\alpha}{R}\right)\right], \\
D(x,\alpha) &= \frac{1}{\sqrt{\pi R}}\left[d_R(x) + \sqrt{2}\sum_{n=1}^{\infty}\left(D_R^n(x)\cos\frac{n\alpha}{R} + D_L^n(x)\sin\frac{n\alpha}{R}\right)\right],
\end{aligned} \tag{2.15}$$

where u and d are the corresponding zero mode SM quarks. Notice that the right(left)-handed zero mode of Q (U, D) has been projected out, but higher tower states contain both L and R.

When all of the SM expansions analogous to equation 2.15 are used to perform the integral in equation 2.13, KK towers with masses given by equation 2.11 emerge. An example of this procedure was shown in equation 2.10. As was discussed above, though, the masses receive important quantum corrections beyond tree level. The form of these corrections has been computed by Cheng *et al.* [56] and will now be discussed.

One loop bulk δ_{Bu} and boundary δ_{Bo} mass corrections for a general field ϕ at KK tower level $n > 0$ take the form

$$\begin{aligned}
\delta_{Bu}(m_{\phi_n}^2) &= \frac{\Delta(\phi)}{16\pi^4 R^2}, \\
\delta_{Bo}(m_{\phi_n}^2) &= m_n \xi(\phi) \ln\left(\frac{\Lambda}{\mu}\right),
\end{aligned} \tag{2.16}$$

where Δ and ξ are field-specific constants, and μ is the renormalization scale (set to R^{-1} for this analysis). δ_{Bo} are assumed to vanish past the cutoff scale Λ. Cheng *et al.* [48] have created a convenient visualization of the size of the radiative corrections as a function of the cutoff. This is displayed in figure 2.4. Note from the form of δ_{Bo} that, for a given R, the mass splittings grow logarithmically with ΛR. It therefore is convenient to use the dimensionless product ΛR as a MUED parameter instead of Λ. The aforementioned authors have created another useful figure which illustrates the degeneracy breaking effect of the one loop corrections. It is reproduced here in figure 2.5.

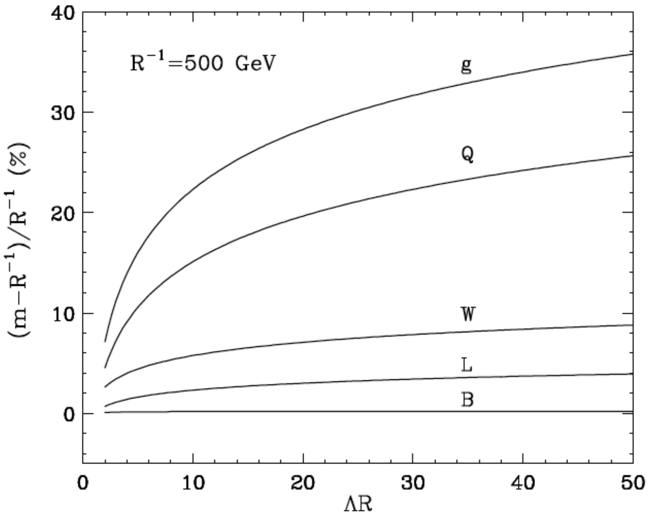

Figure 2.4: The relative size of MUED radiative mass corrections as a function of ΛR ($R = 1/500$ GeV^{-1}) for various $n = 1$ modes.

The next natural question concerns the collider implications of the larger phase space now accessible in light of the widened MUED mass spectrum. Of particular importance to this thesis is the question of how a $3\ell + \not{E}_T$ final state may be obtained from pp collisions. Approximate LO parton[1]–level cross sections for all MUED strong production modes at $\sqrt{s} = 7$ TeV have been computed using the PYTHIA [58] Monte Carlo (MC) event generator. The results are shown in table 2.1. This table gives an idea of which parton level processes are important, and a Feynman diagram illustrating a cascade of the most important such processes to $3\ell + \not{E}_T$ is shown in figure 2.6. It

---

[1] In modern high energy physics, the generic term "parton" collectively describes quarks and gluons. The term has its origins in work by Feynman [57].

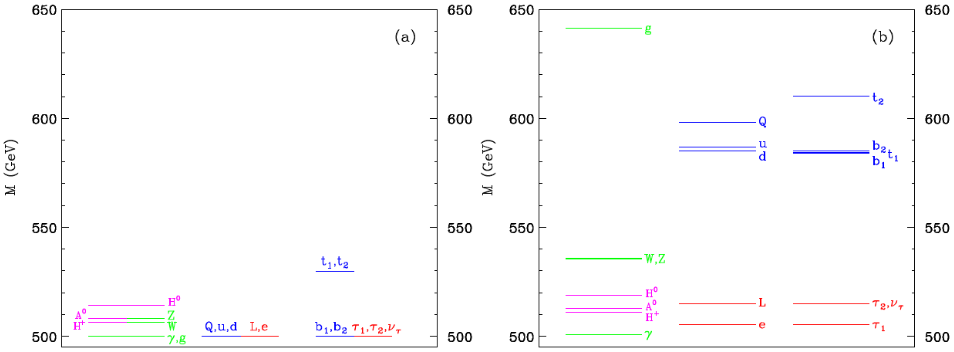

Figure 2.5: One loop corrections (right) break the approximate tree level mass degeneracy (left) of the $n = 1$ tower states. The masses shown here correspond to the point $(R^{-1}, \Lambda R, m_h) = (500\text{ GeV}, 20, 120\text{ GeV})$

is seen that the cascades of interest are those involving W_1/Z_1.

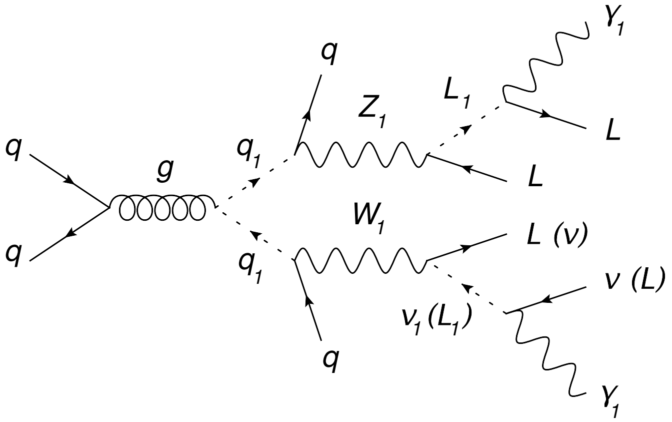

Figure 2.6: A cascade $qq \to q_1 q_1 \to 3\ell + \not{E}_T$ involving $n = 1$ MUED excitations. As shown in table 2.1, this diagram is the leading contribution to the final state of interest in this thesis.

Table 2.1: Approximate LO MUED parton level cross sections (10^6 events, $\sqrt{s} = 7$ TeV) for the point $(R^{-1}, \Lambda R) = (500\ \text{GeV}, 20)$ computed with PYTHIA. The cross sections are shown in descending order. Here Q (S) refers to doublet (singlet) quarks, $*$ denotes the $n = 1$ excitation, and i, j are quark flavors.

Subprocess	Approximate σ (mb)
$q_i + q_j \to Q_i^* + Q_j^*$	5.5×10^{-11}
$q_i + q_j \to Q_i^* + S_j^*$	3.8×10^{-11}
$q + g \to Q^* + g^*$	2.9×10^{-11}
$q + \bar{q} \to Q^* + \overline{Q}^*$	3.9×10^{-12}
$q_i + \bar{q}_i \to Q_j^* + \overline{Q}_j^*$	2.8×10^{-12}
$q_i + \bar{q}_j \to Q_i^* + \overline{Q}_j^*$	2.4×10^{-12}
$q_i + \bar{q}_j \to Q_i^* + \overline{S}_j^*$	2.0×10^{-12}
$g + g \to g^* + g^*$	5.7×10^{-13}
$g + g \to Q^* + \overline{Q}^*$	8.3×10^{-14}
Total	1.3×10^{-10}

2.3 Supersymmetry

Since its theoretical origins in the early 1970s [59] [60] [61], supersymmetry has remained at the forefront of research in both theoretical and experimental subatomic physics. Confirming or excluding its predictions is one of the main components of the LHC physics program [62].

SUSY predicts that, corresponding to each SM field, a so-called superpartner field exists whose spin differs by a half unit. Table 2.2, adapted from Bertone *et al.* [63], gives a general sense of this construction. The nomenclature in this table is standard. Matter field superpartners are prepended with an "s," while the superpartners of the gauge bosons receive an "ino" suffix. It turns out that this idea can be used as a tool to solve several of the open SM problems discussed above. This section serves as a basic review of the cardinal elements of SUSY. For simplicity, the essential character of the SUSY formalism will be discussed mostly in the context of the minimal supersymmetric SM (MSSM). The discussion will then be specialized to the "simplified models" considered in this analysis. A much more comprehensive introduction can be found in, *e.g.*, Martin's classic primer [64].

2.3.1 Features of the MSSM

Although the key ideas of SUSY were written down in the early 1970s, it wasn't until 1981 that these ideas began to coalesce into a model still widely used today [65] [66] [67]. This important model, now understood to be the simplest supersymmetric SM extension, came to be known in ensuing years as the MSSM; the present section will examine its key tenets. The discussion will draw from [64].

Lagrangian

A supersymmetry is a symmetry relating fermions F and bosons B. Schematically, this can be written

$$Q\left|F\right\rangle \sim \left|B\right\rangle, \quad Q\left|F\right\rangle \sim \left|B\right\rangle. \tag{2.17}$$

SM fields			SUSY partners				
			Interaction		Mass		
Symbol	Name	Spin	Symbol	Name	Symbol	Name	Spin
q	Quark	$\frac{1}{2}$	$\widetilde{q}$	Squark	$\widetilde{q}$	Squark	0
ℓ	Lepton	$\frac{1}{2}$	$\widetilde{\ell}$	Slepton	$\widetilde{\ell}$	Slepton	0
ν	Neutrino	$\frac{1}{2}$	$\widetilde{\nu}$	Sneutrino	$\widetilde{\nu}$	Sneutrino	0
g	Gluon	1	$\widetilde{g}$	Gluino	$\widetilde{g}$	Gluino	$\frac{1}{2}$
$W^{\pm}$	W boson	1	$\widetilde{W}^{\pm}$	Wino	$\widetilde{\chi}_i^{\pm}$	Chargino	$\frac{1}{2}$
H_d^-	Higgs boson	0	$\widetilde{H}_d^-$	Higgsino			
H_u^+	Higgs boson	0	$\widetilde{H}_u^+$	Higgsino			
B	B boson	1	$\widetilde{B}$	Bino	$\widetilde{\chi}_j^0$	Neutralino	$\frac{1}{2}$
W^0	W^0 boson	1	$\widetilde{W}^0$	Wino			
H_u^0	Higgs boson	0	$\widetilde{H}_u^0$	Higgsino			
H_d^0	Higgs boson	0	$\widetilde{H}_d^0$	Higgsino			

Table 2.2: The particle spectrum of SUSY. All SM fields and their corresponding superpartners are tabulated. Note that $i = 1, 2$ and $j = 1, ..., 4$. Both interaction and mass eigenstates are shown for the SUSY fields.

As with any symmetry, the goal is to be able to write combinations of operators (Lagrangian terms) which are invariant under the action of Q. In general this is achieved by understanding the precise group structure associated with the symmetry, and then describing the fields as irreducible representations thereof. The first step towards a SUSY Lagrangian, then, is to write down the relevant Lie algebra.

Before this is possible, it's necessary to quickly review some details of the Weyl spinor notation. Recall [68] that the (restricted) Lorentz group is isomorphic to two copies of $SU(2)$: $SO^+(1,3) \cong SU(2) \times SU(2)$. This means that all irreducible representations of this group can be catalogued by a pair of usual $SU(2)$ quantum numbers. The left- and right-handed spinors are the $(\frac{1}{2},0)$ and $(0,\frac{1}{2})$ representations, respectively. There is then some freedom of choice allowed when including spinors in a quantum field theory. So-called Dirac spinors ψ_D correspond to the reducible representation $(\frac{1}{2},0)\oplus(0,\frac{1}{2})$. These arise naturally when considering plane wave solutions to the Dirac equation and are therefore most familiar. Since the SM is a chiral theory, it is often more convenient to treat the two irreducible spinor representations on separate footing. This is the idea behind the Weyl formulation. The relationship between the two-component Weyl and more familiar four-component Dirac spinors is as follows:

$$\psi_D = \begin{pmatrix} \xi \\ \overline{\chi} \end{pmatrix}, \tag{2.18}$$

where the two components of each ξ (left-handed, L) and $\overline{\chi}$ (right-handed, R) are complex Grassmann numbers. Note that the "bar" is part of the name of the R spinor; no mathematical operation is implied.

Because ξ and $\overline{\chi}$ transform differently under action of the Lorentz group, it is conventional to index them with different symbols. In particular, left(right)-handed spinors receive "undotted" ("dotted") indices[2]. By abusing notation in an illustrative way, equation 2.18 can then be rewritten as follows:

$$\psi_D = \begin{pmatrix} \xi_\alpha \\ \overline{\chi}^{\dot{\alpha}} \end{pmatrix}, \tag{2.19}$$

and the fact that L and R are complex conjugate representations may be expressed as

$$\chi^\dagger_\alpha \equiv \overline{\chi}_{\dot{\alpha}}. \tag{2.20}$$

These conventions and definitions have been put in place to make it simple to write down Lorentz invariant spinor products. With this notation, for example, the general form of the free Lagrangian for a theory containing n

---

[2] The indices can be raised and lowered by an antisymmetric quantity $\epsilon^{\alpha\beta} = \epsilon^{\dot{\alpha}\dot{\beta}}$.

fermions χ_i is

$$\begin{aligned}\mathcal{L}_f &= i\sum_i^n \overline{\chi}_i^{\dot{\alpha}}(\overline{\sigma}^\mu)_{\dot{\alpha}\alpha}\partial_\mu\chi_i^\alpha - \frac{1}{2}\sum_{i,j}^{n,n}\left(m_{ij}\chi_{i\alpha}\chi_j^\alpha + m_{ij}\overline{\chi}_i^{\dot{\alpha}}\overline{\chi}_{j\dot{\alpha}}\right) \\ &\equiv i\sum_i^n \overline{\chi}_i\overline{\sigma}^\mu\partial_\mu\chi_i - \frac{1}{2}\sum_{i,j}^{n,n}\left(m_{ij}\chi_i\chi_j + m_{ij}^*\overline{\chi}_i\overline{\chi}_j\right) \qquad (2.21)\end{aligned}$$

where $\overline{\sigma}^\mu \equiv (I, -\vec{\sigma})$, and m_{ij} is the symmetric mass matrix.

It is easiest to derive the SUSY algebra in the context of a simple toy supersymmetric model called the Wess-Zumino model [61]. This model features a Weyl fermion ψ and a complex scalar ϕ; these fields are massless and do not interact. The Lagrangian is

$$\mathcal{L}_{WZ} = i\overline{\psi}\overline{\sigma}^\mu\partial_\mu\psi - \partial_\mu\phi\partial^\mu\phi^* \qquad (2.22)$$

Now parametrize a supersymmetry between these fields with an infinitesimal two-component Weyl fermion ϵ_α:

$$\delta_\epsilon\phi = \epsilon_\alpha\psi^\alpha, \quad \delta_\epsilon\psi_\alpha = -i(\sigma^\mu\overline{\epsilon})_\alpha\partial_\mu\phi \qquad (2.23)$$

It can be shown that the action is invariant $\delta S_{WZ} = 0$ under this transformation. It's also relatively straightforward to show that the commutator $[\delta_{\epsilon_1}, \delta_{\epsilon_2}]$ closes; *i.e.* gives another SUSY transformation. This latter proof requires that a non-interacting auxiliary field F be introduced to ensure closure off-shell. Both of these facts together imply that equation 2.23, along with an associated transformation for F, is indeed a symmetry of $\mathcal{L}_{WZ} + F^*F$. Noether's theorem can therefore be used to compute the fermionic generators of the algebra Q_α and $\overline{Q}_{\dot{\alpha}}$, where the notation is deliberately reminiscent of equation 2.17. These supersymmetric Noether charges are known as supercharges.

The precise form of the supercharges is not important here. The important fact is that their explicit forms can be used to verify the following supersymmetry algebra:

$$\{Q_\alpha, \bar{Q}_{\dot{\alpha}}\} = -2\sigma^\mu_{\alpha\dot{\alpha}} P_\mu, \;\; \{Q_\alpha, Q_\beta\} = 0, \;\; \{\bar{Q}_{\dot{\alpha}}, \bar{Q}_{\dot{\beta}}\} = 0, \tag{2.24}$$

where P^μ is the generator of spacetime translations, namely the usual total energy-momentum operator. The full algebra for a supersymmetric field theory, sometimes called the super-Poincaré algebra [69], is then obtained by writing down, in addition to equation 2.24, the usual Lie brackets for the Poincaré group generators and their corresponding brackets with the SUSY generators.

With this algebra[3] in place, SUSY is characterized. It is now possible to write down irreducible representations and use them to construct a supersymmetric extension of the SM. Intuitively, these representations are formed by grouping the bosonic and fermionic degrees of freedom related by SUSY (superpartners) into sets called supermultiplets [71]. In the Wess-Zumino model there is a single supermultiplet $\{\psi, \phi\}$ called a chiral supermultiplet. Similarly, supermultiplets containing a vector are called vector supermultiplets. The chiral and vector supermultiplets of the MSSM were summarized above in table 2.2.

The most natural language for writing SUSY Lagrangians involves so-called superfields [71]. A superfield is a field defined on spacetime and four additional Grassmannian coordinates $\Phi(x^\mu, \theta_\alpha, \overline{\theta}_{\dot{\alpha}})$. These fields are constructed in such a way that their Taylor expansions contain the field content of a given supermultiplet. Heuristically, for example, $\Phi \supset (\phi, \psi, F)$. Lagrangians written in terms of the familiar supermultiplet fields are then recovered by integrating the fermionic coordinates out of particular functions of the superfields called superpotentials. This formalism makes it easy to write manifestly supersymmetric operator combinations.

---

[3] Because it has both anti-commuting (fermionic) and commuting (bosonic) generators, the super-Poincaré algebra is technically not a Lie algebra. It is in fact a more general structure called a Lie superalgebra [70].

It is now possible to understand the form of the MSSM Lagrangian $\mathcal{L}_{MSSM}$ by cataloguing the terms produced by integrating its various superpotentials. A thorough discussion of the MSSM Lagrangian is beyond the scope of this thesis; a comprehensive term-by-term treatise has been prepared by Kuroda [72], for example. The Lagrangian takes the following form [73]:

$$\mathcal{L}_{MSSM} = \int d^2\theta d^2\overline{\theta}\,[K(\Phi_i) + W(\Phi_C) + G(\Phi_V)] + \mathcal{L}_B. \tag{2.25}$$

A discussion of each term in equation 2.25 follows.

- The first term involves a so-called Kähler potential K, which here is a function of all chiral and vector superfields in the MSSM Φ_i. When fully expanded, this term contains kinetic terms for the (s)fermions and Higgs(inos) as well as the interactions of these fields with the gauge bosons and gauginos.

- The quantity W appearing in the second term is known as *the* MSSM superpotential and is a function of all chiral superfields $\Phi_C = \{H_u, H_d, Q, L, \overline{u}, \overline{d}, \overline{e}\}$:

  $$W = \overline{u}\boldsymbol{y_u}QH_u - \overline{d}\boldsymbol{y_d}QH_d - \overline{e}\boldsymbol{y_e}LH_d + \mu H_u H_d, \tag{2.26}$$

  where $\boldsymbol{y_{u,d,e}}$ are 3×3 matrices of Yukawa couplings (*i.e.* they act on suppressed generational indices), and μ is called the Higgsino mass parameter. W may therefore be understood as a supersymmetric generalization of the analogous Yukawa interactions in equation 2.1. It is important to point out that two $SU(2)$ Higgs doublets H_u and H_d are needed in the MSSM as opposed to the single such doublet in the SM. This additional structure is necessary to avoid an anomaly in the EW sector. When the integral in equation 2.25 is performed, W contributes Yukawa terms for fermions and sfermions, as well as Higgsino mass terms.

- The third term contains a function of the vector superfields called the gauge superpotential $G(\Phi_V)$. Upon integration it contributes kinetic terms for the gauge bosons and gauginos as well as the relevant self-interactions.

- The last term $\mathcal{L}_B$ describes soft SUSY breaking. $\mathcal{L}_{MSSM}$ as written above is pre-SSB. Without $\mathcal{L}_B$, each field would receive the same mass as its corresponding superpartner when H_u and H_d acquire VEVs. In light of, say, the various experimental sparticle mass limits mentioned in chapter 1, this situation is evidently not realized in nature. SUSY must therefore be a broken symmetry. If SUSY is to be realistic, then, it can only be an exact symmetry of the underlying high energy Lagrangian, and its low energy (hence "soft") effective manifestation appears spontaneously broken. A multitude of breaking mechanisms have been proposed [74]. Experiments can currently only probe as high as the TeV scale, though, so it is more immediately useful to insert explicit phenomenological SUSY breaking terms via $\mathcal{L}_B$. The consequence of this non-fundamental approach is a preponderance of free parameters. Indeed, the highly economical form of equation 2.25 obscures 105 such parameters [75]. This fact presents a major challenge to the experimentalist. When designing an analysis it is important to avoid as much of this model-dependence as is possible. Further comments on this topic will be made in the next section. Explicitly, $\mathcal{L}_B$ contains additional sfermion-Higgsino couplings, and mass terms for the gauginos, sfermions, and higgsinos which all violate SUSY.

Charginos and Neutralinos

Feynman rules can be perturbatively derived from $\mathcal{L}_{MSSM}$, and the experimentalist can then compare the predictions of SUSY to observations. Before moving on to the experimental details of the present analysis, though, it is necessary to further understand the nature of charginos and neutralinos.

As discussed above, the MSSM requires two Higgs doublets $H_u \equiv (H_u^+, H_u^0)$ and $H_d \equiv (H_d^0, H_d^-)$. Each of these four fields forms a chiral supermultiplet with its fermionic Higgsino superpartner $\widetilde{H}_{u,d}^{\pm,0}$. As was shown in table 2.2, the electroweak (unbroken $SU(2)_L \times U(1)_Y$) gauge bosons, $W^{\pm,0}$ and B^0, each fall into vector supermultiplets with their respective superpartners $\widetilde{W}^{\pm,0}$ and $\widetilde{B}^0$. Electroweak symmetry breaking in the MSSM, *i.e.* assigning VEVs to both Higgs doublets, causes mixing between the Higgsino and gaugino states. In particular, mixing between the charged Higgsinos and charged winos yields four mass eigenstates called charginos $\widetilde{\chi}_i^{\pm}$. Similarly, mixing between the neutral Higgsinos, neutral wino, and bino yields four mass eigenstates called neutralinos $\widetilde{\chi}_j^0$. Both sets of states are labeled in terms of increasing mass.

Define a neutralino mass term by collecting together post-EWSB Lagrangian terms which are quadratic in neutral gaugino and Higgsino states as follows:

$$\mathcal{L}_{MSSM} \supset -\frac{1}{2}(\widetilde{\psi}^0)^T M_{\widetilde{N}} \widetilde{\psi}^0 + h.c., \tag{2.27}$$

where $\widetilde{\psi}^0 = (\widetilde{B}, \widetilde{W}^0, \widetilde{H}_d^0, \widetilde{H}_u^0)$ and the mass matrix is given by

$$M_{\widetilde{N}} = \begin{pmatrix} M_1 & 0 & -m_Z c(\beta) s(\theta_W) & m_Z s(\beta) s(\theta_W) \\ 0 & M_2 & m_Z c(\beta) c(\theta_W) & -m_Z s(\beta) c(\theta_W) \\ -m_Z c(\beta) s(\theta_W) & m_Z c(\beta) c(\theta_W) & 0 & -\mu \\ m_Z s(\beta) s(\theta_W) & -m_Z s(\beta) c(\theta_W) & -\mu & 0 \end{pmatrix}, \tag{2.28}$$

where M_1 is the bino mass, M_2 is the wino mass, the abbreviation s (c) has been used for sine (cosine), θ_W is the weak mixing angle, μ is the Higgsino mass parameter from equation 2.26, and $\tan\beta$ is the ratio of Higgs VEVs. This is the representation of $M_{\widetilde{N}}$ in the neutral gauge eigenstate basis specified by $\{\widetilde{B}, \widetilde{W}^0, \widetilde{H}_d^0, \widetilde{H}_u^0\}$. If $M_{\widetilde{N}}$ is diagonalized by a matrix $\Theta_{\widetilde{N}}$, the neutralino mass eigenstates are given by:

$$\widetilde{\chi}_j^0 \equiv (\Theta_{\widetilde{N}})_{jk} \widetilde{\psi}_k^0, \tag{2.29}$$

with their masses $m_{\widetilde{\chi}_j^0}$ as the corresponding eigenvalues.

Charginos are characterized in a similar way. A chargino mass term has an associated charged gauge basis $\{\widetilde{W}^+, \widetilde{H}_u^+, \widetilde{W}^-, \widetilde{H}_d^-\}$ mass matrix:

$$M_{\widetilde{C}} = \begin{pmatrix} 0 & 0 & M_2 & \sqrt{2}m_W c(\beta) \\ 0 & 0 & \sqrt{2}m_W s(\beta) & \mu \\ M_2 & \sqrt{2}m_W s(\beta) & 0 & 0 \\ \sqrt{2}m_W c(\beta) & \mu & 0 & 0 \end{pmatrix}, \quad (2.30)$$

which can be diagonalized to give eigenstates $\widetilde{\chi}_i^\pm$ corresponding to masses $m_{\widetilde{\chi}_i^\pm}$.

For future reference, note that the two-body chargino and neutralino decays which are generally considered to be most kinematically plausible [64] are

$$\begin{aligned} \widetilde{\chi}_i^\pm &\longrightarrow \{\widetilde{\chi}_j^0 W^\pm,\ \widetilde{\chi}_1^\pm Z,\ \widetilde{\nu}\ell^\pm,\ \widetilde{\ell}^\pm\nu,\ \widetilde{\chi}_1^\pm H\}, \\ \widetilde{\chi}_j^0 &\longrightarrow \{\widetilde{\chi}_k^0 Z,\ \widetilde{\chi}_k^\pm W^\mp,\ \widetilde{\ell}^\pm\ell^\mp,\ \widetilde{\nu}\nu,\ \widetilde{\chi}_k^0 H\}. \end{aligned} \quad (2.31)$$

Note also that the cross sections for processes involving these vertices will then depend on the relative gauge eigenstate content of the various charginos and neutralinos; the terms "wino-like" and "bino-like" are often used to conveniently characterize the dominant mixing content of these eigenstates.

In hadron collider physics, the term "EW SUSY" refers to the direct production of charginos, neutralinos, or sleptons. This is to be contrasted with "strong SUSY" searches which are designed to observe direct production of squarks or gluinos. The SUSY search to be presented in this dissertation is optimized for events involving direct production of $\widetilde{\chi}_1^\pm\widetilde{\chi}_2^0$, and is therefore an EW SUSY search. A figure produced by the team behind the PROSPINO [76] NLO SUSY cross section calculation software is reproduced here as figure 2.7. This gives a sense of how the cross sections for strong and EW SUSY at the 8 TeV LHC compare.

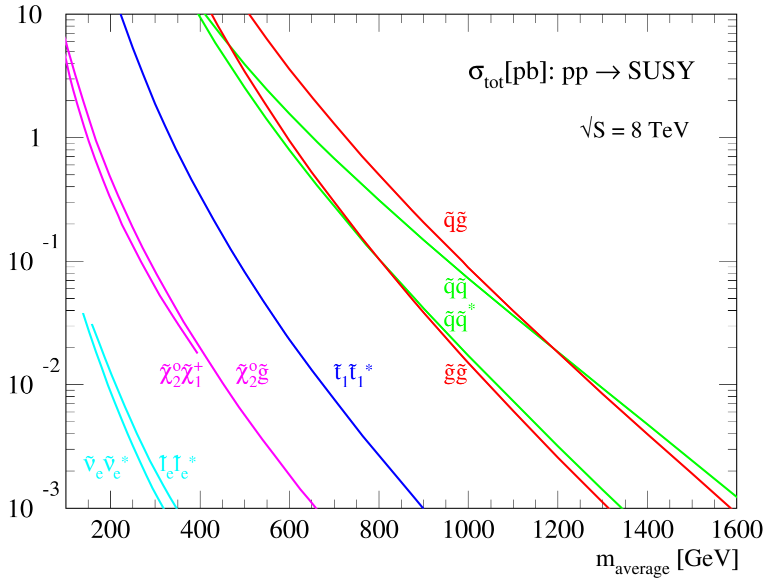

Figure 2.7: NLO cross sections for various SUSY processes at the 8 TeV LHC as computed and plotted by the PROSPINO team. The left-most pink curve shows the direct production mode considered here.

Phenomenology and Motivation

Before moving on to discuss the SUSY scenarios to be considered in this search, it is critical to explore some of the experimentally relevant consequences of supersymmetric Lagrangians such as the one in equation 2.25. This discussion will also prove to be a convenient context in which to illustrate the importance of searching for SUSY at a collider.

There are in fact other SUSY-respecting terms that could be added to the superpotential in equation 2.26. These terms have not been written because they lead to predictions which do not agree with observations. In particular, these missing terms lead to violations of baryon and lepton number conservation, *e.g.* prompt proton decay. The justification for the terms' omission is the postulate that the MSSM multiplicatively conserves so-called *R*-parity [77]. This is a quantum number which can be defined for each field as follows:

$$P_R \equiv (-1)^{3(B-L)+2s}, \tag{2.32}$$

where s is the particle's spin, B its baryon number, and L its lepton number. All SM particles (and both Higgs doublets) have $P_R = 1$ and all superpartners have $P_R = -1$, so R-parity conservation is a $\mathbb{Z}_2$ symmetry. This is useful for collider searches because it immediately implies that sparticles may only be produced in even numbers. Furthermore, if sparticles are produced, their cascade decays must terminate with the production of the lightest $P_R = -1$ SUSY particle (LSP) which is stable. Often the LSP is uncharged, and it therefore is an excellent WIMP DM candidate [78]. It is interesting to note that, although the theoretical origins of R- and KK-parities are quite disparate, their phenomenological consequences are strikingly similar. The study of SUSY scenarios which violate R-parity conservation is associated with a vast literature [79], but no more will be said about this here.

One of the most attractive features of SUSY is that certain supersymmetric scenarios predict unification of the strengths of the SM coupling constants. This is a necessary feature of a theory which can accommodate grand unification. When the MSSM renormalization group flow is studied, it predicts a unification of the inverse SM couplings at a scale $Q \sim 10^{16}$ GeV. This is illustrated in figure 2.8, which has been reproduced from Martin [64].

Perhaps the strongest motivation for SUSY is its elegant solution of the hierarchy problem [64]. The squared SM Higgs mass parameter receives divergent loop corrections from all particles to which it couples directly or indirectly. Quadratically divergent corrections arise from fermions coupling to the Higgs with strength λ_f:

$$\Delta m_H^2 \approx -\frac{|\lambda_f|^2}{8\pi^2}\Lambda_{UV}, \tag{2.33}$$

where Λ_{UV} is the regularization cutoff. If the Planck scale is the scale of new physics, then Λ_{UV} is set roughly to this scale. To achieve a light physical

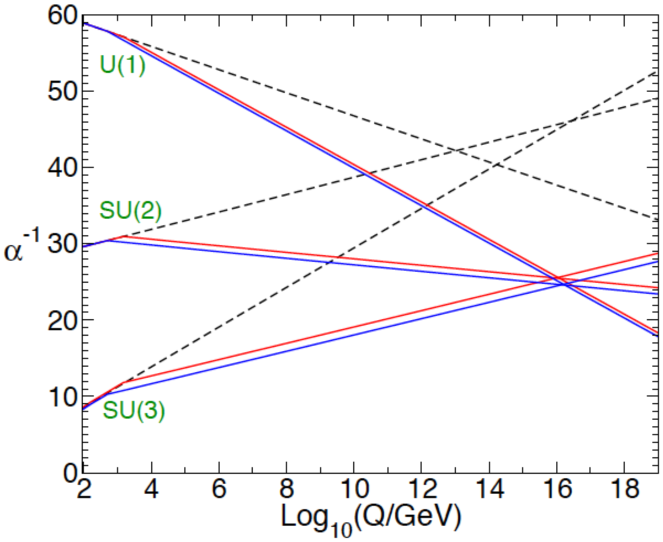

Figure 2.8: Running of SM couplings at two loop level. The dashed lines have been computed in the SM and the colored lines in the MSSM. The MSSM GUT scale is seen to be $Q \sim\ 10^{16}$ GeV. The red (blue) line has been computed under the assumption that the sparticle masses are at a common scale of 0.5 (1.5) TeV.

higgs mass $O(100)$ GeV in agreement with experiment, these large corrections must cancel precisely with the bare Higgs mass. The disparity between the EW and Planck scales therefore requires a precise, finely-tuned choice for the bare Higgs mass [80]. In SUSY, each particle's superpartner has the opposite spin. Therefore, for each quadratic divergence of the form shown in equation 2.33, there is a corresponding correction from the superpartner with the opposite sign. In this way the divergences are canceled and the hierarchy problem resolved.

Although motivation has been presented for general SUSY searches, nothing has yet been said to illustrate the importance of EW SUSY in particular. From equations 2.28 and 2.30, it's clear that charginos and neutralinos could *a priori* assume masses across a wide spectrum via judicious choices of M_1,

M_2, μ, and $\tan\beta$. However, appeals to the concept of naturalness can place restrictions on these masses. To illustrate this in the context of the MSSM, note that the following formula holds at tree level [81]:

$$-\frac{1}{2}m_Z^2 = |\mu|^2 + m_{H_u}^2. \tag{2.34}$$

It is seen that if the sparticles which contribute to the RHS become very heavy ($\gg m_Z$), a precise cancellation (fine-tuning) is required to preserve equality. This gives insight into natural SUSY. Higgsinos receive masses dictated by μ and should therefore not be extremely heavy. Similarly, $m_{H_u}^2$ is corrected to two loops principally by $\widetilde{t}$ and $\widetilde{g}$, so these too should not be exceedingly massive. Masses of other sparticles do not play a strong role in determining supersymmetric naturalness. This constitutes powerful motivation for EW SUSY searches at the TeV scale: The natural requirement of light Higgsinos implies, due to mixing, that some charginos and neutralinos should be light.

Finally, some rationale must be given for choosing to search for EW SUSY in final states with three leptons. The key observation, as will be seen quantitatively in later chapters, is that SM backgrounds in the trilepton channel tend to be quite small. For this reason it is possible to obtain comparable sensitivity to strong SUSY searches despite the much smaller signal production cross sections (recall figure 2.7).

2.3.2 Simplified Models

It was mentioned above that the large number of free parameters introduced by soft SUSY breaking is a challenge for collider searches. So-called simplified models (SIMs) [82] have been designed to facilitate practical, process-wise sets of analyses which target particular final states. These are a class of phenomenological models which aim to encapsulate the general characteristics of models with SM partner fields (*i.e.* models possessing a parity like P_R or P_{KK}) that make predictions in final states with jets, $\not{E}_T$, or leptons. Such models include SUSY and UED. This generality is achieved by avoiding assumptions about couplings, interference terms, *etc.*, and instead building a model from the ground up using only a small number of masses and branching fractions as parameters. This provides a simple framework in which to understand the general nature of a potential new signal. In this analysis two classes of SIM are utilized; a description of their properties will now be given.

In both classes of SIM to be considered, the basic SUSY production mode is associated direct production of wino-like, mass degenerate $\widetilde{\chi}_1^{\pm}$ and $\widetilde{\chi}_2^0$. As illustrated in figure 2.9, this mode is desirable because it has the largest production cross section of all direct weak gaugino modes. The LSP is a bino-like $\widetilde{\chi}_1^0$ and $\widetilde{q}$ masses are set to $O(100)$ TeV. This latter assumption kinematically decouples $\widetilde{q}$ from the cascades and ensures that no interference is present.

Of course, the final state of interest is $3\ell + \not{E}_T$. The two SIMs are differentiated by the nature of the cascades which yield these products. In one case, left-handed sleptons are light, so that they mediate the cascades ("via $\widetilde{\ell}$"). The other case features heavy sleptons, and therefore the cascades are mediated by SM W and Z bosons ("via WZ"). These choices are motivated by recalling the list of plausible decays in equation 2.31. Feynman diagrams showing the explicit decay chains of interest are found in figure 2.10, and a detailed catalog of the SIM parameters is shown in table 2.3.

As described above, the gauginos' branching ratios depend upon their mixing content. This implies that several other analyses are possible in the context of $\widetilde{\chi}_1^{\pm}\widetilde{\chi}_2^0$ SIM. For example, an analysis targeting the case where $\widetilde{\chi}_2^0 \rightarrow \widetilde{\chi}_1^0 H$ is currently in preparation by ATLAS.

2.4 The LHC Inverse Problem

As is typically the case when searching for new scientific phenomena, the function which maps new physics hypotheses to their LHC signatures is not

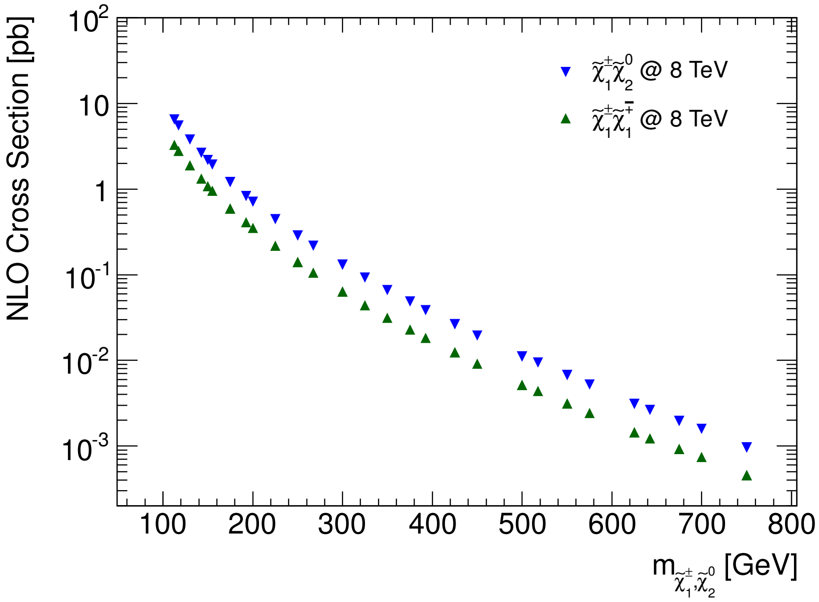

Figure 2.9: The direct production cross section for $\tilde{\chi}_1^{\pm}\tilde{\chi}_2^0$ is largest among all direct weak gaugino modes. The next largest mode $\tilde{\chi}_1^{\pm}\tilde{\chi}_1^{\mp}$ is shown here for comparison.

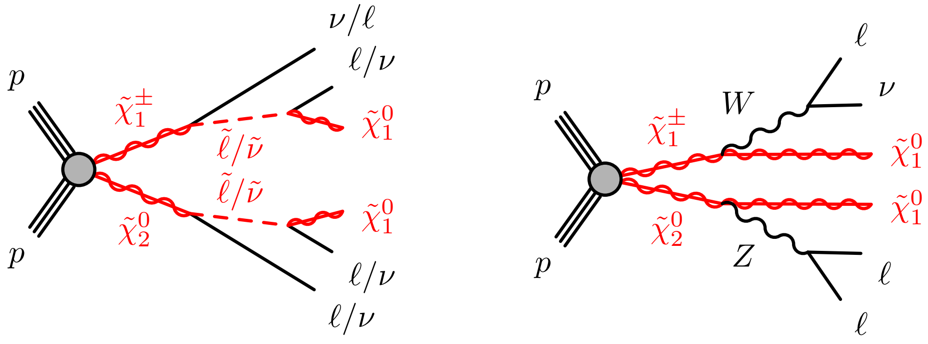

(a) (b)

Figure 2.10: Feynman diagrams showing cascades of interest in SIM via sleptons (a) and via WZ (b). Note the similarity to figure 2.6.

Table 2.3: Parameters are tabulated for both varieties of SIM considered in this analysis. All masses are listed in GeV. Parameters given as a range are varied to generate grids of signal points. Note also that mass degeneracy is assumed for all slepton flavors: $m_{\widetilde{e}} = m_{\widetilde{\mu}} = m_{\widetilde{\tau}}$. The term "heavy" here means that a particle is made sufficiently heavy so as to kinematically remove it from cascades.

Parameter	Via $\widetilde{\ell}$	Via WZ
$m_{\widetilde{\chi}_1^\pm} = m_{\widetilde{\chi}_2^0}$	100 — 700	100 — 400
$m_{\widetilde{\chi}_1^0}$	0 — $600 \wedge < m_{\widetilde{\chi}_2^0}$	0 — $300 \wedge < m_{\widetilde{\chi}_2^0}$
$m_{\widetilde{\ell}_L}$	$\frac{1}{2}\left(m_{\widetilde{\chi}_1^0} + m_{\widetilde{\chi}_2^0}\right)$	heavy
$m_{\widetilde{\ell}_R}$	heavy	heavy
$m_{\widetilde{\nu}}$	$= m_{\widetilde{\ell}_L}$	heavy
$m_{\widetilde{q}}$	heavy	heavy
$BR(\widetilde{\chi}_1^\pm \to \widetilde{\ell}_L^\pm \nu)$	0.5	0
$BR(\widetilde{\chi}_1^\pm \to \ell^\pm \widetilde{\nu})$	0.5	0
$BR(\widetilde{\chi}_2^0 \to \widetilde{\ell}_L \ell)$	0.5	0
$BR(\widetilde{\chi}_2^0 \to \widetilde{\nu} \nu)$	0.5	0
$BR(\widetilde{\chi}_1^\pm \to \widetilde{\chi}_1^0 W^\pm)$	0	1
$BR(\widetilde{\chi}_2^0 \to \widetilde{\chi}_1^0 Z)$	0	1

injective. This fact, first systematically elucidated in the context of LHC searches by Arkani-Hamed *et al.* [83], is known as the LHC inverse problem. It has already been shown, for example, that conservation of R– and KK–parity respectively implies that both SUSY and MUED can yield $3\ell + \not{E}_T$. Although no BSM signals have been observed at the LHC thus far, it is of course critical to be prepared to "solve" the LHC inverse problem should the need arise.

A potential discriminator arises from spin considerations. Note that KK excitations have the same spin as their SM counterparts, but sparticles' spins differ by a half-unit. This fact leads to differences in the predicted form of angular distributions of the various decay products. Figure 2.11, reproduced from Moortgat-Pick *et al.* [84], illustrates this explicitly. This figure shows an example of the differing shapes of the jet opening angle distributions in inclusive dijet production in UED and SUSY.

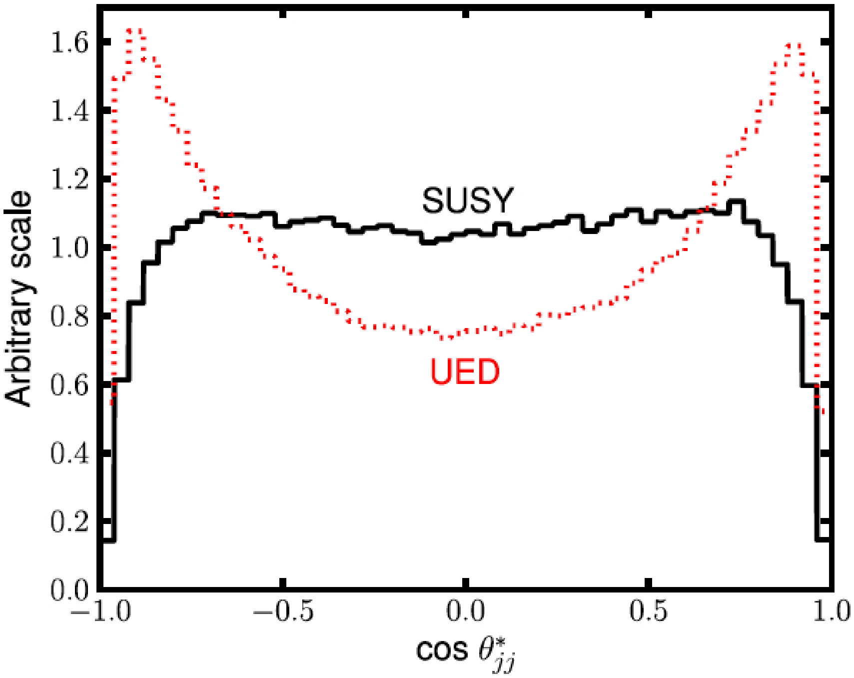

Figure 2.11: Parton-level jet opening angle distributions for dijet production in simulated SUSY and UED events at $\sqrt{s} = 14$ TeV with a sample mass spectrum taken from a minimal supergravity benchmark point.

Chapter 3

Overview of ATLAS

The data used in this analysis were collected with the ATLAS detector at the LHC in 2012. A brief description of this apparatus is presented in this chapter.

3.1 The Large Hadron Collider

The LHC [85] is a *pp* collider which is housed in a 27 km circumference tunnel at CERN on the France–Switzerland border. The tunnel was previously constructed for LEP and is located 50–175 m below ground. The 2012 dataset used in this analysis has been collected with $\sqrt{s} = 8$ TeV; this is the highest CM energy ever attained for collisions in a laboratory.

A series of increasingly energetic accelerators, culminating with the Super Proton Synchrotron (SPS), prepare protons for injection into the LHC ring. Upon injection, the beams are focused and steered by more than 1,600 superconducting quadrupole and dipole magnets operating at 1.9 K. The beam pipe features four interaction points (IPs) with design bunch crossing rates of 40 MHz, and around each such point a detector experiment has been constructed. Two of these, ATLAS and CMS [86], have similar physics programs entailing searches for general new physics and the Higgs boson. The remaining two detectors, LHCb [87] and ALICE [88], have somewhat more specialized programs. Figure 3.1 [89] shows a schematic of the LHC ring and the SPS. The positions of the four main detectors are also indicated in this figure.

To quantify the amount of data produced by a collider it is convenient to employ the concept of integrated luminosity. The instantaneous luminosity L is the constant of proportionality between a cross section and an event rate: $N = L\sigma$, and it is therefore often expressed in units of $\mathrm{b}^{-1}\mathrm{s}^{-1}$, where $1\ \mathrm{b} = 10^{-28}\ \mathrm{m}^2$. When radio frequency (RF) cavities are used to group protons into bunches within each beam, as is done at the LHC, L can be computed as follows [85]:

$$L = \frac{N_b^2 n_b f_{rev} \gamma_r}{4\pi \epsilon_n \beta^*} F, \tag{3.1}$$

where N_b is the number of particles per bunch, n_b is the number of bunches per beam, f_{rev} is the revolution frequency, γ_r is the protons' relativistic factor, ϵ_n is the transverse beam emittance, β^* is the optical beta function (distance from IP to double-width point), and F is a geometric reduction factor related to the beam crossing angle. The 2012 dataset delivered by the LHC had a peak instantaneous luminosity of $5.4\times10^{33}\ \mathrm{cm}^{-2}\mathrm{s}^{-1}$ [90], and, as can be seen in figure 3.2 [91], the total integrated luminosity recorded by ATLAS was 21.3 fb^{-1}. The distribution of the mean number of *pp* interactions per bunch crossing in 2012 is also displayed in figure 3.2 [91].

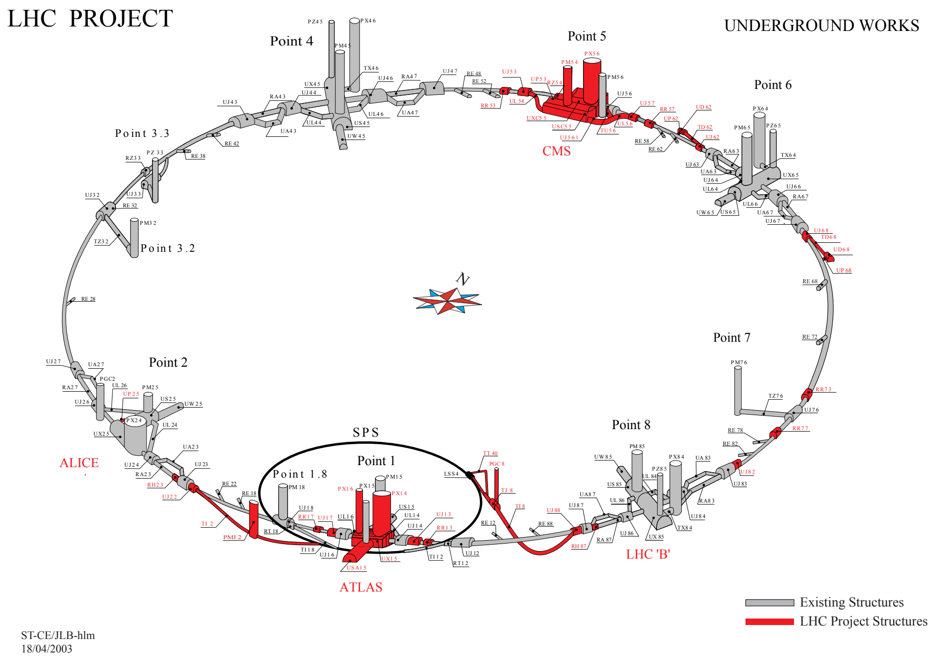

Figure 3.1: A schematic of the LHC which shows the locations of all major detector experiments.

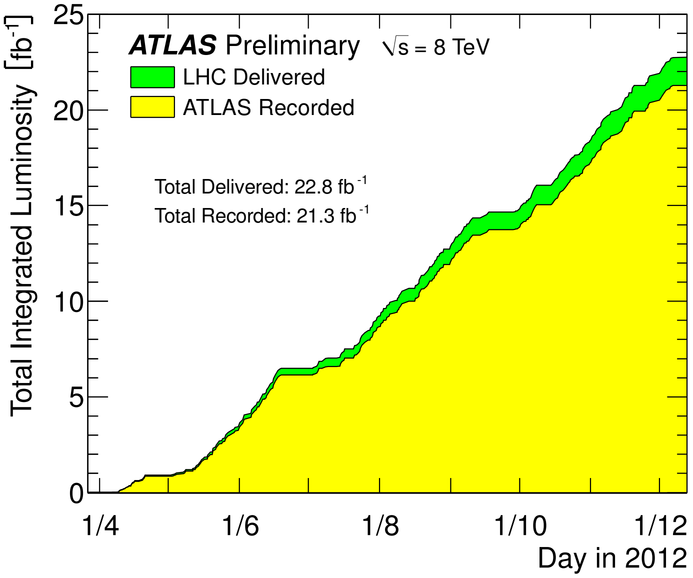

(a)

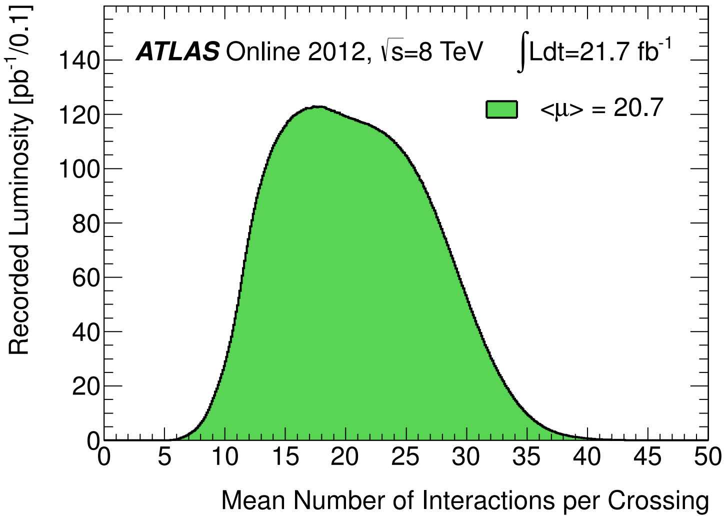

(b)

Figure 3.2: Integrated luminosity delivered by the LHC (green) and recorded by ATLAS (yellow) throughout 2012 (a) and average number of interactions per bunch crossing for the full 2012 dataset (b).

3.2 ATLAS Coordinate System

The ATLAS detector [92] [62] weighs roughly 7,000 tonnes. It measures 44 m in length and has a diameter of 25 m. It is therefore the largest collider detector ever constructed. The design philosophy of ATLAS is canonical for a general purpose detector. As shown in figure 3.3 [93], it features cylindrical, specialized subsystem layers of increasing radius centered around the IP and collinear with the beam pipe at the IP. The remaining sections in this chapter will systematically elucidate these subsystems, but it is first necessary to define the conventional coordinate system and describe some commonly encountered notation.

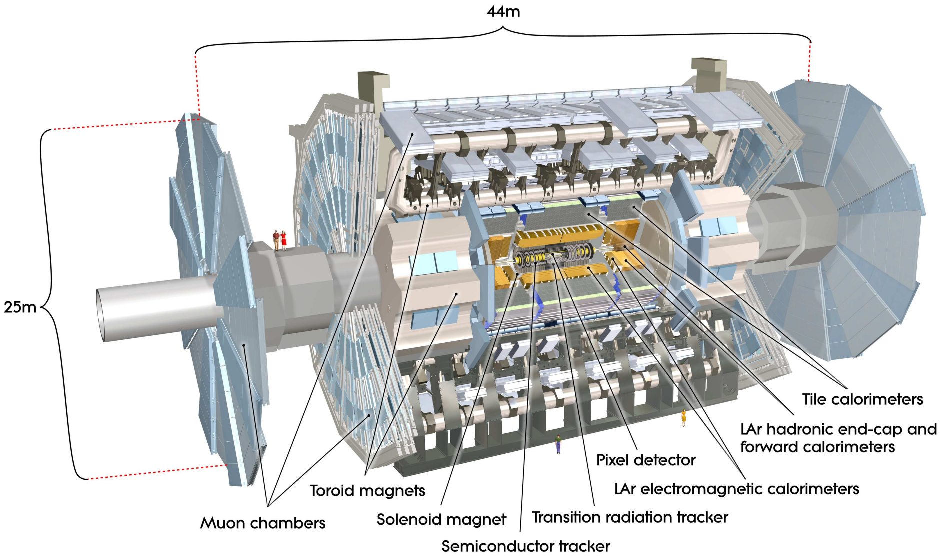

Figure 3.3: A schematic of the ATLAS detector.

By convention, the IP is taken to be at the origin of a right-handed Cartesian coordinate system (x, y, z). The axes are oriented so that the positive z-direction is aligned with the counter-clockwise beam and the x-axis points towards the center of the LHC. The xy-plane is called the transverse plane; points in this plane are often described with azimuthal polar coordinates

(r, ϕ). The angle measured from the z-axis is denoted by θ, but it is typically more convenient to work with the pseudorapidity[1]:

$$\eta \equiv -\ln \tan\left(\frac{\theta}{2}\right). \tag{3.2}$$

3.3 Inner Detector and Solenoid

The LHC beam pipe has a radius of 30 mm. After traversing this, the first ATLAS subsystem which particles encounter is the inner detector (ID) [94]. Covering a range $0.05 < r < 1.2$ m, $|\eta| < 2.5$, and $|z| < 3.1$ m, the ID is a tracking system which makes transverse momentum $\vec{p}_T \equiv (p_x, p_y)$ measurements with overall resolution $\frac{\sigma_{p_T}}{p_T} = 0.05\% \times p_T \oplus 1\%$[2][94]. Such measurements are possible because surrounding the ID is a $r = 1.3$ m solenoidal magnet with field strength ∼2 T (see figure 3.4 [93]) which induces transverse plane Lorentz curvature in charged particle tracks. Note that this also allows charge determination. As is illustrated in figure 3.4 [93], three distinct subsystems collectively comprise the ID. In order of increasing radius, these are the pixel detector, the semiconductor tracker (SCT), and the transition radiation tracker (TRT).

3.3.1 Pixel Detector

The pixel detector [94] is comprised of three barrel ($r = 50.5, 88.5, 122.5$ mm) and three endcap ($|z| = 495, 580, 650$ mm) layers, where each layer is itself comprised of 19×63 mm^2 sensors. Each sensor then contains 47,232 Si pixels—most of which measure $50 \times 400 \mu\text{m}^2$. These facts imply that the pixel detector has approximately $80{\times}10^6$ total readout channels.

The most important function of this subdetector is precision vertexing. Both this and the desire for low noise occupancy necessitates the large channel

---

[1] Pseudorapidity is a convenient quantity because for particles with speeds near c, η is approximately equal to rapidity y, and Δy is invariant under z-boosts.

[2] Whenever transverse momenta or energies appear on the RHS of resolution expressions in this chapter, the units are understood to be GeV.

multiplicity. The transverse and longitudinal resolutions of the various layers are between 10 and 115 μm [94], and together they average 3 hits per track with < 1 noise hit expected per bunch crossing.

3.3.2 Semiconductor Tracker

Consisting of four barrel layers ($r = 0.30, 0.37, 0.44, 0.51$ m) and nine endcap layers ($0.81 < |z| < 2.8$ m), the SCT [94] is the most important subdetector for charged particle tracking. A layered sensor array design philosophy was carried over from the pixel detector, but each SCT sensor is a more cost-effective collection of 1,500 12 cm×80 μm strips of Si. This gives a total of 6.3×10^6 readout channels.

Although the use of strips degrades the spatial resolution slightly with respect to the pixel detector (17 μm transverse and 580 μm longitudinal [94]), it enables the SCT to occupy a much larger volume. Tracks can therefore have as many as 8 hits, thereby providing robust tracking information. The SCT and pixel detector utilize a common cooling system and nominally operate at 266 K.

3.3.3 Transition Radiation Tracker

When a charged particle moves between media with differing dielectric constants, it emits so-called transition radiation and thereby loses an amount of energy proportional to its relativistic factor γ [95]. This is the principle which underlies transition radiation detectors such as ATLAS' TRT ($0.55 < r < 1.1$ m, $|z| < 2.7$ m) [93].

TRT detector elements are 2 mm radius drift chambers known as straws. The straws are oriented parallel to ATLAS in the barrel (lengths: 144 cm) and radially in the endcaps (lengths: 37 cm), and are each filled with a 70% Xe, 27% CO_2, 3% O_2 gas mixture. Xenon is an ideal choice because of its high efficiency for transition radiation absorption. A gold-plated wire runs down the central longitudinal axis of each straw. A potential difference

-1530 V is set up across each wire so that the ionized electrons from the gas produce an electrical pulse which is read out at the end of the straw. The pattern of straws registering such ionization pulses gives tracking information with transverse resolution 130 μm [93]. Although this is slightly coarser than the pixel detector and the SCT, the comparatively large volume of the TRT provides an average of 30 hits per track. Also noteworthy is the fact that regions between TRT straws are filled with polypropylene to encourage large amounts of electron transition radiation. This implies that the TRT is also able to identify electrons.

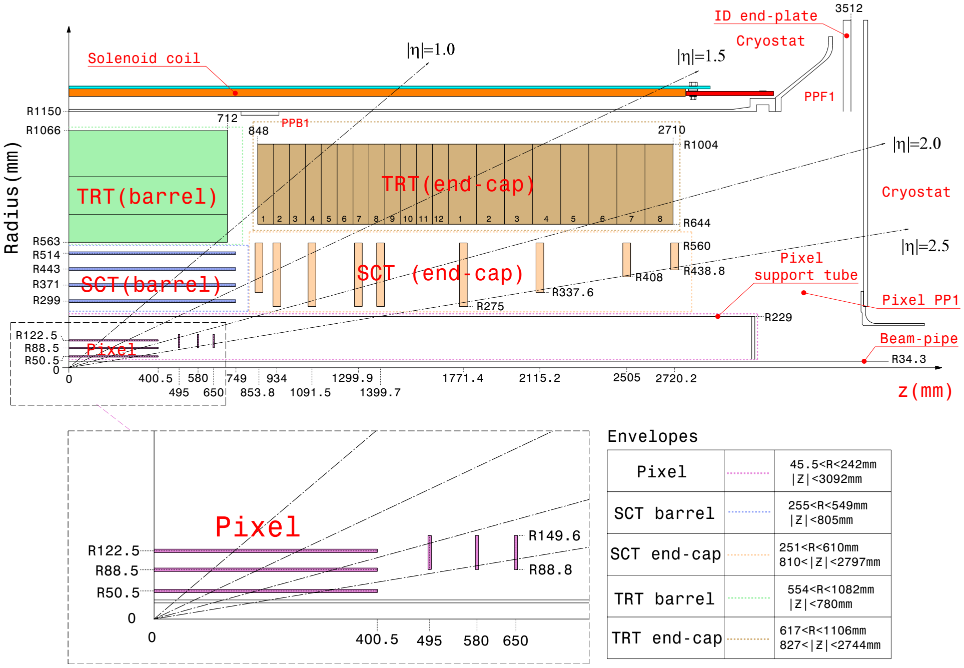

Envelopes

Pixel	⋯	45.5<R<242mm |Z|<3092mm
SCT barrel	⋯	255<R<549mm |Z|<805mm
SCT end-cap	⋯	251<R<610mm 810<|Z|<2797mm
TRT barrel	⋯	554<R<1082mm |Z|<780mm
TRT end-cap	⋯	617<R<1106mm 827<|Z|<2744mm

(a) ID schematic

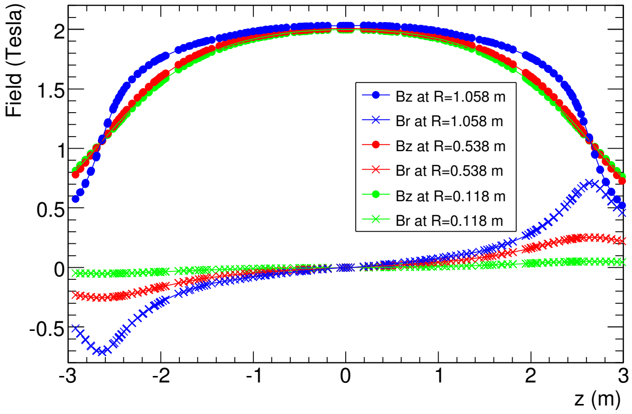

(b) Solenoidal B field

Figure 3.4: A schematic showing various dimensions of the three ID subdetectors (a), and a plot of the z- and r-components of the solenoidal magnetic field (b).

3.4 Calorimeters

After passing through the ID and its associated solenoid, particles enter the energy measurement portion of ATLAS: the calorimeter system ($1.4 < r < 4.25$ m, $|\eta| < 4.9$) [93]. Particle physics calorimeters function by destructively interacting with incident particles, thereby initiating a series of iterative decays collectively called a shower. The properties of showers, which can broadly be classified as electromagnetic or hadronic, can then be measured and used to reconstruct the energy and location of the original particle.

As can be seen in figure 3.5 [93], the calorimetry strategy employed by ATLAS involves liquid argon (LAr) sampling EM calorimeters in the barrel and endcap (ECal), a tile hadronic calorimeter in the barrel (HCal), LAr hadronic endcaps (HEC), and a LAr combined EM–hadronic calorimeter in the forward region (FCal). Each of these subsystems has been designed with a balance between robust (η, r, z) coverage, high energy resolution, and cost-effectiveness in mind. The amount of calorimeter material (measured in interaction lengths) presented to an incident particle is histogrammed in figure 3.5 [93].

3.4.1 Electromagnetic

EM showers occur when electrons and photons iteratively undergo bremsstrahlung and e^+e^- pair-production, respectively, in dense material. EM calorimeters are specialized instruments which allow energy measurements to be extracted from measurements of the properties of showers of this type.

The ATLAS ECal is constructed from alternating layers of lead and liquid argon; such an arrangement is called a Pb–LAr sampling calorimeter. Lead is an ideal choice for an absorber because its high density encourages development of EM showers. The particles in the shower then ionize the LAr, and the amount of ionization is measured with Cu electrodes and subsequently mapped to an incident energy. The Pb absorbers are arranged in an accordion-like pattern to allow full azimuthal (ϕ) coverage. The ECal achieves a resolution $\frac{\sigma_E}{E} = \frac{10\%}{\sqrt{E}} \oplus 0.7\%$ [93] and covers a pseudorapidity range $|\eta| < 1.5$ ($1.4 < |\eta| < 3.2$) in the barrel (endcap). Its radial extent is $1.4 < r < 2$ m.

Both EM and hadronic (see below) calorimetry are performed by the FCal, which extends $3.1 < |\eta| < 4.9$. The EM subsystem within the FCal is a Cu–LAr sampling calorimeter with energy resolution $\frac{\sigma_E}{E} = \frac{100\%}{\sqrt{E}} \oplus 10\%$ [93]. Copper has been chosen to facilitate heat removal in the high particle flux regions.

3.4.2 Hadronic

When a hadron is incident on dense material a hadronic shower may be initiated. These showers can contain both strongly and electromagnetically interacting particles (mostly pions [96]). Note that this is distinct from the process of hadronization, which creates jets of colorless hadrons from partons due to confinement, but hadronic calorimeters are necessary to measure jet energies.

ATLAS' hadronic calorimeters are located in the barrel (HCal coverage: $|\eta| < 1.7$, $2 < r < 4$ m), endcaps (HEC coverage: $1.5 < |\eta| < 3.2$), and forward region (FCal coverage: $3.1 < |\eta| < 4.9$) which gives good hermeticity. Each subsystem attains resolution $\frac{\sigma_E}{E} = \frac{X\%}{\sqrt{E}} \oplus Y\%$, with $X = 56.4, 50, 100$ and $Y = 5.5, 3, 10$ [93] for the HCal, HEC, and FCal, respectively.

The HCal is a sampling calorimeter with steel absorbers and scintillating plastic tile samplers.[3] Both the HEC and the hadronic subsystem of the FCal are LAr sampling calorimeters. The former (latter) utilizes Cu (W) absorbers. As was seen in the material thickness plot in figure 3.5, all of the hadronic calorimeters are comprised of 3-4 layers of absorbers in order to mitigate any punch-through into the muon system.

---

[3] For this reason it is also commonly referred to as the tile calorimeter

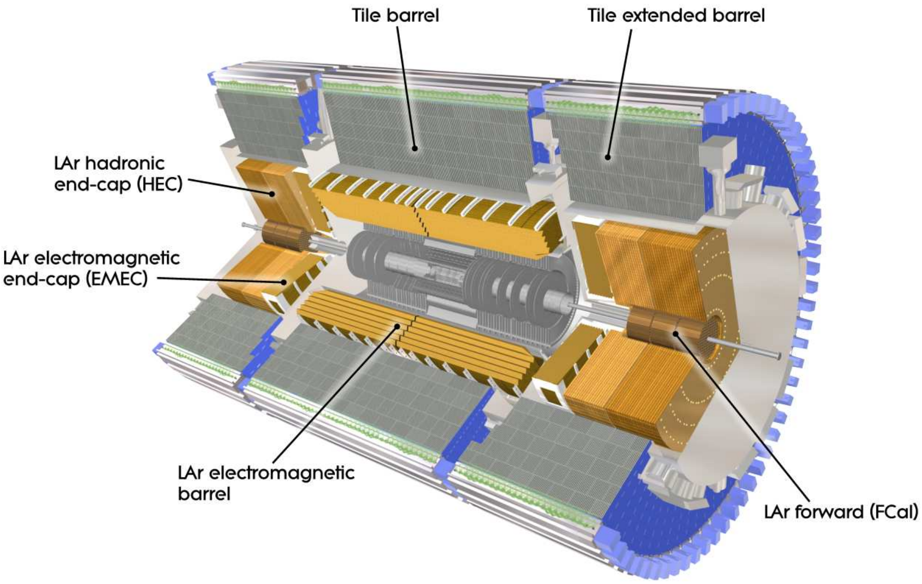

(a) Calorimeters

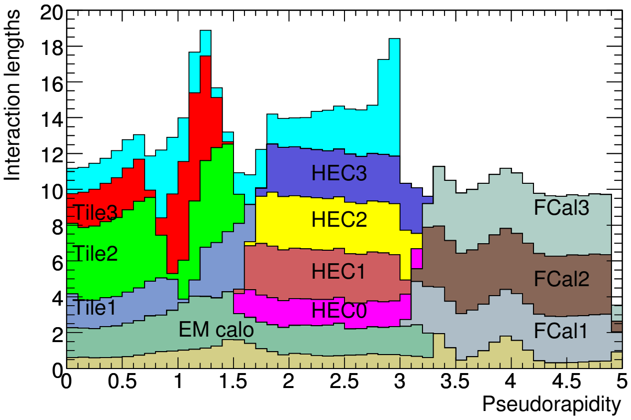

(b) Calorimetric interaction lengths

Figure 3.5: A schematic showing the EM and hadronic calorimeters (a), and a stacked histogram of the amount of calorimetric material in units of the relevant materials' interaction lengths (b). The unlabeled brown (blue) histogram in (b) corresponds to the pre-sampler (material between the calorimeters and MS).

3.5 Muon Spectrometer and Toroidal Magnets

Filling the volume between $4.3 < r < 11$ m and $|\eta| < 2.7$, the muon spectrometer (MS) [93] provides dedicated tracking and trigger (see below) information for muons.

Muon p_T measurements are inferred from $r - z$ track curvature in the presence of ATLAS' eponymous air-core toroidal magnet system. This system consists of 8 toroid coils in the barrel (endcap) which collectively produce a field of roughly 0.5 T (1 T) while operating at 4.6 K. Each set of ϕ-symmetric endcap toroids is rotated by 22.5° with respect to the ϕ-symmetric barrel set to ensure optimal bending power and coverage. The toroid configuration is shown in both subfigures of figure 3.6 [93].

Transverse momentum resolution of 10% for 1 TeV tracks within $|\eta| < 2.7$ [93] is attained through use of two subdetectors: cathode strip chambers (CSC) in the endcaps, and monitored drift tubes (MDT) in both the barrel and endcaps. Both of these systems are illustrated in figure 3.6.

Like the TRT, the MDT is a collection of straws filled with ionizing gas (93% Ar, 7% CO_2) and threaded with Au-plated wire for signal transmission. In the barrel, longitudinally oriented straws $\leq$6 m in length are grouped into three layers ($r = 5, 7.5, 10$ m) of 16 chambers ("stations") each. Endcap MDTs are similarly grouped into four layers ($|z| = 7.4, 10.8, 14, 21.5$ m) which together give ATLAS its characteristic shape (see figure 3.6).

Particle counting rates are too large for proper MDT performance when $|\eta| > 2.0$ and $|z| = 7.4$ m. For this innermost endcap region, then, CSCs are used instead of MDTs. Similarly to MDTs, these are segmented azimuthally into chambers. However, their operation relies on measurement of induced charges on cathode strips rather than straw wire read-outs.

Muon trigger capabilities are provided by resistive plate chambers (RPC) and thin gap chambers (TGC) for $|\eta| < 2.4$. The next section provides further details on the trigger system.

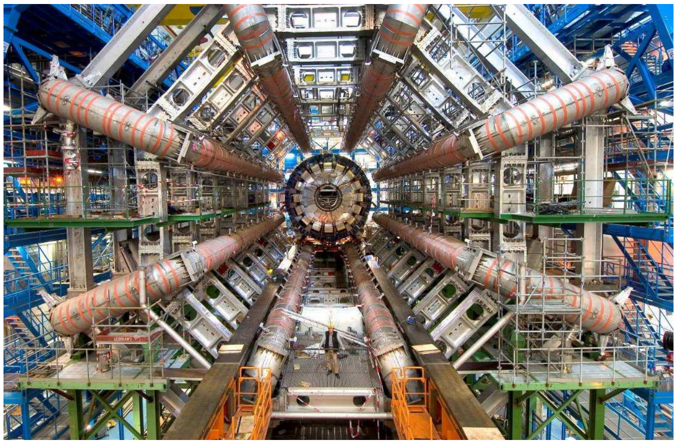

(a) Barrel toroids

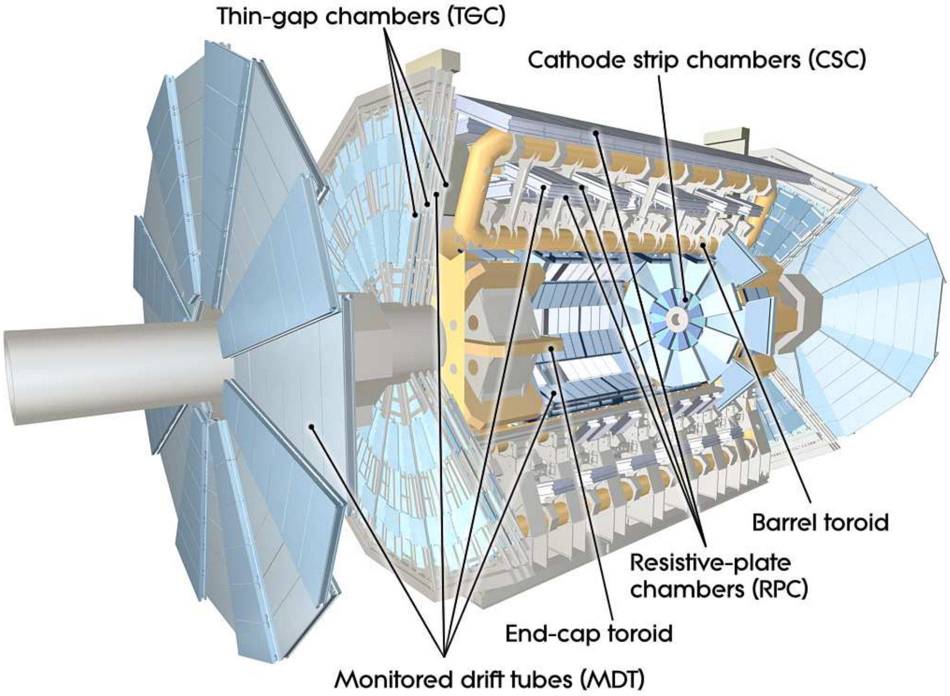

(b) MS and toroid system schematic

Figure 3.6: A photograph showing the orientation of the barrel toroids (a). The ID, solenoid, calorimeters, and MS are not present in this photo. Subfigure (b) shows a schematic of the major MS components and the toroid system.

3.6 Trigger

Data are output from all subdetectors in the form of electrical signals; *e.g.* pulses from TRT anode wires. The trigger and data acquisition system (TDAQ) [93] collects these signals, scrutinizes them via a variety of algorithms, and finally stores events of interest for physics analysis.

Storing a raw collision event observed by ATLAS requires roughly 25 MB, but this can be reduced to 1.3 MB with zero suppression [97]. Given that the LHC bunch crossing rate was 20 MHz (50 ns temporal spacing) in 2012, it is clearly not feasible to store every crossing event. In addition to its impracticality, it turns out that storing all events would not be useful for the ATLAS physics program.

At 7 TeV the inclusive inelastic pp scattering cross section was measured by ATLAS to be 60.3 ± 2.1 mb [98]. As can be seen in figure 3.7 [99], typical cross sections for SM processes of interest are on the order of 10–100 pb at this same CM energy. New physics cross sections may be considerably smaller than this. The disparity between these cross sections implies that the vast majority of pp interactions lead to soft "minimum bias" events. These processes are irrelevant for most ATLAS analyses and can safely be discarded (or, rather, heavily pre-scaled—see below). The automated mechanism for deciding which events will be stored for later analysis is precisely the trigger system. Because the present analysis is focused on extremely rare processes involving final states with three leptons, the large event rate reduction afforded by the trigger is of critical importance.

Given physical storage limitations, a practical data throughput rate was found to be $\sim$300 MB/s, although it can be as high as 600 MB/s in certain runs [97]. The ATLAS trigger's main goal, then, is to select approximately 200 events from the $20{\times}10^6$ produced each second. This reduction is achieved by dividing the trigger functionality into three sequential levels with access to increasingly detailed event properties: L1, L2, and the event

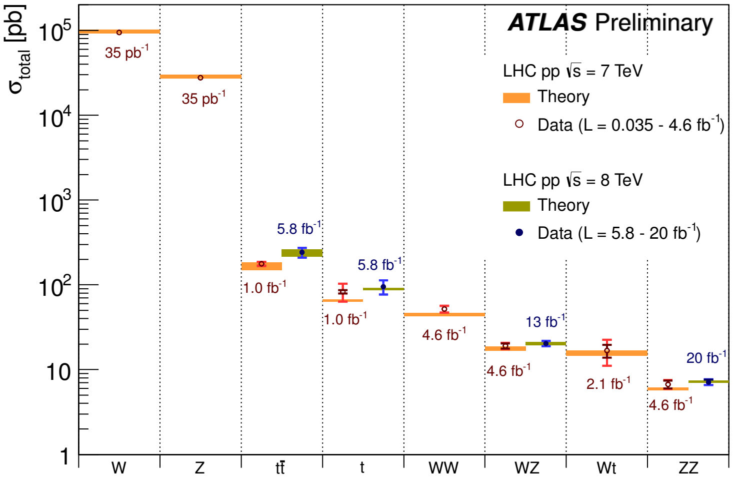

Figure 3.7: ATLAS cross section measurements compared to theory at 7 and 8 TeV for various SM production modes of interest. Note that these are much smaller than the inelastic cross section 60.3 mb.

filter (EF).

The largest event rate reduction 20 MHz→ 75 kHz occurs via the custom-built hardware which comprises L1. This receives input from the RPC, TGC, and calorimeters, and has a maximum of 3 μs to identify so-called regions of interest (ROI) containing hard leptons, jets, large $\not{E}_T$, or large E_T. If an event contains an ROI it becomes input for L2.

Both L2 and the EF[4] are software-based and are located in a dedicated facility near the detector at CERN. L2 is a farm of 500 CPUs which receive input from L1 and the ID. It performs a limited reconstruction (see the next chapter) within the ROI and must make event decisions in less than 40 ms. If an ROI satisfies certain properties, codified in so-called trigger sequences, the event is passed to the EF at a rate 3.5 kHz. The EF is then afforded 4 s in which to employ sophisticated algorithms to fully rebuild and analyze

---

[4] L2 and EF are collectively called the high-level trigger (HLT)

an event. This level is comprised of 1,800 CPUs and the rate reduction is 3.5 kHz→ 200 Hz. EF is the final arbiter as to which events are stored to disk; its output is a summary of all trigger information called a trigger chain. The collection of all trigger chains is known as the trigger menu, and this is completely customizable. Pre-scale factors can be set at each level to further control throughput. These are factors which forcibly reduce the acceptance of a given chain by a factor $\frac{1}{n}$. This is achieved by keeping one event for every n which are successfully triggered upon.

All events satisfying a chain from the menu are disseminated to collaboration members via the LHC Computing Grid [100]. Some explicit chain examples will be presented in chapter 6 when the event selection for this analysis is described.

Chapter 4

Reconstruction and Identification of Physics Objects

Having described the BSM scenarios of interest and the detector used to search for these, focus will now begin to shift to the particulars of the analysis. This chapter briefly describes standard ATLAS reconstruction and identification techniques leading to experimental definitions of the necessary physics objects: electrons, muons, jets, and $\not\!\!E_T$. Because of the rarity of multilepton events at the LHC, lepton identification plays a key role in this analysis. The performance of these algorithms will be summarized. The selection criteria used for each object in the present analysis are then described in detail. Note that the term "lepton" should, unless otherwise indicated, be understood to mean $e^{\pm}$ or $\mu^{\pm}$ for the remainder of this thesis.

4.1 Electrons

This section will present the performance of the standard electron reconstruction and identification algorithms. Electron cuts specific to this analysis will then be presented.

4.1.1 Reconstruction and Identification

The process of establishing that an electron candidate has passed through a particle detector and the subsequent measurement of components of its four-momentum is called electron reconstruction. There is a standard ATLAS algorithm used for this purpose [101].

In the central region ($|\eta| < 2.5$), the first step towards reconstruction is recognition of EM calorimeter energy clusters. This is achieved with a "sliding window" algorithm [102], wherein a window of size 3×5 units (where a unit is 0.025×0.025 in (η, ϕ)) is swept across the ECal to find local E_T maxima. This algorithm identifies EM showers with ∼100% efficiency when $E_T > 15$ GeV. ID information is then used to match these clusters to a track. If a cluster and a track are found to match within $\Delta\eta < 0.05$ and $\Delta\phi < 0.1$ at the track point of impact, electron reconstruction proceeds to the next step: energy determination. This is achieved by summing contributions from the ECal cluster cells identified by the sliding window, the pre-sampler estimate of the amount of energy lost by the candidate before reaching the ECal, estimated leakage outside the cluster, and an estimate of any punch-through energy loss. The transverse momentum components are obtained from the ID track curvature measurement in the solenoidal B field. Of course, there are no ID trackers in the far-forward region $2.5 < |\eta| < 4.9$, so a slightly different algorithm is used here; three-dimensional clusters provide the desired four-momentum reconstruction. The average efficiency of electron reconstruction was measured to be $98.7 \pm 0.1 \pm 0.2\%$ in data; this is illustrated in figure 4.1 [101].

In the present analysis, the electrons of interest are hard, isolated, and prompt[1]. Many electrons incident upon ATLAS—*e.g.* those from photon conversions, Dalitz decays, and jets—do not fit these criteria. Electron identification is the process by which these less desirable electrons are discarded, leaving a sample heavily enriched in electrons of interest. This is achieved by

---

[1] "Hard" means high p_T. Isolation will be described in detail below. "Prompt" means that the electron originates from the primary vertex.

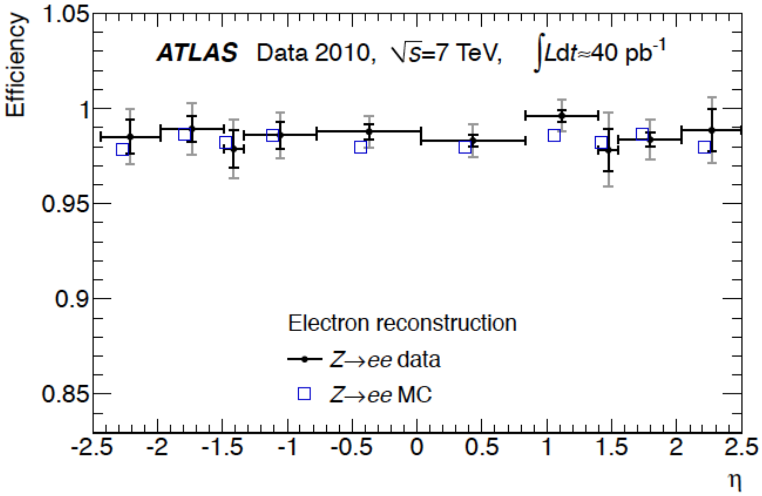

Figure 4.1: Full η-dependence of the ATLAS electron reconstruction efficiency as measured in $Z \to ee$ decays in both data and simulation. The average value is 0.987.

applying a series of cuts to the full set of reconstructed candidate electrons. ATLAS employs three standard identification working points reflecting the desired level of purity to be attained: loose, medium, and tight [101]. This analysis makes use of medium and tight electrons.

Loose electrons are identified using variables defined only in terms of ECal measurements. These are mostly comprised of variables characterizing the shower shape. Medium electrons additionally include tracking information. Cuts on track quality are imposed, such as requiring the transverse impact parameter to satisfy $|d_0| < 5$ mm (to reduce electrons from secondary vertices), and enforcing minimum pixel and SCT hit multiplicities (to improve the track fits). Tight electrons impose further restrictions on track quality, *e.g.* minimum TRT hit multiplicities, and track–cluster matching. The efficiency of the identification working points has been measured in data using samples enriched in $W \to e\nu$, $Z \to ee$, and $J/\psi \to ee$ [101]. Although there is some dependence on E_T and η, the medium (tight) efficiency was found to be roughly 0.85 (0.78).

In addition to the efficiency measurements described above, corresponding MC simulated values were obtained [101]. Small differences, typically 1-2%, were observed. These differences are used to multiplicatively correct MC simulations used in this analysis on an event-by-event basis. These samples are described in chapter 5.

4.1.2 Additional Selection Cuts

The working points described in the previous section are the standard benchmark for electron definitions across all ATLAS analyses. The present analysis incorporates a series of additional identification cuts. As will be shown later, the background (BG) estimate methodology requires the definition of two categories of electrons: baseline and signal.

Baseline Electrons

The starting point for defining baseline electrons is the set of medium identification criteria. A transverse energy cut $E_T > 10$ GeV is then applied. Calorimeter clusters are required to satisfy $|\eta| < 2.5$ to ensure that the central reconstruction algorithm has been used. There are known regions of the ECal with dead optical transmitters; clusters in these areas are discarded. Finally, after passing through the overlap removal scheme (*cf.* section 4.4), electrons are deemed baseline.

Signal Electrons

Signal electrons are the electrons of interest in this analysis. These are baseline electrons which satisfy a number of additional cuts.

Two isolation requirements are imposed. The variable p_T^{cone30} is defined to be the scalar sum of transverse momenta of all > 1 GeV tracks (except those of other baseline leptons) within $\Delta R \equiv \sqrt{\Delta\eta^2 + \Delta\phi^2} \leq 0.3$ of a baseline electron track. An analogous variable E_T^{cone30} may then be defined in terms of ECal clusters rather than tracks. Note also that E_T^{cone30} has a pile-up correction applied: $E_T^{cone30} \rightarrow E_T^{cone30} - AN_v$, where $A = 20.15$ (17.94) MeV in data (MC), and N_v is the multiplicity of ≥ 5 track vertices in the event. These corrections have been computed empirically by examining the average isolation as a function of the number of primary vertices in both data and simulations. The two isolation requirements are $p_T^{cone30} < 0.16E_T$ and $E_T^{cone30} < 0.18E_T$.

Two additional perigee parameter cuts are then placed to reduce non-prompt electrons. The d_0 significance is required to satisfy $|d_0|/\sigma_{d_0} < 5$, and the longitudinal impact parameter must satisfy $|z_0 \sin\theta| < 0.4$ mm. If, in addition to all of these cuts, the electron passes the tight identification selection, it is deemed signal.

4.2 Muons

Since muons are minimum ionizing particles which do not undergo significant showering in the calorimeters, muon reconstruction algorithms differ from their electron counterparts. Performance of these algorithms will be summarized and the muon selection cuts for this analysis will then be presented.

4.2.1 Reconstruction and Identification

Muon reconstruction happens via two distinct and complementary sets of algorithms ("chains"): staco (statistical combination) and muid (muon identification). Each chain is comprised of three algorithms, and each of these returns one of three[2] muon types [103]:

- Standalone muons are reconstructed entirely from MS tracking information. Track segments from the three muon stations are constructed, combined to form a single track, and then extrapolated to the IP.

---

[2] There is a fourth, less commonly used type of muon which is reconstructed using minimum ionization clusters from the ECal.

The staco (muid) algorithm which returns standalone muons is called muonboy (Moore).

- Reconstruction of combined muons involves spatially matching independently reconstructed ID tracks and MS tracks. Since this type of muon has the highest purity, both chains derive their names from the algorithms which return them. The overall vector of perigee parameters $\vec{T}$ is obtained by staco in the following form [103]:

  $$\vec{T} = (C_{ID}^{-1} + C_{MS}^{-1})^{-1}(C_{ID}^{-1}\vec{T}_{ID} + C_{MS}^{-1}\vec{T}_{MS}), \tag{4.1}$$

  where $\vec{T}_i$ and C_i are the vectors of track parameters and their associated covariance matrices, respectively, obtained from subsystem i. This shows that staco, as its name suggests, performs a statistical combination of the ID and MS measurements. The muid approach is to perform a global χ^2-minimizing refit across all track hits from both subdetectors.

- Segment tagged (or, more concisely, tagged) muons are seeded by ID tracks. These tracks are extrapolated to the MS, accounting for energy loss, and a spatially matching tracklet is then sought in the first MS station. The staco (muid) chain makes use of an algorithm called mutag (mugirl).

The standard muons for ATLAS analyses are those returned by the staco chain. This analysis makes use of combined and tagged staco muons. The reconstruction efficiency for both types has been measured in a $> 99.9\%$ pure sample of $Z \to \mu\mu$ decays [104]. As can be seen in figure 4.2 [104], the efficiency is nowhere less than 0.98 in the central region $|\eta| < 2.5$. Note that there are small efficiency differences between the measurement and the MC prediction. As in the electron case, these discrepancies are accounted for by correcting MC event weights with a scale factor ϵ_D/ϵ_{MC}. The largest such discrepancy occurs at $\eta \sim 1.5$ and was caused by a well understood mis-modeling of the reconstruction efficiency in the ID [104].

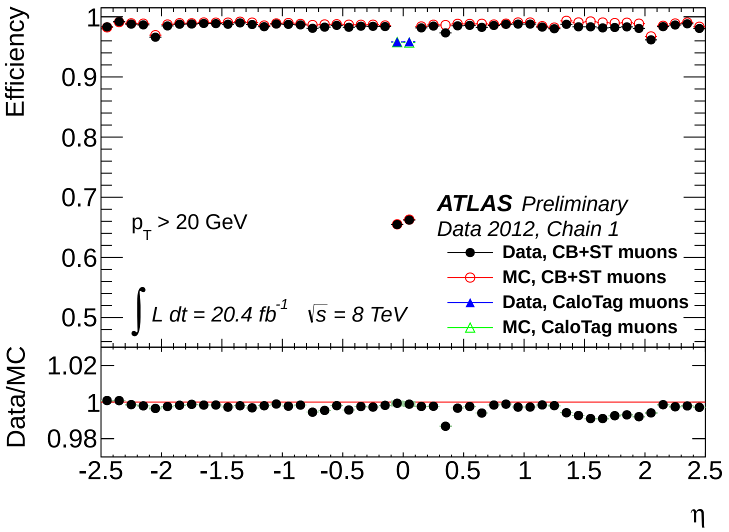

Figure 4.2: η-dependence of the ATLAS muon reconstruction efficiency as measured in $Z \to \mu\mu$ decays in both data and simulation. The efficiency is shown for both combined (CB) and tagged (ST) muons.

Similarly to electrons, muons of interest are identified with loose, medium, and tight sets of identification cuts for both staco and muid [105]. This analysis adopts the loose working point along with a set of customized identification cuts which will now be described.

4.2.2 Additional Selection Cuts

Baseline Muons

Baseline muons are defined to be loose staco combined or tagged muons satisfying several additional criteria. The transverse momentum must satisfy $p_T > 10$ GeV and the pseudorapidity must obey $|\eta| < 2.40$. A number of pixel and SCT track hit restrictions are then imposed: $n_b > 0$, $n_p > 1$, $n_{SCT} > 5$, and $n_h < 3$, where n_b is the number of b-layer (an inner layer of the pixel tracker which improves impact parameter resolution) hits, n_p is the number of overall pixel hits, n_{SCT} is the number of SCT hits, and n_h is the number of pixel and SCT track holes (*i.e.* missing expected measurements). TRT outliers are defined to be either isolated straw pulses or TRT tracks which do not spatially match a track from the pixel and SCT. In this analysis, the following restriction is placed on the TRT outlier multiplicity n^o_{TRT}:

$$\begin{aligned} \text{if} \quad & 0.1 < |\eta| < 1.9: \; n > 5 \text{ and } n^o_{TRT} < 0.9n \\ \text{else if} \quad & (|\eta| < 0.1 \text{ or } |\eta| > 1.9) \text{ and } n > 5: \; n^o_{TRT} < 0.9n, \end{aligned}$$

where n is the total number of TRT hits including outliers: $n = n_{TRT} + n^o_{TRT}$.

Note that p_T is used for identification here instead of E_T as was done for electrons. The lack of calorimeter information necessitates this. Recalling the resolutions of the ID and ECal given in chapter 3, it is clear that E_T measurements are more precise for hard objects and are therefore preferable when a choice is available.

Signal Muons

After overlap removal, signal muons are then required to satisfy additional track quality requirements: $\frac{|d_0|}{\sigma_{d_0}} < 3$, and $|z_0 \sin\theta| < 1$ mm. An isolation cut is also imposed: $p_T^{cone30} < 0.12 p_T$, where p_T^{cone30} is vertex corrected: $p_T^{cone30} \to p_T^{cone30} - AN_v$, with $A = 10.98$ (6.27) MeV in data (MC).

4.3 Jets

Jet reconstruction at ATLAS begins with recognition of topological clusters (topoclusters) in the HCal [102]. These are iteratively constructed clusters in which neighboring calorimeter cells are included if their read-out energies are significantly larger than the known noise threshold. Topoclusters therefore have variable size and shape, which differentiates them from the sliding window-based clusters of the ECal described in section 4.1.

In general, a jet is expected to deposit several topoclusters. With this in mind, the anti-k_t jet clustering algorithm [106] takes all topoclusters from an event as input and returns a set of reconstructed jet objects. This is achieved by defining a metric which incorporates both energy and geometrical information:

$$d_{ij} \equiv \min\left(E_{Ti}^{-2}, E_{Tj}^{-2}\right) \frac{\Delta R_{ij}^2}{R^2}, \tag{4.2}$$

where i, j are cluster indices, and $R = 0.4$ in this analysis. This metric naturally clusters soft particles around hard particles. The algorithm then proceeds by iteratively grouping topoclusters into jets based upon their d_{ij} values [107].

In order to map calorimeter signals to jet energies, it is necessary to perform a calibration to determine the jet energy scale (JES). This can be achieved in a number of ways; *e.g.* by comparing the calorimeter read-out to the tracked momenta of isolated single particles [108]. The JES for the central region of the tile calorimeter is known within 4% for jet $p_T > 20$ GeV.

A number of identification cuts are applied to the jets in this analysis. Baseline jets are required to satisfy $p_T > 20$ GeV and $|\eta| < 4.5$. Overlap removal is then performed. Signal jets are then selected by imposing $|\eta| < 2.5$ and a requirement on the jet vertex fraction (JVF). The JVF is a quantity defined, for each jet J_i and vertex V_j, as follows [109]:

$$\mathrm{JVF}(J_i, V_j) \equiv \frac{\sum\limits_k p_T(T_k^{ij})}{\sum\limits_{n,\ell} p_T(T_\ell^{in})}, \tag{4.3}$$

where T_k^{ij} is the kth track associated with J_i that has been matched to V_j. In this analysis each signal jet is required to satisfy JVF(J_i,PV)>0.5, where PV is the primary vertex. This means that at least half of the jet's tracked p_T must be traceable to the PV, which is useful for pile-up suppression.

Because they are one of the main products of t quark decays, b-jets are of particular importance to this analysis. To wit, it will be shown later that vetoing events with > 0 b-jets provides good suppression of t and $t\bar{t}$ SM backgrounds. Identification of b-jets, also called b-tagging, typically relies on the presence of a displaced vertex due to the long lifetimes of B hadrons. The present analysis uses the MV1 algorithm [110] which identifies b-jets with 0.85 efficiency; this algorithm passes inputs from other b-taggers into a neural network. In particular, MV1 receives input from track–based, secondary vertex–based, and shower shape–based taggers. The signal jet kinematic cuts listed above have been chosen in accord with this algorithm's requirements. MC event weights are corrected with multiplicative b-tag efficiency scale factors derived from data; this is analogous to the lepton reconstruction scale factors described above.

4.4 Overlap Removal Scheme

Several references have been made above to an overlap removal scheme to which baseline electrons, muons, and jets are subject before the signal objects are defined. The purpose of such a scheme is to mitigate any undesired duplication between the reconstructed lepton objects or the between the leptons and jets. This procedure will now be described.

- If two electrons i and j satisfy $\Delta R_{i,j} < 0.1$, discard the softest of these.
- If an electron and a jet satisfy $\Delta R_{e,j} < 0.2$, discard the jet.
- If, after the above e–j overlap removal, a lepton and a jet satisfy $\Delta R_{\ell,j} < 0.4$, discard the lepton.
- If an electron and a muon satisfy $\Delta R_{e,\mu} < 0.1$, discard them both.

4.5 Missing Transverse Momentum

Conservation of momentum in the transverse plane and the hermetic design of ATLAS imply that a significant imbalance in measured $\vec{p}_T$ can be attributed to particles which have escaped the detector—say, neutrinos or perhaps $\tilde{\chi}_1^0$. This notion is made more precise by the definition of the missing transverse momentum two-vector [111]:

$$\vec{\not{E}}_T = -\sum_i \vec{p}_T^{\,i}, \tag{4.4}$$

where summation is over the set of observed particles. The missing transverse momentum[3] is then defined to be the norm of this vector $\not{E}_T = \sqrt{\not{E}_{Tx}^2 + \not{E}_{Ty}^2}$.

The standard ATLAS definition of this quantity for use in analyses is [112]:

$$\vec{\not{E}}_T = \vec{\not{E}}_T^{\,calo} + \vec{\not{E}}_T^{\,cryo} + \vec{\not{E}}_T^{\,\mu}, \tag{4.5}$$

where the calorimeter term $\vec{\not{E}}_T^{\,calo}$ describes calorimetric contributions, the cryostat term $\vec{\not{E}}_T^{\,cryo}$ accounts for energy loss in the cryostat material between the ECal and tile calorimeter, and the muon term $\vec{\not{E}}_T^{\,\mu}$ includes muonic contributions. Some comments about these terms will now be made.

The calorimeter term has components

$$\vec{\not{E}}_T^{\,calo} = -\sum_i^{N_{cell}} E_i \begin{pmatrix} \sin\theta_i \cos\phi_i \\ \sin\theta_i \sin\phi_i \end{pmatrix} \tag{4.6}$$

where E_i is the energy of the ith calorimeter cell whose angular position is specified by θ_i and ϕ_i. The sum runs over all cells belonging to calorimeter clusters. Comparing this to equation 4.4 reveals that the ultra-relativisitc approximation ($E \sim p$) is being used to write energies instead of momenta. In the literature these two quantities are therefore often interchangeably labeled and named with impunity in the context of $\not{E}_T$ discussions.

More refined calorimeter term measurements are obtained by using information from reconstructed physics objects. To this end, the term is broken

---

[3] $\vec{\not{E}}_T$ is also commonly referred to as the missing transverse energy vector. Its norm is then also referred to as the missing transverse energy. See also the discussion following equation 4.6

up into object-specific contributions as follows:

$$\vec{\not{E}}_T^{\,calo,calib} = \vec{\not{E}}_T^{\,e} + \vec{\not{E}}_T^{\,\mu,calo} + \vec{\not{E}}_T^{\,\gamma} + \vec{\not{E}}_T^{\,j} + \vec{\not{E}}_T^{\,CO}, \tag{4.7}$$

where the superscript *calib* indicates that contributions of each of these terms are drawn from the corresponding energy measurements obtained by the calibrated reconstruction algorithms for each indicated object. The calorimeter muon term $\vec{\not{E}}_T^{\,\mu,calo}$ parameterizes the minimum ionization energy deposited by muons in the calorimeters. The so-called cell out term $\vec{\not{E}}_T^{\,CO}$ collects cells which were not associated with an object during reconstruction. $\vec{\not{E}}_T^{\,calo,calib}$ replaces $\vec{\not{E}}_T^{\,calo}$ in equation 4.5.

The muon term in equation 4.5 is simply defined to be the negative sum of reconstructed muon transverse momenta as measured by the MS: $\vec{\not{E}}_T^{\,\mu} = -\sum_i \vec{p}_T^{\,\mu,i}$. Note that, as discussed above, p_T measurements for isolated muons include a correction for calorimeter energy loss. Isolated muons, then, do not make a contribution to $\vec{\not{E}}_T^{\,\mu,calo}$ in equation 4.7.

Performance of the missing transverse momentum reconstruction has been assessed by comparing MC predictions to data [113]. Results from this study are reproduced in figure 4.3; excellent agreement was obtained. In the present analysis a baseline cut $\not{E}_T > 50$ GeV is used to avoid known issues with soft $\not{E}_T$ reconstruction [113]. It will be shown in the next chapter that raising this baseline cut increases sensitivity to SUSY and MUED.

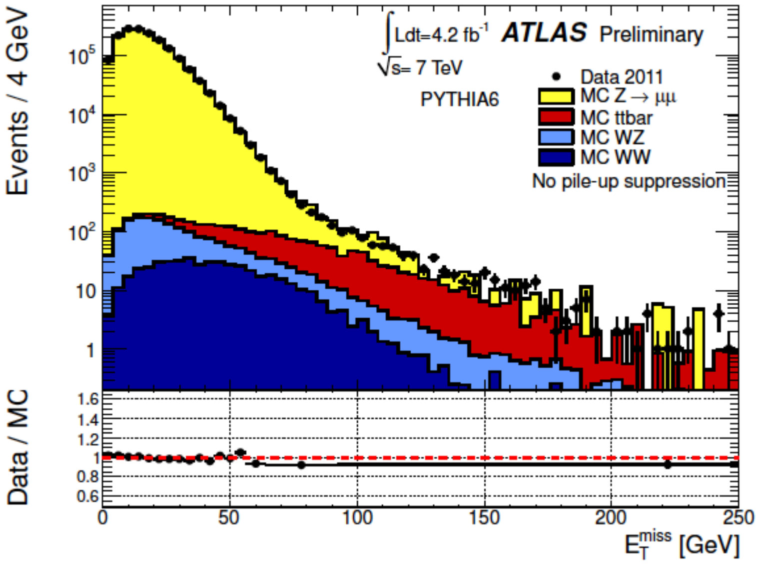

Figure 4.3: Comparison of data and MC simulated missing transverse momentum distributions in $Z \rightarrow \mu\mu$ decays. The various MC contributions have been weighted by their cross sections and the total number of events was then normalized to data.

Chapter 5

Monte Carlo Simulated Samples

Monte Carlo simulated samples have been used extensively for SR optimization and sensitivity estimates. Signal and BG events have been simulated with a number of different MC generators; this will be elucidated in the following sections. Realistic simulated datasets must include modeling of MC-generated particles incident upon ATLAS. In all cases this has been performed with the GEANT4 detector simulation software [114]. Note that the same reconstruction algorithms which were described in chapter 4 are used for data and MC. The samples described in this section have also been used to estimate the SM BG and statistically interpret the analysis; these considerations will be explored in later chapters.

5.1 Background

It is of critical importance to understand and model all SM processes which can lead to the desired $3\ell + \not{E}_T$ final state. Note that this includes processes which may include mis-identified leptons which are considered "fake" in this analysis (see chapter 7). Some basic properties of the relevant BG samples are catalogued here.

Diboson modeling includes $pp \to WZ/\gamma^* \to 3\ell\nu$, $pp \to ZZ/\gamma^* \to 4\ell, 2\ell 2\nu$[1], and $pp \to WW \to 2\ell 2\nu$. All of these are modeled with SHERPA [115], and the resulting LO cross sections are scaled to NLO with MCFM [116]–based K-factors $K = \sigma^{NLO}_{MCFM}/\sigma^{LO}_{SHERPA}$. For WZ, *e.g.*, the result is $K \sim 10.24$ pb/9.75 pb ~ 1.05.

Top–anti-top pair production ($t\bar{t}$) samples have been generated with POWHEG [117] and were normalized LO→NNLO with HATHOR [118]: 210.8→238.1 pb. Parton showering was modeled with PYTHIA [58].

Triboson (WWZ, *etc.*) production was simulated with MadGraph 5 [119]. Single top simulation was performed with MC@NLO [120] and AcerMC [121]. All $t\bar{t}Vj$ and Vj samples have been generated with ALPGEN (except MadGraph $t\bar{t}WW$). Showering was performed in PYTHIA for all of these samples.

The CT10 [122] parton distribution function (PDF) set has been utilized for all SHERPA, POWHEG, and MC@NLO samples. The CTEQ6L1 set was used for MadGraph and ALPGEN samples.

5.2 Signal

SUSY

The various SIM parameters were described in section 2.3.2. Herwig++ [123] has been used to generate all SIM via $\widetilde{\ell}$ and SIM via WZ samples, and NLO cross sections were obtained from PROSPINO [76]. The CTEQ6L1 PDF set has been utilized.

---

[1] The γ^* will be dropped henceforth.

MUED

All MUED samples were generated at LO with Herwig++ and CTEQ6L1; NLO cross sections are not available.

5.3 Correction Factors for Simulated Samples

In addition to the lepton reconstruction scale factors and b-tagging scale factors described in chapter 4, two further corrections are applied to all MC samples. The first such correction accounts for the effects of pile-up interactions. Recalling figure 3.2, it can be seen that the average number of pp interactions per bunch crossing was $\langle\mu\rangle = 20.7$ in 2012 ATLAS data [91]. As previously discussed, the vast majority of these interactions are minimum bias or QCD. This implies that when a hard scattering event is triggered and stored, ATLAS will also typically detect and record products of several unrelated inelastic scattering events which happen to be taking place at this time. This effect is known as pile-up, and it includes contributions from within the hard bunch crossing ("in-time") and from temporally nearby bunch crossings ("out-of-time"). Each MC event in a given sample is reweighted with a scale factor such that the $\langle\mu\rangle$ distribution agrees with that observed in data.

The ATLAS trigger system cannot, of course, be applied to MC events. It is therefore necessary to pass MC samples through a software simulation of the trigger. Differences between the efficiencies of the trigger applied to data and its simulation applied to MC give rise to the final event-wise MC correction needed for this analysis[2]: $\epsilon^T_D/\epsilon^T_{MC}$, where the trigger efficiencies are defined as

$$\epsilon^T_{D,MC} = \left.\frac{N_{pass}}{N_{pass}+N_{fail}}\right|_{D,MC}. \tag{5.1}$$

---

[2] The values of this scale factor are obtained with a tag-and-probe technique applied to $Z \to \ell\ell$ events; they typically reflect a 1-2% difference between data and MC.

Chapter 6

Signal Region Definitions

After selecting objects as described in chapter 4, the next project is to design a set of criteria for selecting full events. Since this is a blind analysis, the selection must be rigorously specified before comparing predictions to data. In order for a selection, called a signal region (SR), to be desirable, it should be defined in such a way so as to preferentially select signal-like events. Selections with this property are said to have good "sensitivity" to new physics scenarios. A means of quantitatively comparing and subsequently optimizing the statistical significance of candidate SRs is therefore necessary. In this chapter, the optimization program and resulting signal regions will be described in detail. The expected sensitivity will also be estimated.

6.1 Baseline Event Selection

A number of standard cuts pertaining to data quality, trigger and detector performance, and other technical considerations are used in this analysis. These "baseline" cuts are described in this section. Most of the baseline cut thresholds were previously optimized for the 2 fb^{-1} ATLAS EW SUSY trilepton analysis in 2010 [1].

Table 6.1 shows the list of trigger chains used to select data events in this analysis. The chains are also used for the software trigger simulation discussed previously. A selected event must pass at least one of these chains. The p_T thresholds given in table 6.1 ensure that the leptons are in the high efficiency (80-100%) “plateau” region of the turn-on curve for that particular chain. Signal leptons in a selected event must match the triggering lepton(s) to within $\Delta R < 0.15$. The technical trigger chain names provide convenient encapsulations of the chain properties. For example, EF_mu24i_tight indicates the presence of a tight muon with $p_T > 24$ GeV at the event filter level; the “i” denotes isolation.

Table 6.1: Trigger chains used in this analysis. The explicit technical names and the offline p_T thresholds are provided.

Lepton flavor(s)	Chain name	Offline p_T cut (GeV)
Single isolated e	EF_el_EF_e24vhi_medium1	25
Single isolated μ	EF_mu24i_tight	25
Double e	EF_2e12Tvh_loose1	14,14
	EF_e24vh_medium1_e7_medium1	25,10
Double μ	EF_2mu13	14,14
	EF_mu18_tight_mu8_EFFS	18,10
Combined $e\mu$	EF_e12Tvh_medium1_mu8	14,10
	EF_mu18_tight_e7_medium1	18,10

Stable LHC beam conditions and good subsystem performance across ATLAS cannot be taken for granted. If these conditions are satisfied during a given data collection period, the events are recorded on a good runs list (GRL). Data events selected in this analysis must be part of the GRL corresponding to the 2012 dataset.

A set of quality control cuts are employed to further reduce events featuring instrumental or otherwise undesired effects. Cosmic muons are removed by discarding events with muons satisfying $|d_0| > 0.2$ mm or $|z_0| > 1$ mm. Events containing a muon with a large track curvature uncertainty ($\frac{\sigma_{q/p}}{|q/p|} \geq 0.2$) are discarded. If the PV of an event has <5 associate tracks, the event is cut away. Calorimeter quality cuts include avoiding cells which are known to be malfunctioning, disregarding events with significant LAr noise, and ignoring corrupted data. Spurious jets are known to arise from three sources: LHC beam anomalies, calorimeter noise spikes, and cosmic rays. These can be identified by their LAr pulse shapes and the energy fraction deposited in the various calorimeter systems.

Because all signal scenarios considered in this analysis produce a SFOC lepton pair in the final state, events without such a pair are ignored. A significant background due to Drell-Yan, J/ψ ($m \sim 3.1$ GeV), and Υ ($m \sim 9.5$ GeV) is present at low dilepton invariant mass. Therefore, events with any SFOC lepton pair satisfying $m_{SFOC} < 12$ GeV are removed.

The final baseline cut is the requirement of exactly 3 signal leptons. These can be electrons, muons, or both. Leptonic tau decays are automatically included by the electron and muon reconstruction algorithms. Hadronic tau decays are not included; these will be considered in a planned update of this analysis which is in preparation at the time of this writing.

6.2 Event Selection Optimization

This section presents the full optimization of the key selection criteria which are used to define the signal regions. The general strategy and figure of merit will first be described. The explicit optimization will then be presented.

6.2.1 Strategy

The goal is to design series of cuts which will mitigate SM backgrounds while retaining good sensitivity to both SIM types and MUED. For simplicity, all SM processes are estimated purely from MC for this purpose. Appendix A describes the particulars of this estimate. The full BG estimate technique is the subject of chapter 7.

Note that the mass splitting between the LSP and the next-lightest neutralino (or, equivalently, the lightest chargino) $\Delta m_{21} = m_{\widetilde{\chi}^{0,\pm}_{2,1}} - m_{\widetilde{\chi}^0_1}$ characterizes the amount of phase space available to all final state particles in both SIM scenarios. This observation, when coupled with the fact that $\widetilde{\chi}^0_2$ can decay both via on-shell Z ($m_Z \sim 91.2$ GeV) and non-resonantly via off-shell Z or $\widetilde{\ell}$, will be seen to warrant definition of several signal regions which each target complementary kinematic regimes of the SIM parameter spaces. In particular, it will be seen to be beneficial to consider signal regions both on and off the Z mass shell. Within each of these, kinematic cuts of varying tightness can be used to obtain the desired sensitivity.

MUED cascades are phenomenologically similar to SIM, with $W^{\pm}_1 Z_1$ playing a role analogous to $\widetilde{\chi}^{\pm}_1 \widetilde{\chi}^0_2$. The optimization logic is therefore similar, but there is one noteworthy difference: the MUED cascades of interest in this analysis often produce hard jets (recall figure 2.6). A specialized SR will be developed to exploit this feature.

These considerations will be made more concrete when the optimization variables are presented explicitly in the next subsection. It is first necessary, however, to describe the figure of merit which is used to compare candidate cut thresholds.

Recall that a p-value is the probability, under the null hypothesis (which in this analysis is the SM), of obtaining experimental results at least as extreme as those observed. In high energy physics, it is canonical to instead report the number of standard deviations at which evaluation of the complementary standard normal cumulative distribution function (CDF) would give p (or $p/2$ for a two-tailed hypothesis test). This is often called the statistical significance:

$$Z_N = \sqrt{2}\mathrm{erf}^{-1}(1 - 2p), \tag{6.1}$$

where erf(x) is the error function. Note that this formula must be modified slightly for a two-tailed test, but in this analysis a one-tailed test is used. Exclusion at the 95% confidence level (CL), *i.e.* $p = 0.05$, therefore corresponds to $Z_N \sim 1.64$. The full statistical machinery which will later be used to translate the results of this analysis into statistical significances is complex and computationally intensive. It is therefore desirable at this point to adopt a more pragmatic approach which can easily provide an approximate significance suitable for optimization.

A simple Bayesian technique incorporating approximate systematic uncertainties can be used for this purpose [124]. In this formulation, an average p-value is constructed by weighting conventional Poisson p-values with Bayes posteriors:

$$p_\beta = \int_0^\infty dB \; P_P(D|B) \; p_b(B|\langle B\rangle), \tag{6.2}$$

where $\langle B\rangle$ is the background prediction, P_P is a (complementary) Poisson CDF, D is the observed event count in data, and p_b is the posterior. Assuming p_b is a truncated normal distribution with standard deviation ΔB and a lower bound at $B = 0$, the approximate p-value becomes

$$p_\beta = \frac{\displaystyle\int_0^\infty dB \; \left[1 - \frac{\Gamma(\lfloor D+1\rfloor, B)}{\lfloor D\rfloor!}\right] \; \exp\left[-\frac{(B-\langle B\rangle)^2}{2\Delta B^2}\right]}{\sqrt{2\pi}\Delta B \left[1 - \Phi\left(\frac{-\langle B\rangle}{\Delta B}\right)\right]}, \tag{6.3}$$

where Γ is the incomplete gamma function, and Φ is the standard normal CDF. In the following subsection, Z_N will be approximated by using p_β in equation 6.1. $\langle B\rangle$ will be estimated from MC and $\Delta B = 0.3 \times \langle B\rangle$. It will be seen later that 30% is a reasonable uncertainty assumption for the purposes of benchmarking. To assess the sensitivity to new physics, the “data observation” will be set to the expected total MC yield of signal and background: $D = \langle S\rangle + \langle B\rangle$.

Note that the baseline event selection attains approximate significances on the order $Z_N \lesssim 0.03$ for typical SIM benchmark points. This clearly illustrates the necessity of further optimization.

6.2.2 Threshold Determination

Each analysis variable will be introduced in this section. Optimal cuts on each variable were obtained by locally maximizing the approximate Z_N. An example of this procedure is shown in figure 6.1. Background and signal distributions will be shown for each variable.

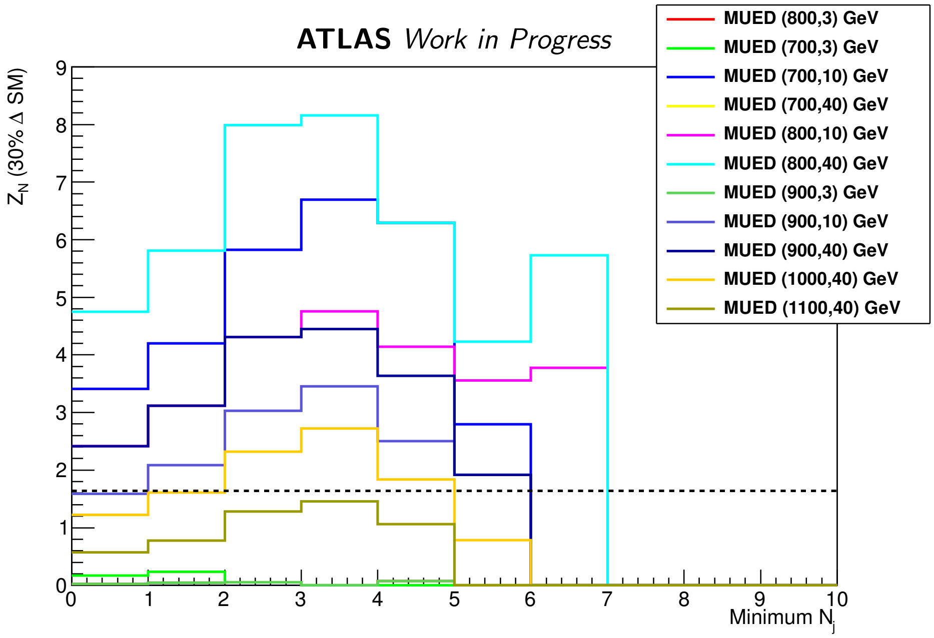

Figure 6.1: The approximate significance as a function of the lower jet multiplicity N_j threshold is shown for several MUED model points. It is seen that requiring $N_j \geq 3$ maximizes the significance.

Multiplicity of b-Jets

The contribution from $t\bar{t}$ can be greatly reduced by vetoing events with at least one b-jet. The multiplicity of b-jets after the baseline selection is displayed in figure 6.2

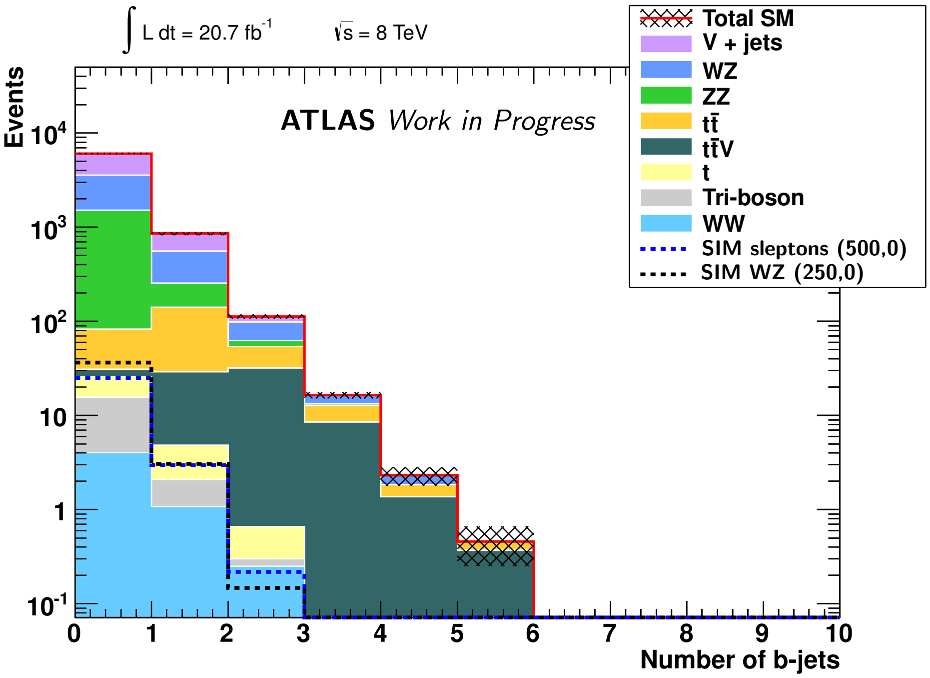

Figure 6.2: The *b*-jet multiplicity distribution is shown for the BG and representative signal points. All backgrounds are stacked and the uncertainties indicated are statistical only. The plots include all events passing the baseline selection.

Z Mass Window

The post-*b*-veto distribution of SFOC dilepton invariant mass is shown in figure 6.3. In events with multiple SFOC pairs, the SFOC mass nearest to $m_Z = 91.2$ GeV is chosen. Note that the via WZ signal exhibits a resonant peak around the Z mass, whereas the via $\widetilde{\ell}$ distribution does not. This suggests that the SRs should be broadly classified by whether they reject (SRnoZ-type) or request (SRZ-type) a Z boson. Good performance is obtained with a window $m_Z \pm 10$ GeV, but additional cuts will be placed on this variable below.

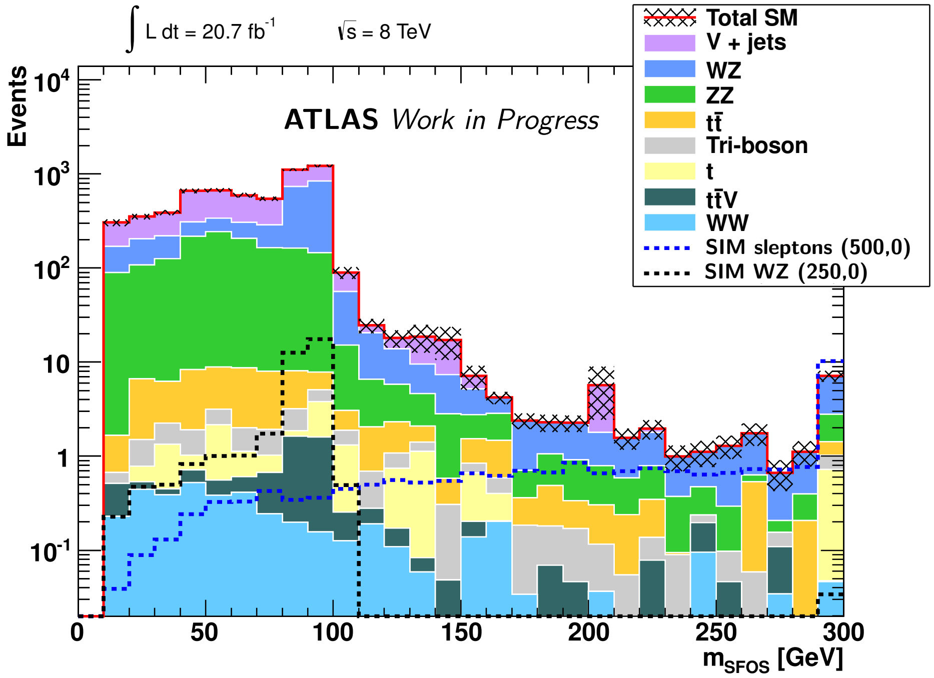

Figure 6.3: Values of m_{SFOC} nearest to m_Z are plotted after the baseline selection and b-veto.

Missing Transverse Momentum

Missing transverse momentum, as defined in section 4.5, is expected to be generated by the LSPs, LKPs, and neutrinos. $\not{E}_T$ distributions for SRnoZ-type and SRZ-type regions are shown in figure 6.4. From this figure it can be seen that several $\not{E}_T$ cuts are needed for sensitivity to various signal points in SRnoZ-type regions. Placing lower bounds at 50 GeV and 75 GeV gives the best performance. SRZ-type SRs also require multiple $\not{E}_T$ cuts. Figure 6.4 indicates that using two bins 75< $\not{E}_T$ <120 GeV and $\not{E}_T$ >120 GeV is a good choice.

SFOC Invariant Mass

To further optimize the Z rejection window in SRnoZ-type regions, the m_{SFOC} distributions after the b-veto, 10 GeV Z-veto, and $\not{E}_T$ > 50 GeV or $\not{E}_T > 75$ GeV are respectively shown in figure 6.5. These distributions suggest that the region above m_Z is not sensitive for via WZ signal points, so requiring $m_{SFOC} < 81.2$ GeV will be beneficial for these. To differentiate between low and intermediate mass regimes, it is helpful to place another bin edge at $m_{SFOC} = 60$ GeV. High-m_{SFOC} sensitivity for the via $\widetilde{\ell}$ point in figure 6.5 is preserved by defining one SRnoZ-type region which retains the high m_{SFOC} tail.

Transverse Mass

Transverse mass is useful for signal discrimination in cases where an invisible final state particle is present. The definition used in this analysis is [111]:

$$m_T = \sqrt{2p_T^{\ell}\not{E}_T[1 - \cos(\phi_{\ell} - \phi_{\not{E}_T})]}, \tag{6.4}$$

where ℓ is defined to be the hardest lepton which does not enter into calculation of the best Z mass. When defined in this way, the transverse mass gives a useful way to approximately reconstruct the W mass. Because it depends on both lepton kinematics and missing transverse momentum, this variable gives good discrimination for signal points with large mass splittings. This is shown explicitly in figure 6.6, and it is seen that $m_T > 110$ GeV is an optimal cut. Signal points with smaller mass splittings tend to be slightly more sensitive at lower m_T, so an orthogonality restriction $m_T < 110$ GeV is used for these. As can be seen in figure 6.7, this same bin edge works well in SRZ-type regions.

Lepton Transverse Momentum

Cutting on the momentum of the sub-sub-leading lepton provides good sensitivity to large mass-gap scenarios. This is shown in figure 6.8 for events satisfying the baseline, b-veto, 10 GeV Z-veto, $\not{E}_T > 75$ GeV, and $m_T > 110$ GeV. A cut $p_T^3 > 30$ GeV is seen to give good sensitivity.

MUED: Jets

It was mentioned previously that the phenomenological similarity between SIM and MUED implies a similar optimization logic. The above approach therefore applies to MUED as well. The presence of hard jets in MUED cascades of interest, though, gives an additional handle for optimization studies which will be discussed in this subsection.

The m_{SFOC} distribution after applying the baseline, a b-veto, 10 GeV Z-veto, and a preliminary missing transverse momentum cut $\not\!\!E_T > 75$ GeV is shown in figure 6.9. A window 20< m_{SFOC} <81.2 GeV gives the best performance.

The jet multiplicity distribution after applying the baseline, b-veto, 20< m_{SFOC} <81.2 GeV, and a preliminary cut $\not\!\!E_T > 75$ GeV is shown in figure 6.10. It is seen that requiring $N_j \geq 3$ is optimal. This can be understood by recalling table 2.1. The leading two-jet q^*q^* production modes can be associated with additional initial state radiation (ISR) jets, and the subleading q^*g^* modes always have ≥3 jets.

A $\not\!\!E_T$ lower threshold significance scan at the baseline, b-veto, $20 < m_{SFOC} < 81.2$ GeV, and $N_j \geq 3$ stage is shown in figure 6.11. Requiring $\not\!\!E_T >$ 120 GeV yields high significance for most points.

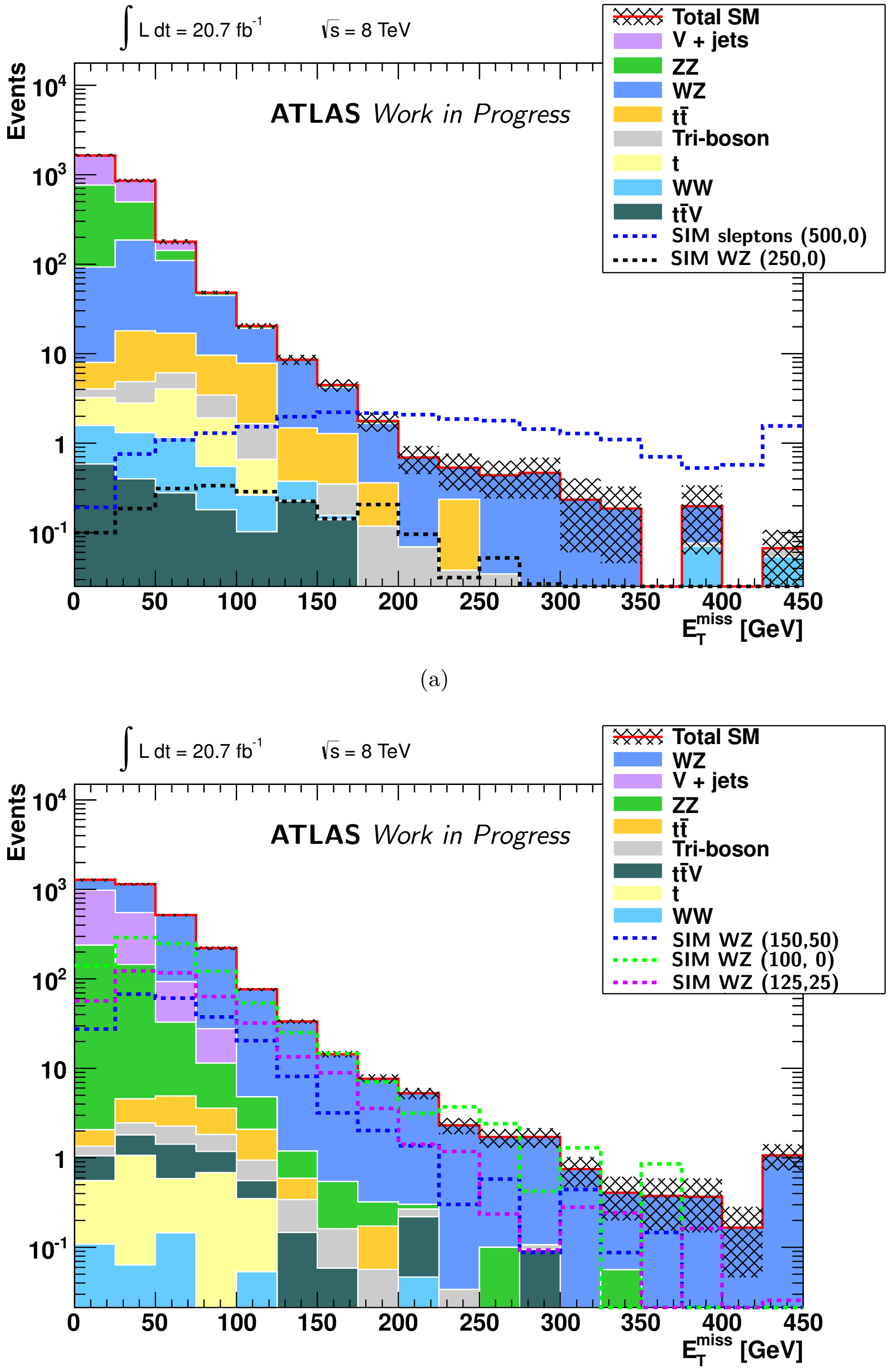

(a)

(b)

Figure 6.4: The $\not{E}_T$ distributions for events passing baseline, b-veto, and 10 GeV Z-veto (a), and baseline, b-veto, and Z-request (b).

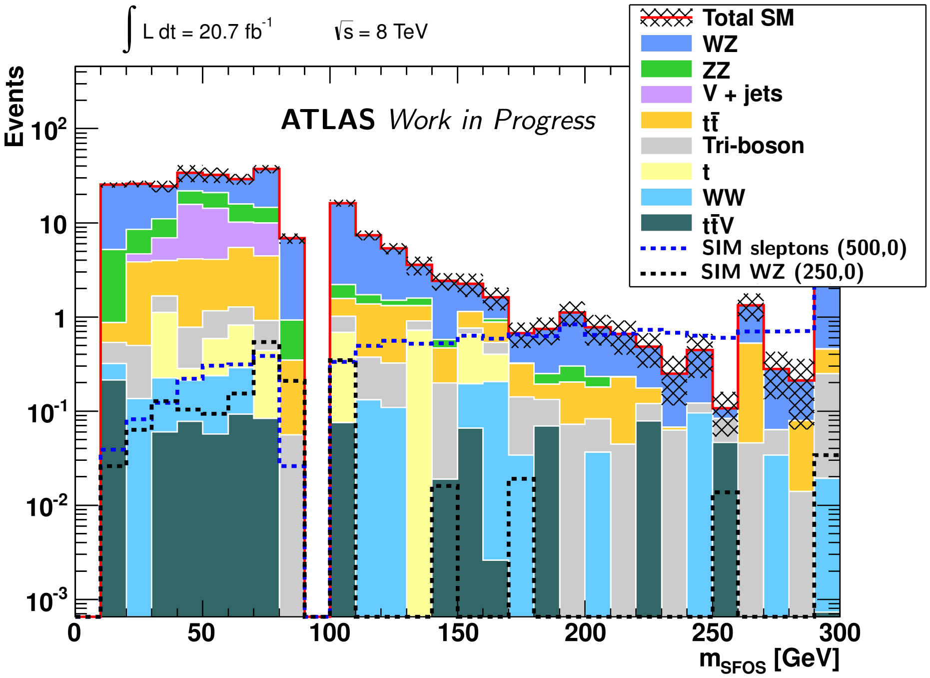

(a) SRnoZ-type: $\not{E}_T > 50$ GeV

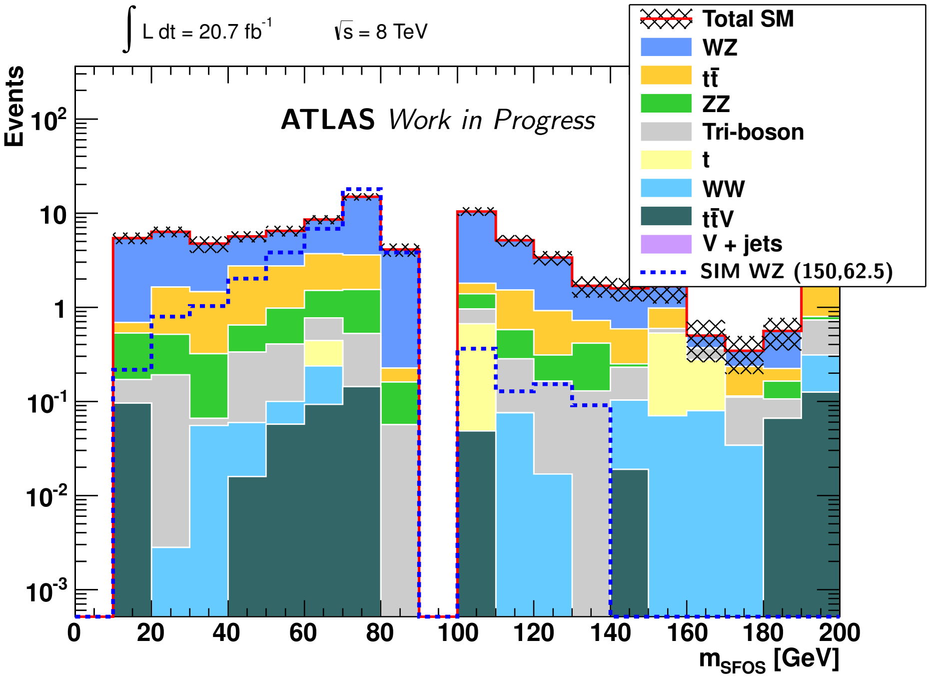

(b) SRnoZ-type: $\not{E}_T > 75$ GeV

Figure 6.5: The m_{SFOC} distribution for events passing the baseline, b-veto, 10 GeV Z-veto, and $\not{E}_T > 50$ GeV (a) or $\not{E}_T > 75$ GeV (b).

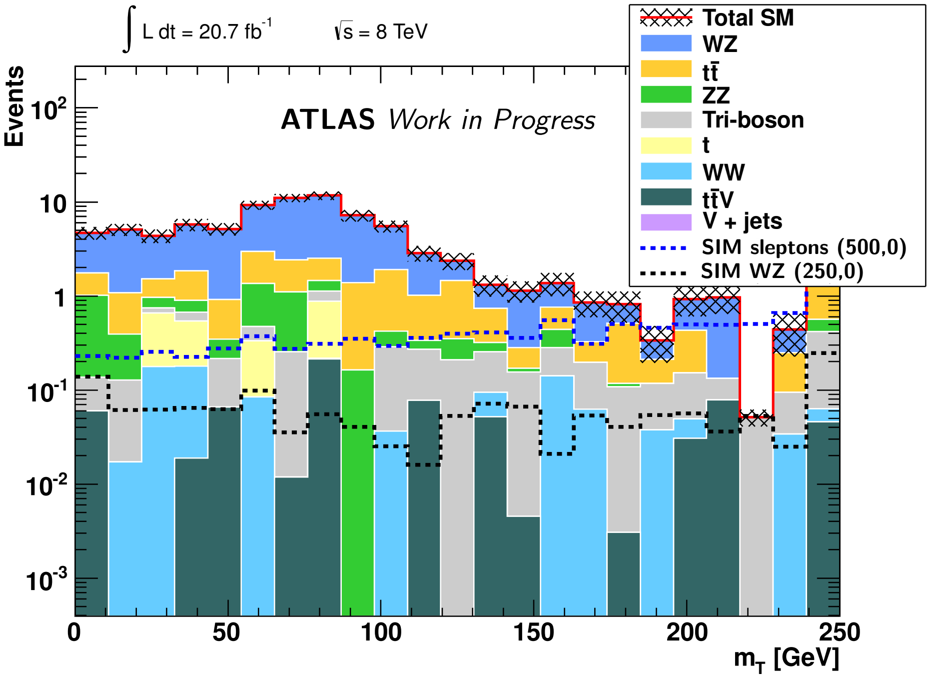

Figure 6.6: The m_T distribution for events satisfying the baseline, b-veto, 10 GeV Z-veto, and $\not{E}_T > 75$ GeV.

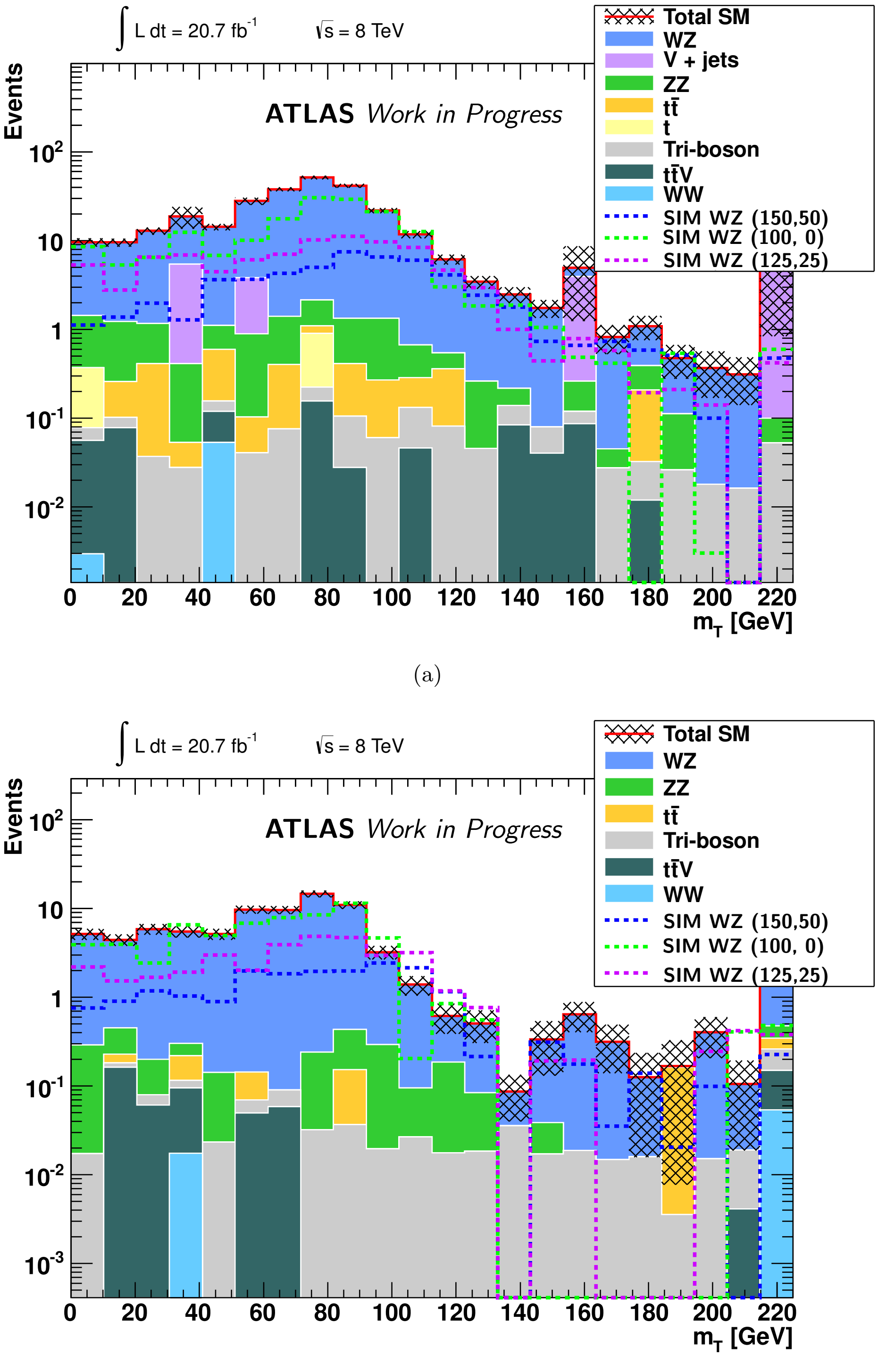

(a)

(b)

Figure 6.7: The m_T distributions the baseline, b-veto, 10 GeV Z request, and $75 < \not{E}_T < 120$ GeV (a), or $\not{E}_T > 120$ GeV (b).

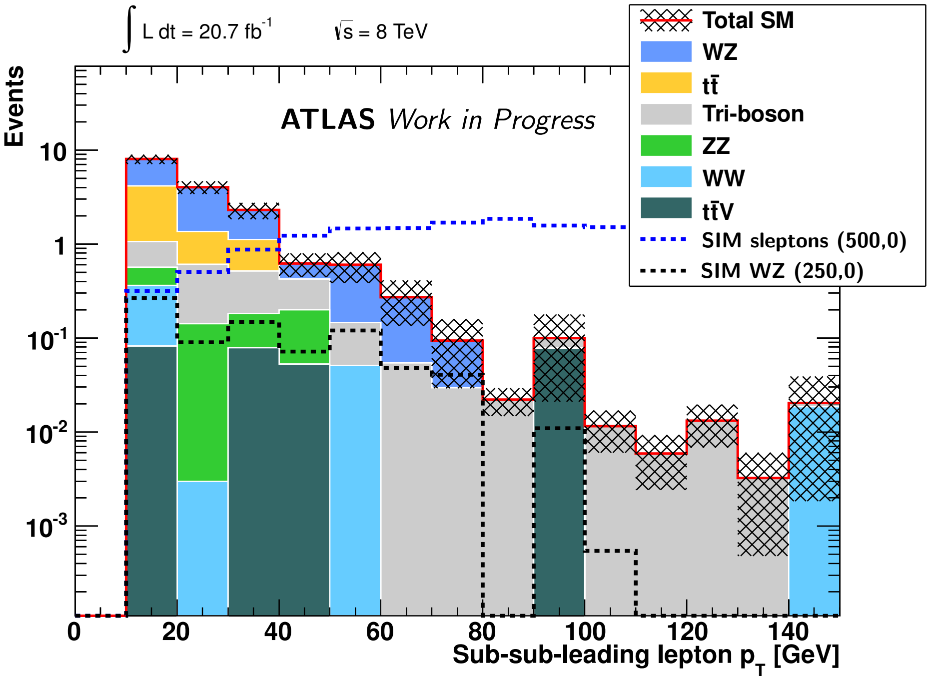

Figure 6.8: The p_T^3 distribution for events satisfying the baseline, b-veto, 10 GeV Z-veto, $\not{E}_T > 75$ GeV, and $m_T > 110$ GeV.

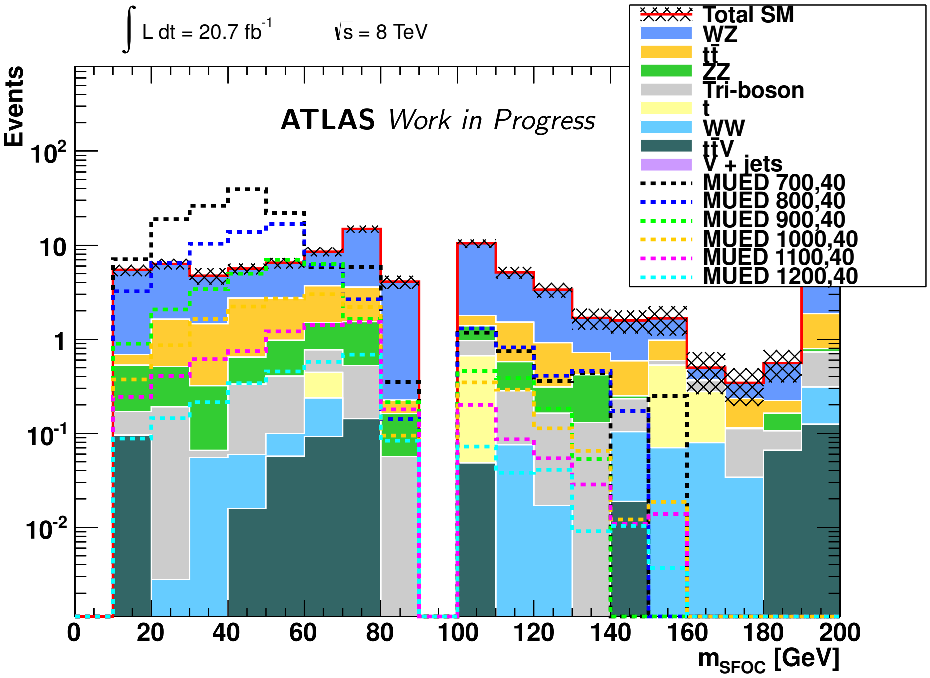

Figure 6.9: The m_{SFOC} distribution for events passing the baseline, b-veto, 10 GeV Z-veto, and $\not{E}_T > 75$ GeV.

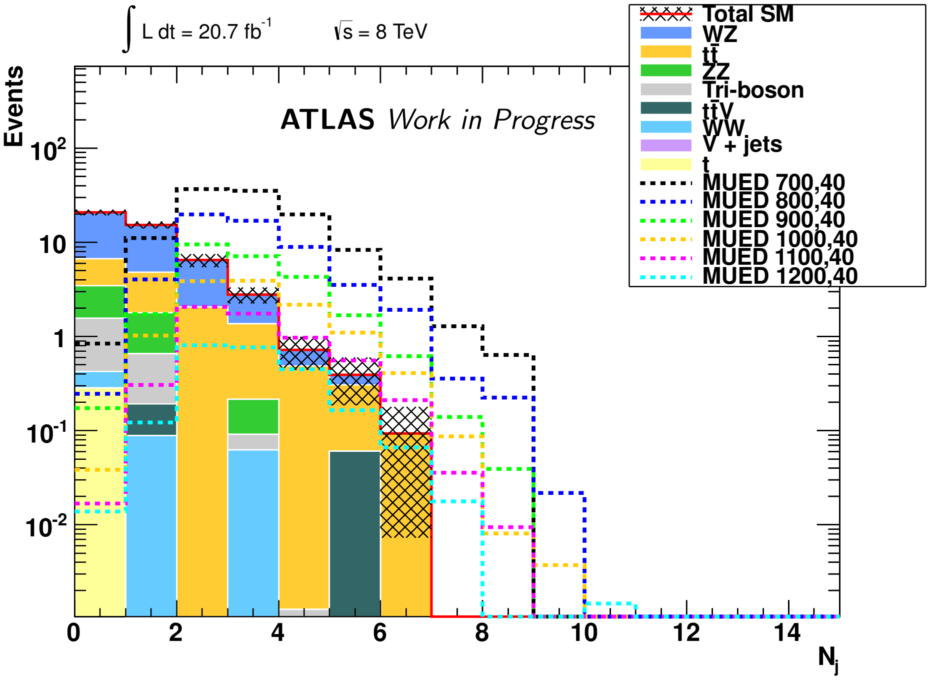

Figure 6.10: The N_j distribution for events passing the baseline, b-veto, $20 < m_{SFOC} < 81.2$ GeV, and $\not{E}_T > 75$ GeV. The significance scan corresponding to this distribution was shown in figure 6.1.

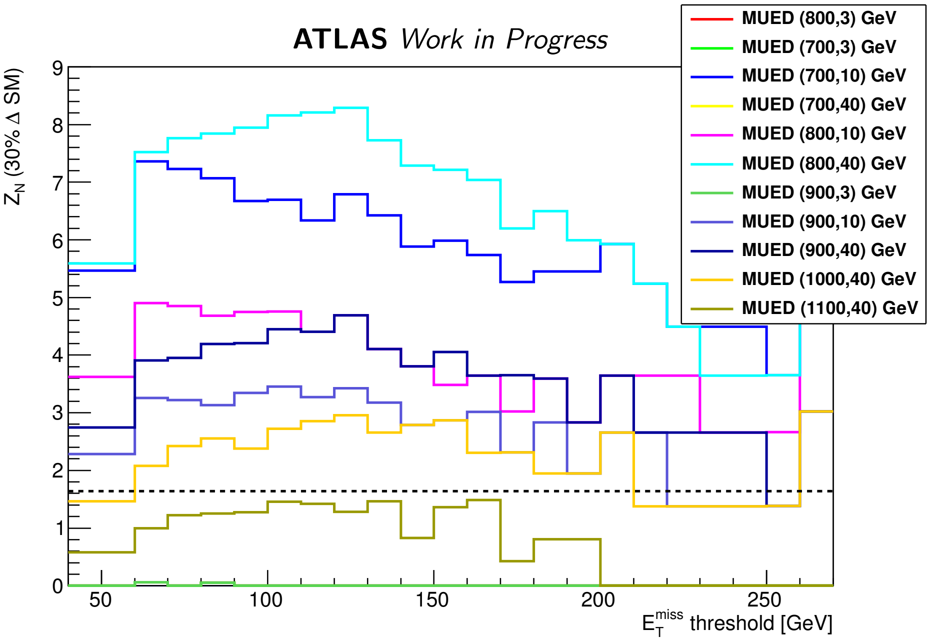

Figure 6.11: A significance scan at the baseline, b-veto, 20< m_{SFOC} <81.2 GeV, and $N_j \geq 3$ stage.

6.3 Event Selection Summary

A set of SRnoZ-type and SRZ-type SRs have now been described. These have been made orthogonal[1] to facilitate a statistical combination of the results (see chapter 8). Within each SR type, levels of tightness are conveniently labeled with Roman letters a, b, c, and d. The SRs are summarized in table 6.2.

Table 6.2: Summary of the signal region definitions. All regions require the baseline selection (notably ℓ+SFOC) and a b-veto. Note that SRnoZc events are removed from all other SRnoZ-type regions to ensure orthogonality.

SR	m_{SFOC} (GeV)	$\not{E}_T$ (GeV)	m_T (GeV)	p_T^3 (GeV)	N_j	$\perp$ veto
SRnoZa	< 60	>50	–	>10	–	!SRnoZc
SRnoZb	$(60, 81.2)$	>75	–	>10	–	!SRnoZc
SRnoZc	$\notin (81.2, 101.2)$	>75	>110	>30	–	–
SRnoZd	$(20, 81.2)$	>120	–	>10	≥ 3	!SRnoZc
SRZa	$(81.2, 101.2)$	$(75, 120)$	< 110	>10	–	–
SRZb	$(81.2, 101.2)$	$(75, 120)$	> 110	>10	–	–
SRZc	$(81.2, 101.2)$	>120	>110	>10	–	–

The set of variables used for optimization in the previous section was $\{N_b, m_{SFOC}, \not{E}_T, m_T, p_T^3, N_j\}$. This set was found to be complete in the sense that adding further variables did not improve the sensitivity.

6.4 Approximate Expected Sensitivity

This section presents the expected sensitivity estimate for all signal points in their most sensitive SRs. This will serve as a benchmark to assess the performance of the full statistical interpretation described in chapter 8.

Figure 6.12 shows that the best bulk sensitivity for SIM via $\widetilde{\ell}$ is obtained

---

[1] Two SRs are said to be "orthogonal" if their definitions prevent them from containing any of the same events.

with the tight cuts of SRnoZc. Complementary sensitivity to the compressed scenarios is added with the looser cuts of SRnoZa. Sensitivity is expected to extend as high as $m_{\tilde{\chi}^{\pm,0}_{1,2}} \sim 700$ GeV.

On the other hand, figures 6.13 and 6.14 illustrate that sensitivity to SIM via WZ is more complex, requiring both SRnoZ- and SRZ-type regions. The best bulk sensitivity, again obtained by exploiting the additional phase space, comes from SRZb and c. Low mass, compressed, and sub-diagonal ($\Delta m_{21} \sim m_Z$) sensitivity are variously obtained with SRZa, SRnoZa, and SRnoZb. These SRs are seen to give expected sensitivity up to $m_{\tilde{\chi}^{\pm,0}_{1,2}} \sim$ 300 GeV.

The most powerful region for MUED is the specialized SRnoZd. As can be seen in figure 6.15, sensitivity slightly past $R^{-1} \sim 1$ TeV is expected at high ΛR.

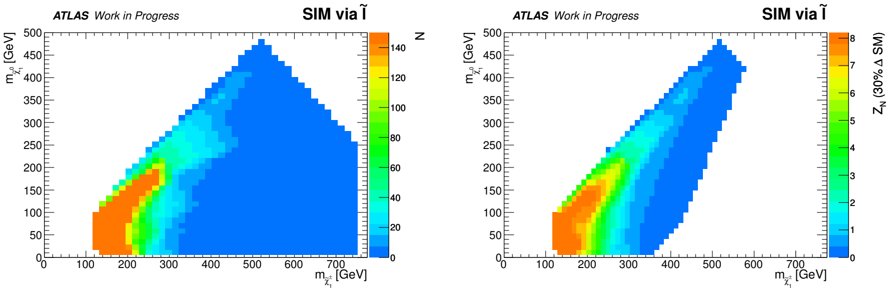

(a) SRnoZa (b) SRnoZa

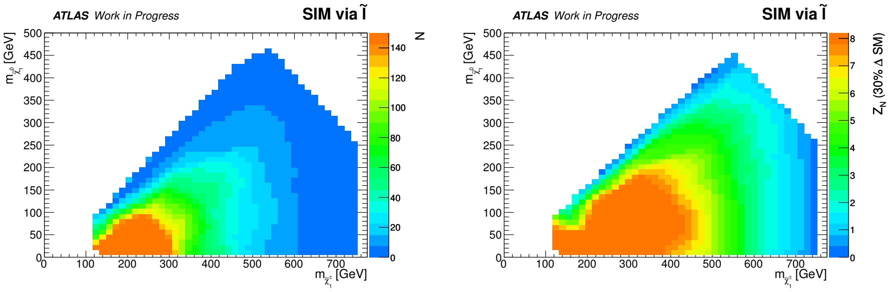

(c) SRnoZc (d) SRnoZc

Figure 6.12: Expected signal yields (left) and corresponding approximate significances (right) are shown for SIM via $\widetilde{\ell}$ in SRnoZa (top) and SRnoZc (bottom). All yields have been scaled to 20.7 fb^{-1}.

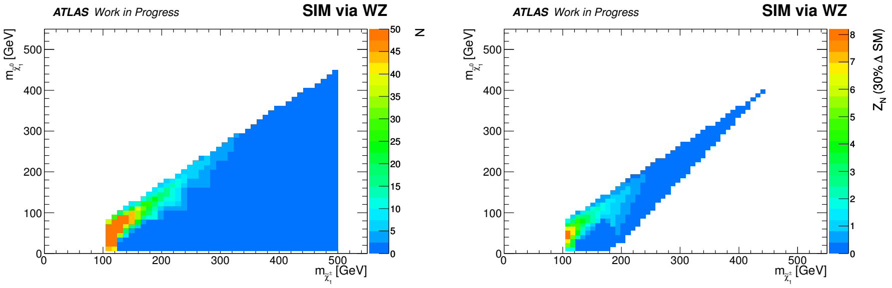

(a) SRnoZa (b) SRnoZa

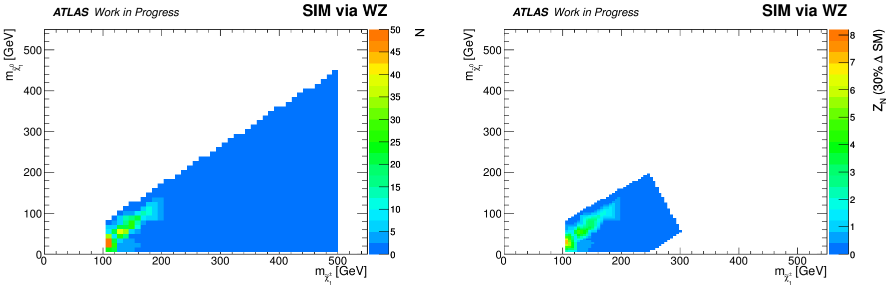

(c) SRnoZb (d) SRnoZb

Figure 6.13: Expected signal yields (left) and corresponding approximate significances (right) are shown for SIM via WZ in SRnoZa (top), and SRnoZb (bottom). All yields have been scaled to 20.7 fb^{-1}.

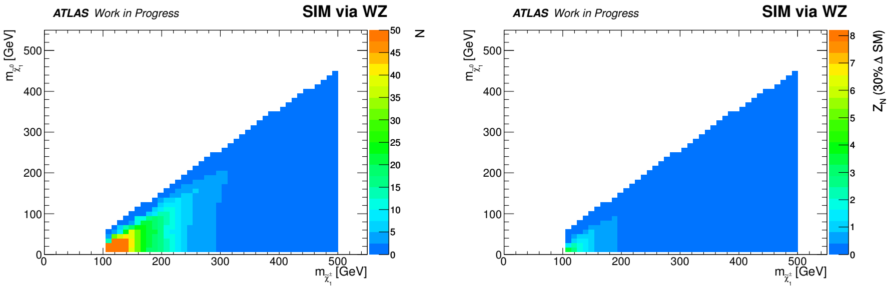

(a) SRZa

(b) SRZa

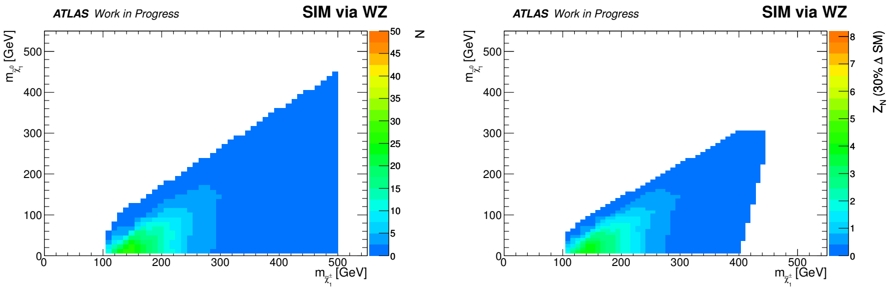

(c) SRZb

(d) SRZb

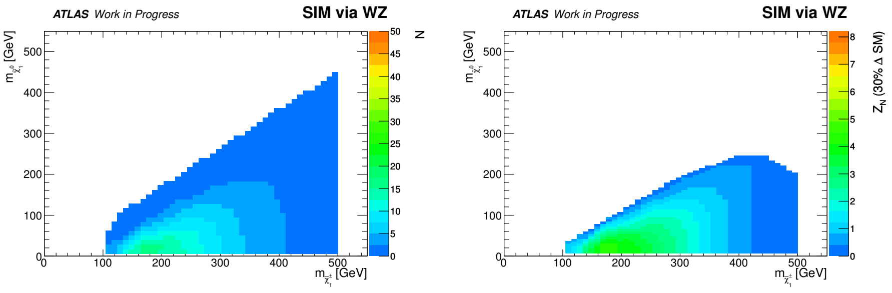

(e) SRZc

(f) SRZc

Figure 6.14: Expected signal yields (left) and corresponding approximate significances (right) are shown for SIM via WZ in SRZa (top), SRZb (middle), and SRZc (bottom). All yields have been scaled to 20.7 fb^{-1}.

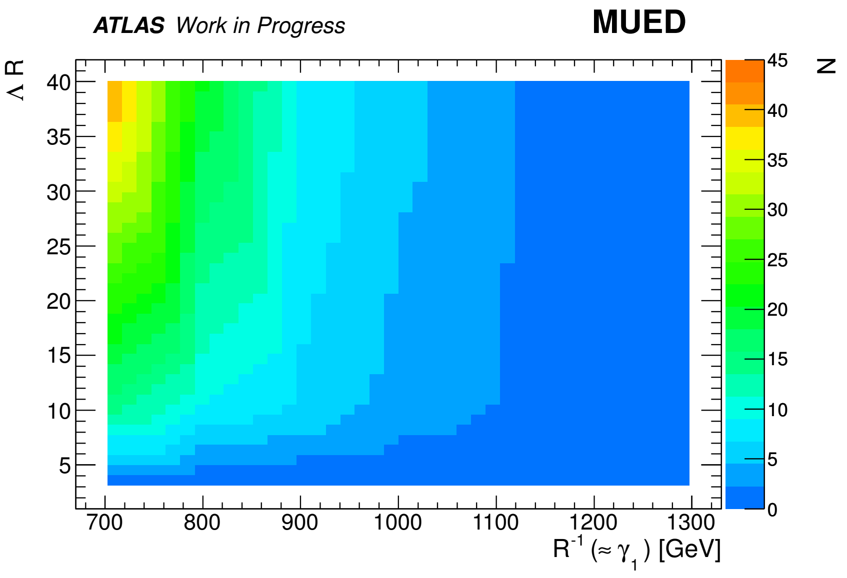

(a) SRnoZd

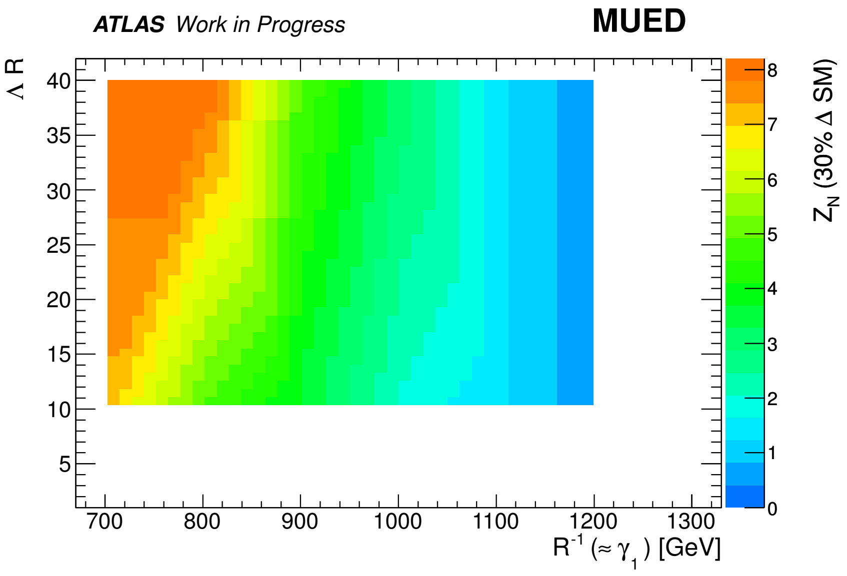

(b) SRnoZd

Figure 6.15: Expected signal yields (a) and corresponding approximate significances (b) are shown for MUED in SRnoZd. All yields have been scaled to 20.7 fb^{-1}.

Chapter 7

Standard Model Background Estimate

This chapter gives a description of the methodology used to estimate the SM background in each SR. A wide variety of uncertainties associated with this estimate are described and calculated. Comprehensive validation of the estimate is also presented.

7.1 Overview

SM backgrounds can be classified as either irreducible or reducible. Irreducible BGs are those which contribute three real final state leptons, whereas reducible BGs rely on the presence of at least one "fake" lepton to produce $3\ell + \not{E}_T$. In this analysis, a real lepton is a prompt lepton from W, Z, or τ decays, whereas fake leptons are defined to be those due to jets—heavy (HF) and light flavor (LF)[1]—or from photon conversions. The irreducible BGs are therefore WZ, ZZ, $t\bar{t}V$, and triboson. Reducible BGs are $t\bar{t}$, single t, WW, and Vj. Feynman diagrams for the two leading backgrounds, WZ and $t\bar{t}$, are shown in figure 7.1.

---

[1] The "heavy" quark flavors in this analysis are b and c. Note in particular that leptons originating from semileptonic heavy flavor decays are defined to be fake leptons in this analysis.

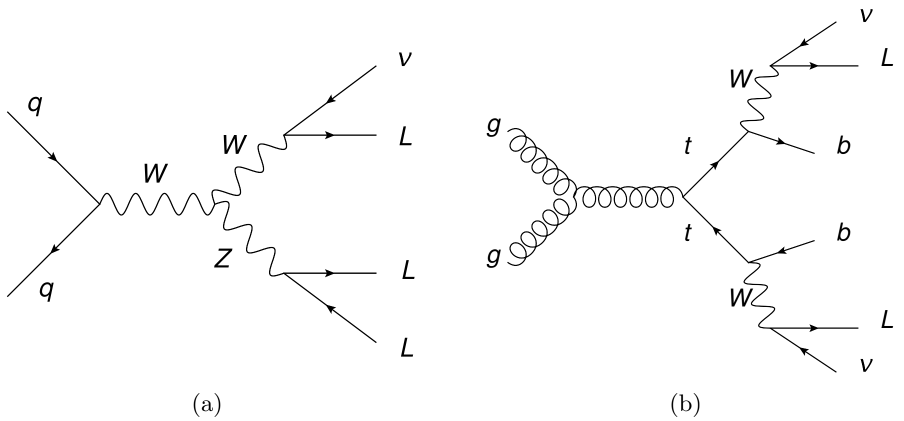

Figure 7.1: Feynman diagram examples of the two leading BGs in this analysis: s-channel WZ (a) and gluon fusion $t\bar{t}$ (b).

The purely MC-based BG estimate which was used for optimization in chapter 6 does not distinguish between irreducible and reducible contributions; this technique is also used for the SRnoZd estimate and is described in appendix A. The estimate in all other SRs utilizes a more sophisticated data-driven approach called the matrix method for the reducible BG, with irreducible contributions again estimated from MC. Both the matrix method and MC-based estimates are associated with a number of uncertainties, and all of these are profiled as properly correlated nuisance parameters. The signal regions are blinded to prevent bias. It is therefore necessary to validate the BG estimate in a set of minimally orthogonal validation regions (VRs). All of these considerations are explored in detail in the proceeding sections.

7.2 Reducible Background Estimate: The Matrix Method

The reducible background component is estimated with a data-driven matrix technique [125] which is described in this section. The method is based on the idea that, statistically speaking, real and fake leptons can be differentiated by their identification quality. A system of equations relating kinematic lepton properties and the real–fake composition can be written down:

$$\begin{pmatrix} N_{ss} \\ N_{s\bar{b}} \\ N_{\bar{b}s} \\ N_{\bar{b}\bar{b}} \end{pmatrix} = \begin{pmatrix} \epsilon_1\epsilon_2 & \epsilon_1 f_2 & f_1\epsilon_2 & f_1 f_2 \\ \epsilon_1(1-\epsilon_2) & \epsilon_1(1-f_2) & f_1(1-\epsilon_2) & f_1(1-f_2) \\ (1-\epsilon_1)\epsilon_2 & (1-\epsilon_1)f_2 & (1-f_1)\epsilon_2 & (1-f_1)f_2 \\ (1-\epsilon_1)(1-\epsilon_2) & (1-\epsilon_1)(1-f_2) & (1-f_1)(1-\epsilon_2) & (1-f_1)(1-f_2) \end{pmatrix} \begin{pmatrix} N_{RR} \\ N_{RF} \\ N_{FR} \\ N_{FF} \end{pmatrix}, \tag{7.1}$$

where the various symbols are defined as follows:

- N_{RR} is the number of events wherein the sub-leading and sub-sub-leading leptons are real. N_{RF} is the number of events wherein the sub-leading lepton is real and the sub-sub-leading lepton is fake, *etc.* Note that these yields are understood to be comprised of events with baseline leptons. Note also that only a 4-dimensional column vector (and therefore 4×4 matrix rather than the expected 8×8) is required because the leading lepton was found to be R in $\gtrsim 99\%$ of all selected events; two examples are shown in figure 7.2.

- N_{ss} is the number of events wherein the sub-leading and sub-sub-leading leptons are signal leptons[2]. $N_{s\bar{b}}$ is the number of events wherein the sub-leading lepton is signal and the sub-sub-leading lepton is baseline and not signal, *etc.*

- ϵ_i is the identification probability ("efficiency")—*i.e.* the probability that a R baseline lepton passes the signal lepton requirements. An index is included because ϵ will generally be p_T- and η-dependent, and therefore $\epsilon_{1,2}$ will assume different values according to the kinematic properties of the sub- and sub-sub-leading leptons.

- f_j is the misidentification probability ("fake rate")—*i.e.* the probability that a F baseline lepton passes the signal lepton requirements.

---

[2] Note that N_{ss} is the data observation of interest in the region to which the matrix method is being applied. If the region is a SR, N_{ss} is the observed SR yield in data and therefore must be blinded.

The vector components on the LHS of equation 7.1 are known by construction. As will be described in the following subsections, all entries of the matrix can be measured. Therefore the real–fake composition can be obtained by performing a matrix inversion. When this is done, the reducible background estimate is obtained in the following form:

$$\begin{aligned} N_{RF}+N_{FR}+N_{FF} = \frac{1}{(\epsilon_1-f_1)(\epsilon_2-f_2)} & [(\epsilon_1\epsilon_2-\epsilon_1 f_2-f_1\epsilon_2+f_1+f_2-1)N_{ss} \\ & +(\epsilon_1\epsilon_2-\epsilon_1 f_2-f_1\epsilon_2+f_2)N_{s\bar{b}}+(\epsilon_1\epsilon_2-\epsilon_1 f_2-f_1\epsilon_2+f_1)N_{\bar{b}s} \\ & +(\epsilon_1\epsilon_2-\epsilon_1 f_2-f_1\epsilon_2)N_{\bar{b}\bar{b}}]. \end{aligned} \tag{7.2}$$

It was mentioned above that $N_{RR,FR,RF,FF}$ were assumed to reflect events containing baseline leptons. This was necessary to be able to write down the system of equations in equation 7.1 in the first place. The event selection used for the analysis, however, requires all leptons to pass the signal cuts. Equation 7.2 must therefore be scaled by the efficiencies and fake rates to obtain the final reducible BG estimate:

$$N_{red} = \epsilon_1 f_2 N_{RF} + f_1\epsilon_2 N_{FR} + f_1 f_2 N_{FF}. \tag{7.3}$$

In addition to p_T- and possibly η-dependence, fake rates generally exhibit dependence on the lepton flavor ($\ell = e,\ \mu$), the fake type (LF, HF, conversion), and the type of SM process giving rise to the fake (top or gauge boson). In a region X, then, the fake rate can be written as a weighted average:

$$f_X^\ell = \sum_{i,j} sf_\ell^i R_{X,\ell}^{ij} f_\ell^{ij}, \tag{7.4}$$

where i (j) is an index encoding the fake type (BG process type), sf_ℓ^i is a scale factor which accounts for data–MC discrepancies, $R_{X,\ell}^{ij}$ is the fraction of fakes of type i which are seeded by process j, and f_ℓ^{ij} is the i-from-j fake rate. $R_{X,\ell}^{ij}$ and f_ℓ^{ij} are computed from MC simulations, while sf_ℓ^i is derived from both data and MC. MC-derived weighted average efficiencies are similarly corrected with a data-driven scale factor. Measurements of the various scale factors are presented in the following subsections.

7.2.1 Efficiencies

The efficiency computation proceeds via a standard tag-and-probe technique. An enriched sample of $Z \to \ell\ell$ is selected by enforcing the baseline *event* selection and the presence of a SFOC baseline lepton pair satisfying a 10 GeV Z-request. A "tag" lepton is identified by matching one of these baseline leptons to a single lepton trigger from table 6.1 and requiring that it passes the signal lepton selection criteria. The efficiency is then obtained by calculating the frequency with which the remaining "probe" lepton satisfies the signal criteria. If an event possesses two tags, both are counted as successful probes. The scale factor sf_{ℓ}^{ϵ} is defined to be the ratio of efficiencies obtained from data and MC; it is then applied to MC–derived cross section weighted average efficiencies in each SR.

Efficiencies have been binned in p_T, $|\eta|$, and the vertex multiplicity. No significant dependence on any of these quantities has been observed. As a representative example, figure 7.3 shows the p_T-binned muon efficiency and scale factor in data and MC. The final efficiency scale factors used in the analysis are $sf_e^{\epsilon} = 0.996 \pm 0.001$ and $sf_{\mu}^{\epsilon} = 0.995 \pm 0.001$, where the uncertainties are statistical.

7.2.2 Fake Rate Scale Factors

The fake rate measurements use the same general tag-and-probe strategy that was used for the efficiency scale factor measurements. Samples heavily enriched in LF, HF, and conversions, respectively, are selected. High quality tag leptons are then identified and used to test the baseline→signal probability for fake probes.

Figure 7.4 displays a representative selection of results. As was done for the efficiencies, the results were binned in p_T, $|\eta|$, and vertex multiplicity. As figure 7.4 suggests, no significant dependence on these quantities was observed within uncertainties. Average scale factors have therefore been used: $sf_{\ell}^{LF} = 1.0 \pm 0.1$, $sf_{e(\mu)}^{HF} = 0.75 \pm 0.05$ (0.86 ± 0.03), and $sf_{e}^{C} = 1.22 \pm 0.27$. The uncertainties are discussed in the next section.

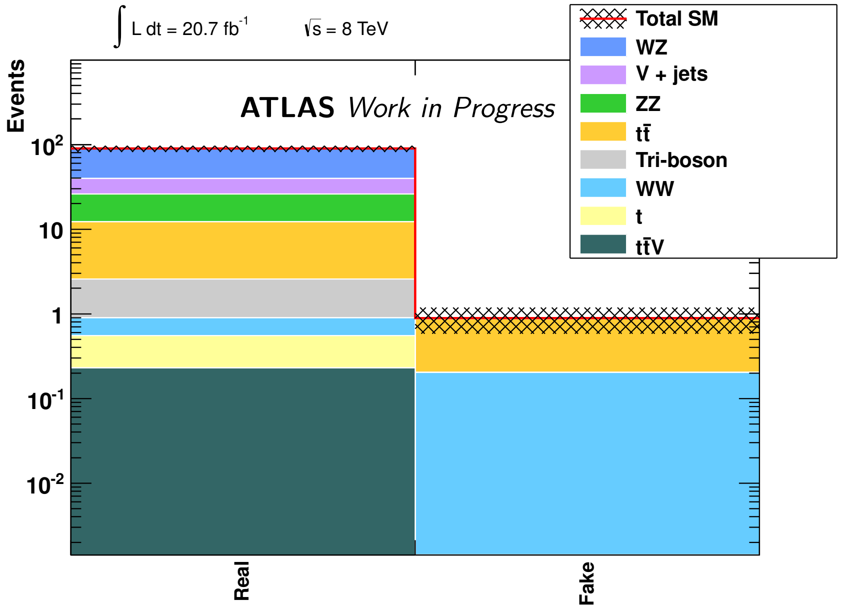

(a) SRnoZa

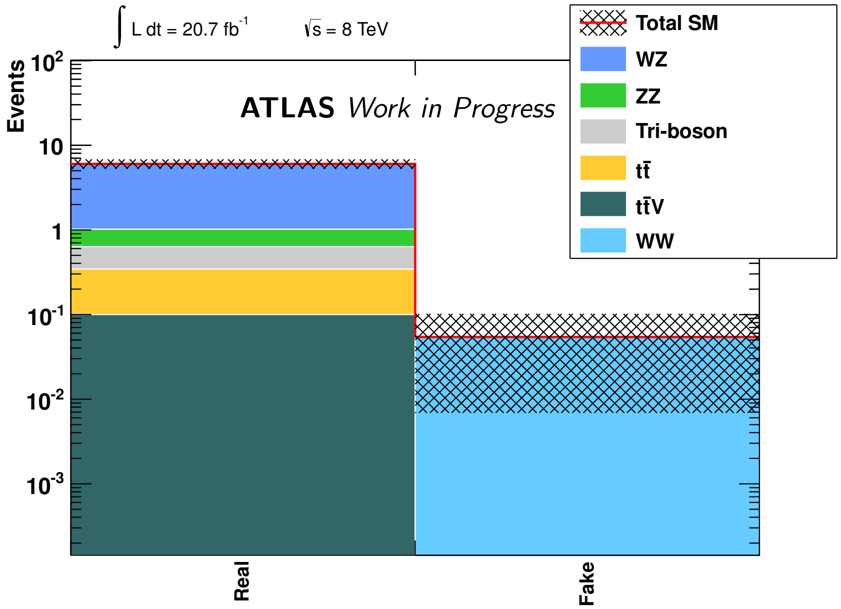

(b) SRZc

Figure 7.2: The leading lepton real–fake composition in SRnoZa (a) and SRZc (b).

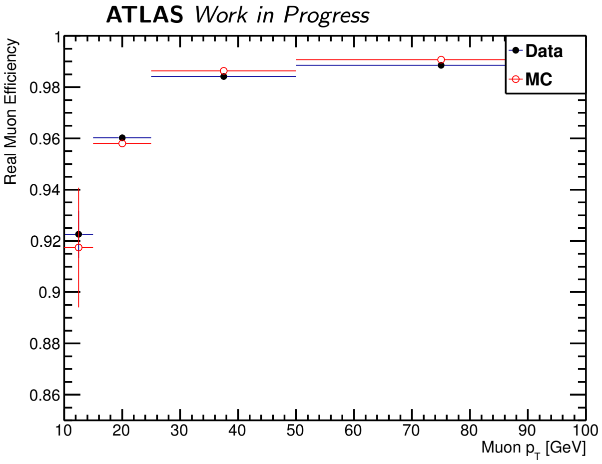

(a) Efficiency

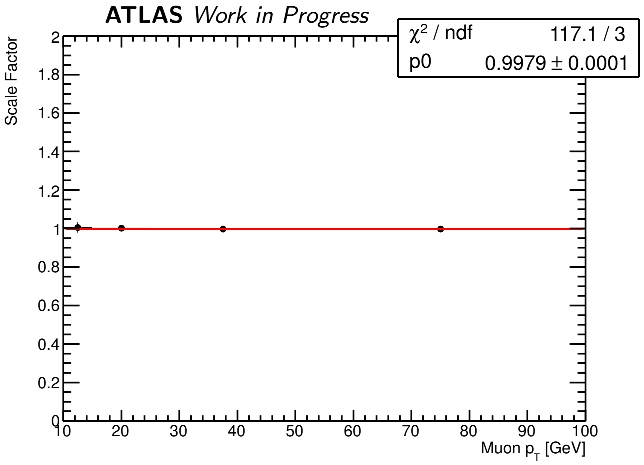

(b) Scale factor

Figure 7.3: Muon baseline→signal identification efficiency (a) and scale factor (b). Both are binned in p_T.

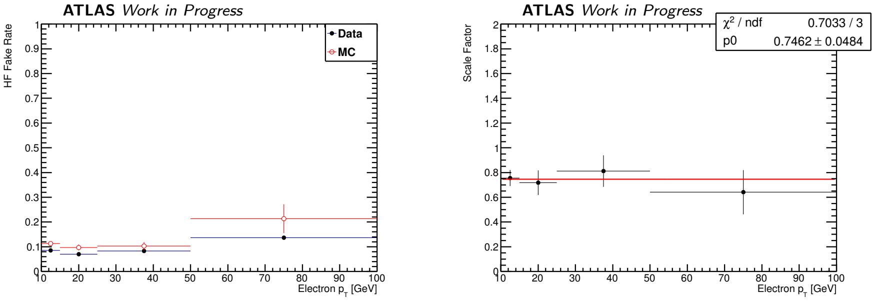

(a) Fake rate: HF

(b) Scale factor: HF

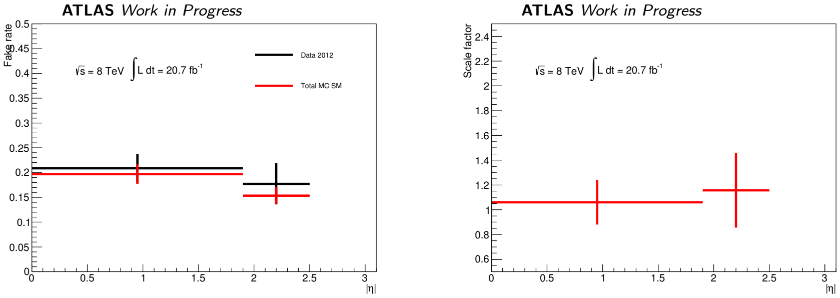

(c) Fake rate: conversions

(d) Scale factor: conversions

Figure 7.4: Fake rates (left) and scale factors (right) for electrons from HF (top) and conversions (bottom). The HF plots are binned in electron p_T, and the conversion plots are binned in electron $|\eta|$ with $p_T^e > 15$ GeV.

7.3 Sources of Uncertainty

This section contains a breakdown of all sources of uncertainty associated with the irreducible and reducible BG estimates. As will be explained in chapter 8, the statistical interpretation involves profiling all uncertainties as a set of potentially correlated Gaussian nuisance parameters. The percentages quoted in this section therefore describe the shift in the yield when a given systematic is varied by $\pm 1\sigma$ around its nominal central value.

7.3.1 Uncertainties on Irreducible Backgrounds

All uncertainties considered for the MC-based irreducible BG estimate are shown in tables 7.1 through 7.3. Note that the typical total uncertainty is roughly 30%. This tends to be dominated both by the statistical uncertainty from MC as well as several systematics—notably the generator choice and cross section. Descriptions of all irreducible uncertainties will now be provided.

Stastical uncertainty arises from the finite size of the MC samples used for the estimate. As explained in appendix A, this uncertainty is taken to be the quadrature sum of the squares of the MC weights.

WZ cross section systematics are calculated by quadrature-adding the uncertainty on the ATLAS cross section measurement [126] and the difference between this measurement and the NLO MCFM prediction; this procedure gives an uncertainty of $9\% \oplus 8\% = 12\%$. A 5% uncertainty is applied to the ZZ cross section based upon an ATLAS measurement [126]. The theoretical $t\bar{t}V$ cross section uncertainty has been estimated to be 30% by Kardos *et al.* [127]. A conservative cross section systematic of 10% is applied to reflect the absence of experimental cross section measurements for tribosons.

To quantify the effect of the choice of MC generator on the leading irreducible WZ and ZZ backgrounds, a comparison has been made between SHERPA and POWHEG. The procedure involves scaling POWHEG to

SHERPA (the latter being treated as the central value) after the pre-selection and lepton multiplicity cuts. The resulting difference in yields is then quadrature-added to the (scaled) POWHEG statistical uncertainty in each signal region to give the final generator uncertainty.

After the baseline cuts, the POWHEG WZ yield was scaled to that of SHERPA with a scale factor of 1.07. The $\not{E}_T$ distributions at the three lepton stage for each generator before and after this scaling are shown in Figure 7.5. As described above, the subsequent difference in shape between these generators gives a systematic uncertainty for each signal region as shown in Table 7.4. A similar procedure was followed for ZZ. A conservative 100% generator systematic is included for tribosons; this is a small effect because triboson yields are small in all SRs.

Systematics are associated with measurements of the energy scale and resolution for electrons and jets. The energy scale is a correction which must be measured as part of proper calibration of the calorimeter. Energy resolutions were discussed in chapter 3; their uncertainties are computed by smearing the transverse momentum of the relevant object. Similarly, the staco muon momentum scale calibration is associated with uncertainties from the ID and MS. All of these systematics are provided as a set of standard binned scale factors from the relevant ATLAS working groups. Note also that the previously described lepton reconstruction and b-tag scale factors are associated with errors. Uncertainty due to these is assessed by fluctuating the scale factors between their errors. Scale and resolution uncertainties for the missing transverse momentum cell out term (recall equation 4.7) are also included. All of these object-based systematics are typically small ($\lesssim$ 5%).

PDF sets are parameterized by a set of quantities S_j. These are commonly called eigenvectors because they can be fluctuated independently. The best-fit central values of each eigenvector are used in the analysis, and PDF uncertainties are obtained by shifting these up and down [128]. In this analysis these were found to be typically on the order of 1%.

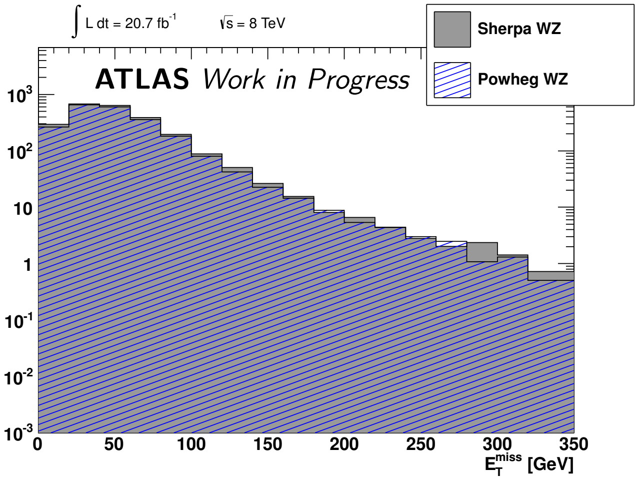

(a)

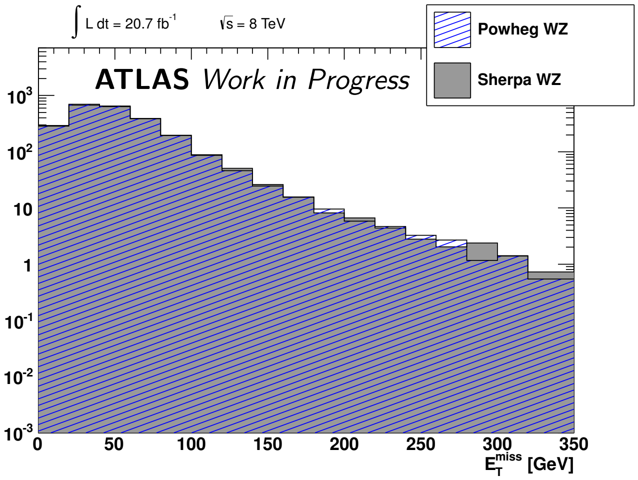

(b)

Figure 7.5: Unscaled (a) and Powheg-scaled (b) WZ $\not\!\!E_T$ distributions at the baseline stage.

An uncertainty was computed for the previously discussed trigger efficiency scale factor, but this was found to be negligible. A 3.6% systematic comes from the 2012 luminosity measurement [129].

Note that all sources of uncertainty described in this subsection are also computed for each signal sample. Additionally, uncertainties on the QCD coupling α_s, the difference between CTEQ and MSTW PDF parametrizations, and the process scales are included for the signal samples. These uncertainties range from 20-40% in total.

7.3.2 Uncertainties on Reducible Backgrounds

Uncertainties on the reducible background estimate are due to the real efficiencies, each term in equation 7.4, and the statistics of the sample selected with baseline leptons. As shown in table 7.5, the total uncertainties are of order $40 - 80\%$. Each source of uncertainty will now be described.

Dependence of the efficiencies on η introduces a small systematic in each SR. These were found to be negligible and are therefore not shown in table 7.5.

A conservative systematic is applied to account for potential uncertainty in the calculation of the fractions $R^{ij}_{X,\ell}$. This effects a fluctuation of the weighted average fake rates of size $\sim \pm 10\%$.

Statistical uncertainties are considered for the N_{ss}, *etc.* data yields and fake rates f^{ij} in each SR; these are added in quadrature and the resulting values range between $\sim 7 - 70\%$.

The fake rates f^{ij} used in the analysis are computed in each SR without applying the various $\not{E}_T$ cuts. This was found to give a large reduction in the statistical uncertainty while introducing a comparatively moderate systematic shift of $\sim 5 - 65\%$ depending on the SR.

The data and MC control region fake rates used to define the scale factors sf^i are associated with statistical uncertainties. They are also associated with uncertainties obtained by varying the cuts used to define the control regions. When both of these sources of error are added in quadrature, scale factor uncertainties $\lesssim 13\%$ are obtained.

Note that when applying the matrix method, the values on the LHS of equation 7.1 are obtained from data. A closure test, wherein these values are instead obtained from the fully MC-based estimate, can therefore be used to validate the method. Validation is achieved by comparing the resulting reducible BG estimate with fully MC-derived yields as input to the known fake composition from MC. When this was done, agreement within errors was observed in all regions, and therefore no systematic is needed to account for this potential bias.

For the fully MC-based estimate in SRnoZd, all sources of uncertainty discussed in section 7.3.1 were computed for the reducible BG components. The total reducible uncertainty in this SR is 96.5% and is dominated by MC statistics.

Table 7.1: Uncertainties on irreducible SM yields in SRnoZa, b, and c.

	Triboson	ZZ	$t\bar{t}V$	WZ	Total
			SRnoZa		
Expected Events	1.69	13.76	0.23	49.56	65.23
Electron energy scale	0.17,-0.53%	4.92,-4.27%	0.0,0.0%	1.16,-1.31%	1.92,-1.91%
Electron energy ratio	-0.16,-0.36%	-0.2,0.32%	0.0,0.0%	0.44,-0.26%	0.29,-0.14%
Muon spectrometer track p resolution	0.28,0.04%	0.02,-0.35%	0.0,0.0%	-0.22,0.03%	-0.16,-0.05%
Muon inner detector track p resolution	0.0,-0.31%	0.0,0.02%	0.0,0.0%	-0.27,0.03%	-0.2,0.02%
Jet energy scale	-0.06,1.76%	7.65,-4.39%	0.0,0.0%	2.3,1.42%	3.36,0.19%
Jet energy resolution	0.67,0.67%	7.3,7.3%	36.0,36.0%	6.73,6.73%	6.8,6.8%
$\not{E}_T$ soft term scale	-0.42,-0.46%	21.93,-15.72%	0.0,0.0%	4.27,-2.97%	7.86,-5.58%
$\not{E}_T$ soft term resolution	-0.37,-0.37%	3.39,3.39%	0.0,0.0%	0.15,0.15%	0.82,0.82%
b-tagging	2.23,-2.31%	2.94,-3.02%	61.48,-76.77%	3.11,-3.2%	3.26,-3.4%
Electron ID/reconstruction efficiency	0.39,-6.0%	1.85,-7.53%	-0.62,-7.02%	0.81,-6.83%	1.01,-6.96%
Muon ID/reconstruction efficiency	-0.1,-1.0%	-0.09,-0.99%	-0.05,-0.67%	-0.1,-1.04%	-0.1,-1.03%
MC statistics	3.94,-3.94%	6.37,-6.37%	54.76,-54.76%	4.59,-4.59%	3.74,-3.74%
Luminosity	3.6,-3.6%	3.6,-3.6%	3.6,-3.6%	3.6,-3.6%	3.6,-3.6%
Generator	100.0 %	49.4 %	0.0 %	6.9 %	18.25%
PDF	0.0,0.0%	2.6,-2.71%	0.0,0.0%	1.98,2.18%	2.06,1.08%
Cross section	10.0 %	5.0 %	30.0 %	12.0 %	10.54%
Total	100.67,-100.87%	56.27,-54.25%	94.81,-105.6%	17.62,-18.61%	24.71,-24.8%
			SRnoZb		
Expected Events	0.63	1.76	0.21	19.52	22.11
Electron energy scale	1.35,-1.11%	0.0,-3.68%	0.0,0.0%	2.99,-2.28%	2.68,-2.33%
Electron energy ratio	1.08,-0.07%	0.0,-0.48%	0.0,0.0%	0.96,-1.28%	0.88,-1.17%
Muon spectrometer track p resolution	-1.11,-0.11%	0.0,0.0%	0.0,0.0%	-0.73,0.63%	-0.67,0.55%
Muon inner detector track p resolution	0.0,-0.62%	0.0,-0.48%	0.0,0.0%	0.82,-0.06%	0.72,-0.11%
Jet energy scale	2.78,0.09%	10.61,-7.47%	0.0,46.9%	4.31,6.1%	4.73,5.23%
Jet energy resolution	1.35,1.35%	16.77,16.77%	43.16,43.16%	6.73,6.73%	7.71,7.71%
$\not{E}_T$ soft term scale	1.57,-1.05%	34.57,-23.63%	0.0,0.0%	7.22,-1.82%	9.16,-3.52%
$\not{E}_T$ soft term resolution	-0.48,-0.48%	-5.36,-5.36%	0.0,0.0%	0.82,0.82%	0.28,0.28%
b-tagging	2.25,-2.29%	2.18,-2.19%	28.75,-29.03%	3.28,-3.38%	3.4,-3.49%
Electron ID/reconstruction efficiency	0.45,-5.22%	1.01,-5.46%	-0.23,-1.84%	0.41,-4.78%	0.45,-4.82%
Muon ID/reconstruction efficiency	-0.07,-1.02%	-0.14,-0.95%	-0.4,-1.74%	-0.11,-1.08%	-0.12,-1.07%
MC statistics	6.41,-6.41%	18.29,-18.29%	54.86,-54.86%	7.54,-7.54%	6.84,-6.84%
Luminosity	3.6,-3.6%	3.6,-3.6%	3.6,-3.6%	3.6,-3.6%	3.6,-3.6%
Generator	100.0 %	38.4 %	0.0 %	7.0 %	12.09%
PDF	0.0,0.0%	2.75,-2.67%	0.0,0.0%	2.28,2.39%	2.23,1.9%
Cross section	10.0 %	5.0 %	30.0 %	12.0 %	11.55%
Total	100.87,-100.96%	58.97,-53.18%	81.31,-93.99%	20.17,-19.94%	23.04,-22.04%
			SRnoZc		
Expected Events	0.81	0.25	0.21	2.12	3.4
Electron energy scale	1.04,-2.07%	0.0,0.0%	0.0,-29.58%	7.85,-7.57%	5.15,-7.05%
Electron energy ratio	0.58,0.21%	0.0,0.0%	0.0,29.58%	0.0,6.51%	0.14,5.94%
Muon spectrometer track p resolution	0.16,-0.02%	3.11,0.0%	0.0,0.0%	0.0,0.0%	0.27,-0.0%
Muon inner detector track p resolution	0.0,0.17%	0.0,0.0%	0.0,0.0%	5.27,0.0%	3.29,0.04%
Jet energy scale	1.05,-0.02%	0.0,35.9%	0.0,69.5%	5.5,-0.42%	3.68,6.68%
Jet energy resolution	3.09,3.09%	0.0,0.0%	103.23,103.23%	11.33,11.33%	14.2,14.2%
$\not{E}_T$ soft term scale	-0.04,-2.1%	3.11,0.0%	0.0,0.0%	11.51,-2.32%	7.41,-1.95%
$\not{E}_T$ soft term resolution	0.78,0.78%	0.0,0.0%	0.0,0.0%	6.68,6.68%	4.36,4.36%
b-tagging	2.35,-2.43%	6.32,-6.32%	10.39,-10.67%	3.98,-4.12%	4.16,-4.28%
Electron ID/reconstruction efficiency	-0.0,-3.29%	1.94,0.21%	-0.18,-5.46%	0.72,-2.59%	0.58,-2.73%
Muon ID/reconstruction efficiency	-0.05,-1.04%	-0.48,-1.91%	0.2,-0.37%	-0.04,-1.07%	-0.06,-1.08%
MC statistics	5.64,-5.64%	54.82,-54.82%	51.78,-51.78%	20.6,-20.6%	13.93,-13.93%
Luminosity	3.6,-3.6%	3.6,-3.6%	3.6,-3.6%	3.6,-3.6%	3.6,-3.6%
Generator	100.0 %	14.4 %	0.0 %	65.9 %	66.2%
PDF	0.0,0.0%	9.12,-8.29%	0.0,0.0%	1.86,2.27%	1.83,0.81%
Cross section	10.0 %	5.0 %	30.0 %	12.0 %	12.12%
Total	100.81,-100.9%	58.28,-68.2%	119.83,-144.83%	73.27,-72.34%	71.3,-71.54%

Table 7.2: Uncertainties on irreducible SM yields in SRnoZd.

	Triboson	ZZ	$t\bar{t}V$	WZ	Total
SRnoZd					
Expected Events	0.01	0.07	0.06	0.35	0.48
Electron energy scale	0.0,0.0%	83.31,0.0%	0.0,0.0%	0.0,0.0%	11.42,0.0%
Electron energy ratio	0.0,0.0%	0.0,0.0%	0.0,0.0%	0.0,0.0%	0.0,0.0%
Muon spectrometer track p resolution	29.59,0.0%	0.0,0.0%	0.0,0.0%	35.9,0.0%	26.39,0.0%
Muon inner detector track p resolution	0.0,0.0%	0.0,0.0%	0.0,0.0%	0.0,0.0%	0.0,0.0%
Jet energy scale	0.0,36.78%	0.0,-83.31%	0.0,17.83%	0.0,15.8%	0.0,2.86%
Jet energy resolution	21.53,21.53%	0.0,0.0%	0.0,0.0%	47.17,47.17%	34.35,34.35%
$\not\!\!E_T$ soft term scale	29.59,0.0%	0.0,0.0%	0.0,0.0%	0.0,0.0%	0.56,0.0%
$\not\!\!E_T$ soft term resolution	0.0,0.0%	0.0,0.0%	0.0,0.0%	0.0,0.0%	0.0,0.0%
b-tagging	16.63,-19.04%	14.38,-15.67%	58.26,-59.5%	18.25,-20.41%	22.67,-24.6%
Electron ID/reconstruction efficiency	0.27,-3.99%	14.57,-15.69%	0.0,0.0%	-0.0,-3.8%	2.0,-4.96%
Muon ID/reconstruction efficiency	-0.31,-1.27%	-0.04,-0.23%	-0.75,-2.45%	-0.13,-1.21%	-0.2,-1.23%
MC statistics	43.64,-43.64%	84.96,-84.96%	100.0,-100.0%	44.89,-44.89%	36.52,-36.52%
Luminosity	3.6,-3.6%	3.6,-3.6%	3.6,-3.6%	3.6,-3.6%	3.6,-3.6%
Generator	100.0 %	65.1 %	0.0 %	115.0 %	93.57%
PDF	0.0,0.0%	2.41,-2.61%	0.0,0.0%	1.82,2.11%	1.63,1.14%
Cross section	10.0 %	5.0 %	30.0 %	12.0 %	13.24%
Total	120.45,-119.22%	137.33,-137.6%	119.61,-121.56%	138.73,-135.31%	113.16,-109.99%

Table 7.3: Uncertainties on irreducible SM yields in all SRZ-type regions.

	Triboson	ZZ	$t\bar{t}V$	WZ	Total
			SRZa		
Expected Events	0.54	8.88	0.43	235.05	244.9
Electron energy scale	2.68,-2.12%	0.52,-2.99%	0.0,0.0%	0.39,-0.19%	0.4,-0.3%
Electron energy ratio	-0.39,0.49%	1.63,0.91%	0.0,26.64%	0.06,0.04%	0.11,0.12%
Muon spectrometer track p resolution	1.17,-0.28%	0.48,0.15%	26.64,0.0%	-0.13,0.11%	-0.06,0.11%
Muon inner detector track p resolution	0.71,1.18%	0.0,0.15%	0.0,0.0%	-0.03,0.15%	-0.02,0.15%
Jet energy scale	3.3,2.64%	1.34,7.25%	26.64,21.24%	1.71,1.04%	1.74,1.3%
Jet energy resolution	2.95,2.95%	7.76,7.76%	19.64,19.64%	2.88,2.88%	3.08,3.08%
$\not\!\!E_T$ soft term scale	-1.35,0.32%	10.88,-6.69%	0.0,0.0%	2.61,-2.35%	2.9,-2.5%
$\not\!\!E_T$ soft term resolution	-0.5,-0.5%	1.95,1.95%	-0.94,-0.94%	-0.24,-0.24%	-0.16,-0.16%
b-tagging	2.56,-2.63%	3.33,-3.43%	46.28,-56.32%	3.07,-3.17%	3.15,-3.28%
Electron ID/reconstruction efficiency	0.36,-4.72%	0.37,-3.61%	0.07,-6.06%	0.41,-4.98%	0.41,-4.93%
Muon ID/reconstruction efficiency	-0.1,-1.05%	-0.08,-1.14%	0.05,-0.82%	-0.1,-1.05%	-0.1,-1.05%
MC statistics	5.92,-5.92%	8.51,-8.51%	40.41,-40.41%	2.13,-2.13%	2.07,-2.07%
Luminosity	3.6,-3.6%	3.6,-3.6%	3.6,-3.6%	3.6,-3.6%	3.6,-3.6%
Generator	100.0 %	10.7 %	0.0 %	1.6 %	2.14%
PDF	0.0,0.0%	1.85,-2.01%	0.0,0.0%	1.74,2.0%	1.74,1.85%
Cross section	10.0 %	5.0 %	30.0 %	12.0 %	11.77%
Total	100.92,-101.0%	20.66,-20.64%	80.59,-85.46%	13.96,-14.8%	13.96,-14.75%
			SRZb		
Expected Events	0.43	0.95	0.22	18.68	20.29
Electron energy scale	2.06,-2.58%	21.65,-20.82%	0.0,0.0%	2.08,-7.7%	2.97,-8.12%
Electron energy ratio	-0.65,0.29%	0.0,-6.89%	0.0,0.0%	0.3,-0.31%	0.26,-0.6%
Muon spectrometer track p resolution	-0.36,-0.21%	5.51,0.0%	0.0,0.0%	0.1,-0.12%	0.34,-0.12%
Muon inner detector track p resolution	0.2,-0.36%	0.0,0.0%	0.0,0.0%	-1.81,-0.15%	-1.66,-0.14%
Jet energy scale	-0.06,3.66%	17.68,-10.14%	0.0,18.39%	1.7,7.57%	2.39,6.77%
Jet energy resolution	0.34,0.34%	15.47,15.47%	4.64,4.64%	4.84,4.84%	5.24,5.24%
$\not\!\!E_T$ soft term scale	1.55,-2.07%	6.16,4.82%	0.0,0.0%	13.73,-16.89%	12.97,-15.37%
$\not\!\!E_T$ soft term resolution	0.72,0.72%	2.67,2.67%	0.0,0.0%	3.02,3.02%	2.93,2.93%
b-tagging	2.95,-3.0%	1.86,-1.9%	38.4,-64.33%	3.3,-3.45%	3.61,-4.03%
Electron ID/reconstruction efficiency	0.03,-4.37%	2.73,-3.99%	0.17,-1.53%	0.65,-3.14%	0.73,-3.19%
Muon ID/reconstruction efficiency	-0.08,-1.01%	-0.05,-0.91%	-0.04,-1.38%	-0.08,-1.13%	-0.08,-1.12%
MC statistics	6.62,-6.62%	25.45,-25.45%	57.33,-57.33%	7.46,-7.46%	7.0,-7.0%
Luminosity	3.6,-3.6%	3.6,-3.6%	3.6,-3.6%	3.6,-3.6%	3.6,-3.6%
Generator	100.0 %	16.8 %	0.0 %	5.9 %	8.36%
PDF	0.0,0.0%	2.33,-2.82%	0.0,0.0%	2.0,2.15%	1.95,1.84%
Cross section	10.0 %	5.0 %	30.0 %	12.0 %	11.83%
Total	100.86,-101.05%	45.61,-43.01%	75.47,-93.29%	22.24,-26.64%	22.6,-26.21%
			SRZc		
Expected Events	0.29	0.39	0.1	5.01	5.79
Electron energy scale	0.58,-1.0%	0.0,0.0%	0.0,0.0%	8.44,-10.02%	7.33,-8.73%
Electron energy ratio	-0.02,0.49%	0.0,0.0%	0.0,0.0%	0.0,0.61%	-0.0,0.55%
Muon spectrometer track p resolution	0.44,0.28%	0.0,0.0%	0.0,0.0%	-0.29,0.0%	-0.22,0.01%
Muon inner detector track p resolution	-0.05,0.0%	0.0,0.0%	0.0,0.0%	0.0,0.0%	-0.0,0.0%
Jet energy scale	0.05,2.43%	-7.58,1.46%	0.0,0.0%	8.23,0.99%	6.62,1.08%
Jet energy resolution	2.85,2.85%	4.52,4.52%	38.25,38.25%	2.77,2.77%	3.51,3.51%
$\not\!\!E_T$ soft term scale	-0.84,1.11%	0.0,-32.99%	0.0,0.0%	3.94,-4.74%	3.37,-6.26%
$\not\!\!E_T$ soft term resolution	-1.22,-1.22%	-33.02,-33.02%	0.0,0.0%	-3.3,-3.3%	-5.13,-5.13%
b-tagging	3.34,-3.4%	2.35,-2.35%	7.74,-8.19%	6.02,-6.47%	5.67,-6.07%
Electron ID/reconstruction efficiency	0.14,-4.19%	1.04,-1.32%	0.29,-2.03%	0.96,-3.24%	0.91,-3.14%
Muon ID/reconstruction efficiency	-0.04,-1.07%	-0.29,-1.39%	0.03,-1.08%	0.02,-0.95%	-0.01,-0.99%
MC statistics	6.37,-6.37%	41.46,-41.46%	95.95,-95.95%	14.22,-14.22%	12.73,-12.73%
Luminosity	3.6,-3.6%	3.6,-3.6%	3.6,-3.6%	3.6,-3.6%	3.6,-3.6%
Generator	100.0 %	35.4 %	0.0 %	12.9 %	18.55%
PDF	0.0,0.0%	3.43,-4.47%	0.0,0.0%	1.37,1.67%	1.41,1.15%
Cross section	10.0 %	5.0 %	30.0 %	12.0 %	11.74%
Total	100.87,-101.0%	64.78,-72.39%	107.9,-107.95%	27.16,-26.92%	28.98,-29.35%

Table 7.4: WZ generator systematics have been computed in each signal region as shown here. All yields are scaled to 20.7 fb^{-1} and all uncertainties are statistical. The POWHEG yields have been scaled to SHERPA at the three lepton stage with a scale factor of 1.07.

Region	SHERPA WZ	POWHEG WZ (scaled)	Generator systematic
SRnoZa	49.6±2.3	46.5±1.4	6.86%
SRnoZb	19.5±1.5	20.4±1.0	6.96%
SRnoZc	2.12±0.44	3.46±0.41	65.9%
SRnoZd	0.35±0.16	0.72±0.15	115%
SRZa	235.0±5.1	236.1±3.6	1.60%
SRZb	18.7±1.4	19.2±1.0	5.86%
SRZc	5.01±0.7	5.37±0.53	12.9%

Table 7.5: Uncertainties on the reducible BG estimate in all relevant SRs.

	SRnoZa	SRnoZb	SRnoZc	SRZa	SRZb	SRZc
Expected Events	31.0	7.08	1.03	4.28	1.70	0.46
Statistics	+7.3,-7.3%	+12,-12%	+38,-38%	+34,-34%	+35,-35%	+71,-71%
Fractions	+12,-12%	+19,-19%	+5,-14%	+29,-29%	+8,-9%	+20,-26%
$\not{E}_T$ dependence	+42,-36%	+64,-64%	+10,-9%	+33,-26%	+6,-5%	+16,-13%
Scale factors	+7,-6%	+13,-13%	+1,-1%	+4,-4%	+0,-0%	+1,-1%
Total	+45,-39%	+66,-50%	+40,-42%	+84,-111%	+37,-38%	+76,-78%

7.4 Background Estimate Validation

Before unblinding the analysis, it is necessary to validate the background estimate technique. This is achieved by defining a number of VRs which are similar but orthogonal to the SRs. The definitions of these regions are given in table 7.6 below; it is seen that orthogonalization is achieved by lowering the $\not{E}_T$ cut or requiring the presence of at least one b-jet. Because the VRs are not blinded, they permit realistic performance benchmarking of the BG estimate.

Each region targets particular BG components. VRnoZa(b) targets WZ^*, Z^*Z^*, $Z^* + j$ ($t\bar{t}$) by cutting $35 < \not{E}_T < 50$ GeV (requiring ≥ 1 b-jet). Similarly, VRZa(b) targets WZ, $Z + j$ (WZ).

Table 7.6: Validation region definitions.

	N_ℓ	SFOC pair	Z boson	$\not{E}_T$ (GeV)	N_b	Target process
VRnoZa	3	request	veto	35–50	0	WZ^*, Z^*Z^*, $Z^* + j$
VRnoZb	3	request	veto	> 50	≥ 1	$t\bar{t}$
VRZa	3	request	request	30–50	0	WZ, $Z + j$
VRZb	3	request	request	> 50	≥ 1	WZ

The comparison between SM predictions and observations in data for all VRs is displayed in table 7.7. The full background estimate (including the matrix method) is used for this estimate; the corresponding table for the MC-based estimate can be found in appendix A. Note that agreement is achieved within errors in all VRs. This fact, coupled with the agreement seen in the selection of VR distributions shown in figure 7.6, validates the methodology.

Table 7.7: Predictions and observations in all validation regions. Uncertainties are systematic and statistical.

Selection	VRnoZa	VRnoZb	VRZa	VRZb
Triboson	1.4±1.4	0.5±0.5	0.6±0.6	0.26±0.27
ZZ	128±87	4.5±2.8	108±23	6.9±2.2
$t\bar{t}V$	2.9±1.2	21±7	7.4±2.6	26±8
WZ	110±21	34±15	545±89	138±38
Σ SM irreducible	242±90	60±16	662±92	171±39
SM reducible	146±55	72±45	376±138	27±13
Σ SM	388±106	132±48	1038±166	198±41
Data	463	141	1131	171

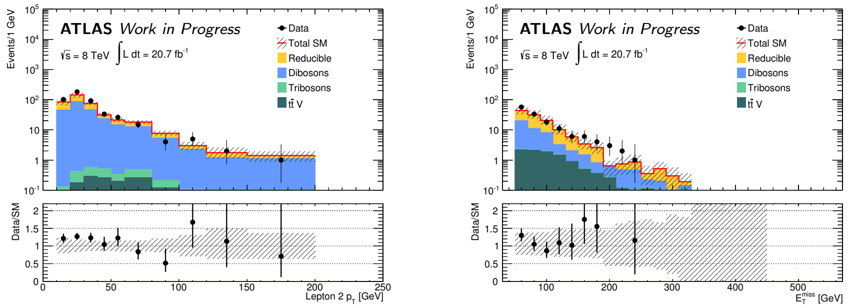

(a) VRnoZa (b) VRnoZb

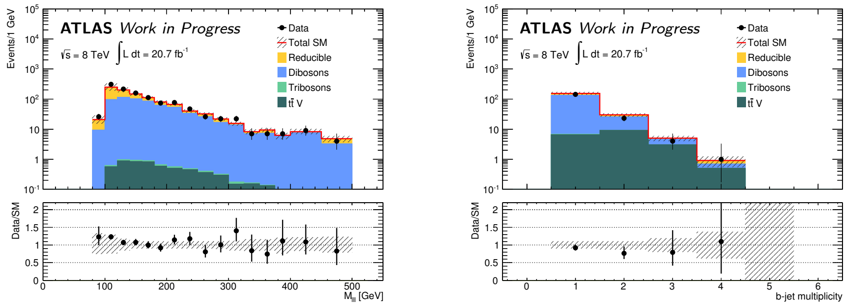

(c) VRZa (d) VRZb

Figure 7.6: Distributions of p_T^2 (a), $\not\!\!E_T$ (b), $M_{\ell\ell\ell}$ (c), and N_b (d) for data and the full BG estimate are overlaid in the indicated validation regions. Uncertainties on the BG are statistical and systematic. $\sqrt{N}$ statistical error bars are included on the data.

Chapter 8

Results and Interpretation

This chapter presents the full suite of results. A comparison between data observations and BG predictions in each SR will be shown and discussed. The interpretation of this comparison requires elucidation of a statistical method called the CL_s technique [130]. This technique is then used to set 95% CL limits on the parameter spaces of MUED and SUSY.

8.1 Signal Region Observations

Table 8.1 shows the final BG estimates and the unblinded observations in data in all SRs. The reducible SM contributions in SRnoZa, b, and c, and all SRZ-type regions (SRnoZd) have been estimated using the matrix method (MC), and the irreducible contributions have been estimated purely with MC.

Remarkable agreement between SM prediction and observation is obtained in all signal regions. To further illustrate this fact, various SR distributions are provided in figures 8.1 and 8.2. From the p-values p_0, it is clear that no significant excess[1] can be claimed from these null results; the derivation of this "discovery" p-value will be explained in due course. The next step is therefore to translate the results into constraints (in the form of 95% CL

---

[1] By convention, a 3σ (5σ) excess is considered evidence (discovery) of new phenomena in experimental high energy physics.

Table 8.1: Full BG estimate compared to data in all SRs. Errors are statistical and systematic.

Selection	SRnoZa	SRnoZb	SRnoZc	SRnoZd	SRZa	SRZb	SRZc
Triboson	1.7±1.7	0.6±0.6	0.8±0.8	0.01±0.01	0.5±0.5	0.4±0.4	0.29±0.29
ZZ	14±8	1.8±1.0	0.25±0.17	0.07±0.09	8.9±1.8	1.0±0.4	0.39±0.28
$t\bar{t}V$	0.23±0.23	0.21±0.19	0.21±0.30	0.06±0.07	0.4±0.4	0.22±0.21	0.10±0.10
WZ	50±9	20±4	2.1±1.6	0.35±0.48	235±35	19±5	5.0±1.4
Σ SM irreducible	65±12	22±4	3.4±1.8	0.48±0.50	245±35	20±5	5.8±1.4
SM reducible	31±14	7±5	1.0±0.4	0.57±0.55	4±5	1.7±0.7	0.5±0.4
Σ SM	96±19	29±6	4.4±1.8	1.06±0.74	249±35	22±5	6.3±1.5
Data	101	32	5	2	273	23	6
p_0	0.41	0.37	0.40	0.22	0.23	0.44	0.50

limits) on the SIM and MUED parameter spaces.

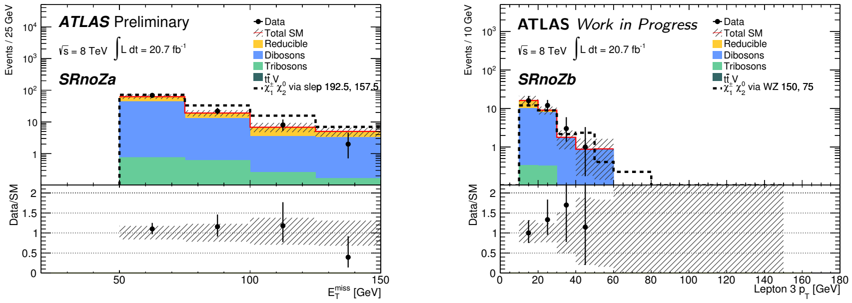

(a) SRnoZa

(b) SRnoZb

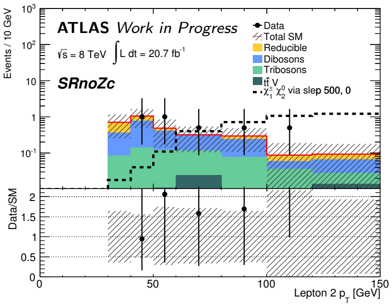

(c) SRnoZc

Figure 8.1: Distributions of $\not\!\!E_T$ (a), p_T^3 (b), and p_T^2 (c) for data and the full BG estimate are overlaid in the indicated SRnoZ-type regions. Uncertainties on the BG are statistical and systematic. $\sqrt{N}$ statistical error bars are included on the data.

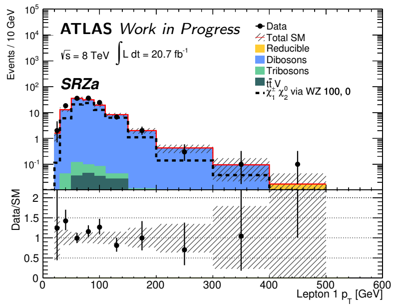

(a) SRZa (b) SRZb

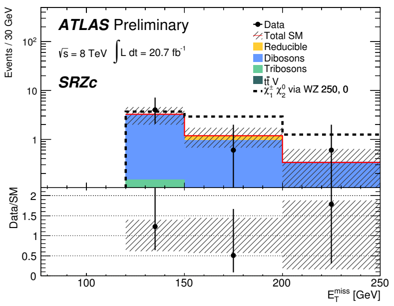

(c) SRZc

Figure 8.2: Distributions of p_T^1 (a), m_T (b), and $\not{E}_T$ (c) for data and the full BG estimate are overlaid in the indicated SRZ-type regions. Uncertainties on the BG are statistical and systematic. $\sqrt{N}$ statistical error bars are included on the data.

8.2 Methodology for Statistical Interpretation of Results

For SUSY analyses at the LHC, statistical interpretations are conventionally carried out using the modified frequentist CL_s prescription [130]. This is a frequentist upper limit setting method, but the traditional p-value is modified in a conservative way. An outline of the method will now be given.

A likelihood function is constructed which has the general form [131]

$$L(n_{\mathrm{SR}}|\mu, b, \vec{\theta}\,) = P(n_{\mathrm{SR}}|\lambda_{\mathrm{SR}}(\mu, b, \vec{\theta}\,)) \times P_s(\vec{\theta}^{\,0}, \vec{\theta}\,), \tag{8.1}$$

where n_{SR} is the number of events observed in data in a given SR, μ is the signal strength (see below), b is the BG estimate, $\vec{\theta}$ is a vector of nuisance parameters (systematics) with nominal values $\vec{\theta}^{\,0}$, P is a Poisson distribution for n_{SR} with mean λ_{SR}, and P_s is a probability density function (PDF) for the nuisance parameters. The signal strength μ is an arbitrary factor which modifies the nominal signal cross section: $\sigma_s \rightarrow \mu\sigma_s$. The BG-only case corresponds to $\mu = 0$, and $\mu = 1$ corresponds to the nominal S+BG case.

Notice that the likelihood in equation 8.1 has been written as a product of two independent probabilities: the probability to observe n_{SR} events in data and the probability that the nuisance parameters take on particular values $\vec{\theta}$. Systematic uncertainties contribute to both of these factors. On one hand, P_s serves to constrain the systematics in fits. In this analysis, this is assumed to take the form of a product of standard normal distributions [131]:

$$P_s(\vec{\theta}^{\,0}, \vec{\theta}\,) = \prod_{i}^{N_s} \phi(\theta_i - \theta_i^0), \tag{8.2}$$

where N_s is the number of nuisance parameters to be considered. On the other hand, the degree of impact of each systematic is accounted for explicitly in λ_{SR}. Without systematics, this would have the form $\lambda_{\mathrm{SR}} = \mu s + b$, where s is the expected signal yield. If, for example, nuisance parameter θ_1 is associated with an 11% BG yield shift (recall table 7.1), this must be modified[2]: $\lambda_{\mathrm{SR}} = \mu s + b + 0.11 b\theta_1$.

All correlations are introduced by describing multiple systematics with the same nuisance parameter. This allows modeling of region–wise (*e.g.* cross section uncertainties), process–wise (*e.g.* jet energy scale), and region–process–wise (*e.g.* luminosity) correlations. When all region-wise correlations are accounted for, statistical combinations of multiple signal regions can be performed by defining a new likelihood function as a product of likelihoods of the single-SR form in equation 8.1.

With the likelihood in place, a profile log-likelihood ratio test statistic can be defined:

$$\widetilde{q}_\mu \equiv \begin{cases} -2\ln\dfrac{L(\mu,\hat{\hat{\theta}}(\mu))}{L(0,\hat{\hat{\theta}}(0))}, & \hat{\mu} < 0 \\ -2\ln\dfrac{L(\mu,\hat{\hat{\theta}}(\mu))}{L(\hat{\mu},\hat{\theta})}, & 0 \leq \hat{\mu} \leq \mu \\ 0, & \hat{\mu} > \mu, \end{cases} \tag{8.3}$$

where $\hat{\mu}$ and $\hat{\theta}$ are maximum likelihood estimators (MLEs), and $\hat{\hat{\theta}}(\mu)$ is a conditional MLE for a given μ. Note that the vector arrow $\vec{}$ on θ has been suppressed for notational simplicity. Usage of this test statistic is canonical for ATLAS SUSY searches [132]. The value of $\widetilde{q}_\mu$ observed in data is then found by setting $\mu = 1$, although other values of μ may also be tested. A comment will be made on this below.

Monte Carlo pseudo-experiments ("toys") are then used to build the PDF $f(\widetilde{q}_\mu)$ in the S+BG case $f(\widetilde{q}_1|\hat{\hat{\theta}}(\mu = 1, \mathrm{obs}))$ and in the BG-only case $f(\widetilde{q}_0|\hat{\hat{\theta}}(\mu = 0, \mathrm{obs}))$. The conditional MLEs used here are the values obtained from the data observation—although the nuisance parameters float in the extremiza-

---

[2] Note in particular that this form of λ_{SR}, when considered in conjunction with equation 8.2, appropriately incorporates the desired influence of the systematics when they assume their nominal values and their $\pm 1\sigma$ shifts.

tions used to compute $\widetilde{q}_\mu$. This means that the nuisance parameters are set to their observed conditional MLE values in order to create (and then sample) $P(n_{\rm SR})$. This gives a new pseudo-data value of $n_{\rm SR}$, which is then used to compute a value of $\widetilde{q}_\mu$ in the same way as was initially done to obtain the observed value in data. This procedure is iterated and a PDF is obtained. An example is shown in figure 8.3.

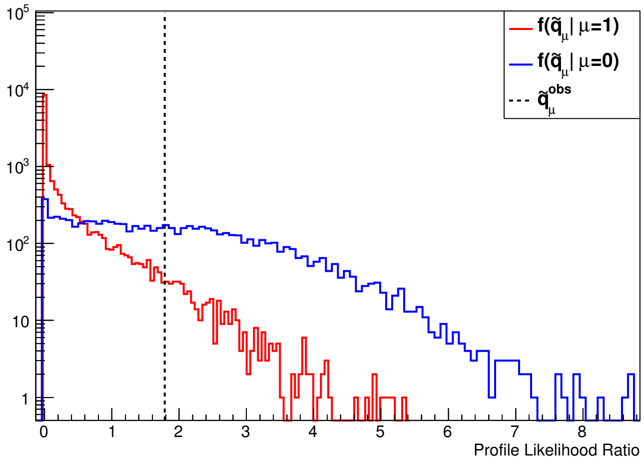

Figure 8.3: The non-normalized distribution of the profile log-likelihood ratio test statistic is shown for S+BG ($\mu = 1$) and BG-only ($\mu = 0$) hypotheses. The signal here is a SIM grid point with $CL_s \sim 5\%$. 1.5×10^4 toy experiments have been used, and a value $\widetilde{q}_1^{\,obs} = 1.79$ was seen in data.

Two p-values are then defined. One of these describes the S+BG hypothesis:

$$p_1 \equiv \int_{\widetilde{q}_1^{\rm obs}}^{\infty} d\widetilde{q}_1 \; f(\widetilde{q}_1 | \hat{\hat{\theta}}(\mu = 1, {\rm obs})), \tag{8.4}$$

and the other describes the BG-only (null) hypothesis:

$$p_0 \equiv 1 - \int_{\widetilde{q}_1^{\rm obs}}^{\infty} d\widetilde{q}_0 \; f(\widetilde{q}_0 | \hat{\hat{\theta}}(\mu = 0, {\rm obs})). \tag{8.5}$$

Finally, the modified CL_s p-value is defined to be

$$CL_s \equiv \frac{p_1}{1 - p_0}, \tag{8.6}$$

and new physics models with $CL_s \leq 0.05$ are excluded at $\geq$95% CL. A contour can be drawn through such models to obtain the observed limit.

Expected limits can be generated in a number of ways. The most obvious technique is to simply replace the data observation by the expected BG and repeat the above procedure. The $\pm 1\sigma$ expected error bands are obtained by converting the expected limit at $CL_s = 0.05$ to an equivalent significance using equation 6.1 (which gives ~ 1.64) and then drawing contours through 0.64 and 2.64.

The CL_s prescription is therefore essentially a standard frequentist hypothesis test, but the normalization in equation 8.6 renders it conservative. The normalization provides robustness against cases where the S+BG and BG-only $\widetilde{q}_\mu$ distributions are not well separated—*i.e.* cases where exclusion can occur despite poor sensitivity in a traditional hypothesis test using p_1 only. In these cases p_0 is large, so CL_s becomes large.

Although the above method fixes $\mu = 1$ from the outset, it is also possible to set limits by performing a scan across μ values. A 95% CL upper limit on μ is then obtained for each signal point by finding the value of μ which gives $CL_s = 0.05$. This approach is often used for one-dimensional limits such as those on Higgs boson masses [133]. These limit setting paradigms are equivalent in the sense that they will exclude the same model points, but the $\pm 1\sigma$ bands of course have different meanings.

8.3 Visible Cross Section Limits

Although the SRs have been optimized for sensitivity to particular classes of BSM scenarios, it is possible to interpret the analysis results in a model independent way. As will be explained in the present section, this is achieved by setting limits on the so-called visible cross section.

By scanning input signal yields, a hypothetical signal yield N_S^{exc} which would give $CL_s = 0.05$ can be obtained in each SR. This is interpreted as a model independent 95% CL upper limit on all hypothetical new physics scenarios producing SR events. It is often, however, more convenient to think in terms of cross sections. To this end, the N_S limit can readily be translated to a limit on the so-called BSM visible cross section: $\sigma_V^{\text{exc}} = N_S^{\text{exc}}/L$. Results of these calculations are displayed in table 8.2.

Table 8.2: Expected and observed 95% CL upper limits on the visible cross section and equivalent limits on signal yields are shown in each SR.

	SRnoZa	SRnoZb	SRnoZc	SRnoZd	SRZa	SRZb	SRZc
Expected Events	96 ± 19	29 ± 6	4.4 ± 1.8	1.06±0.74	249 ± 35	22 ± 5	6.3 ± 1.5
Observed Events	101	32	5	2	273	23	6
p_0-value	0.41	0.37	0.40	0.22	0.23	0.44	0.5
N_S^{exc} (exp)	39.3	16.3	6.2	2.9	67.9	13.2	6.7
N_S^{exc} (obs)	41.8	18.0	6.8	4.4	83.7	13.9	6.5
σ_V^{exc} (exp) [fb]	1.90	0.79	0.30	0.14	3.28	0.64	0.32
σ_V^{exc} (obs) [fb]	2.02	0.87	0.33	0.21	4.04	0.67	0.31

Note that the visible cross section is related to the cross section of a given signal model by folding in the acceptance and efficiency for that model: $\sigma_V = A \times \epsilon\sigma_S$. The acceptance is defined to be the efficiency of all fiducial cuts (*i.e.* cuts applied to truth- and parton-level physics objects), whereas ϵ is the efficiency of all reconstruction-level cuts applied to events and objects passing the fiducial cuts. In this language, $A \times \epsilon$ is then the overall efficiency of an event selection. As an example, $A \times \epsilon \sim 5\%$ in the SIM via $\widetilde{\ell}$ bulk. This provides two additional interpretations of the observed limit contours: They can be thought of as contours drawn through $N_S = N_S^{\text{exc}}$ or through $\sigma_S = \sigma_V^{\text{exc}}/(A \times \epsilon)$.

8.4 MUED Interpretation

Figure 8.4 displays the expected and observed 95% CL limits on the MUED parameter space in SRnoZd. Also shown are the $\pm 1\sigma$ contours resulting from up- and downward fluctuation of the theory uncertainties on the MUED signal. As a conservative convention, the observed limit is taken to be the $+1\sigma$ theory uncertainty curve. All contours are obtained by linear interpolation from the underlying discrete grid. The full map of CL_s values can be found in appendix B.

Compactification scales $\lesssim$ 950 GeV are excluded at moderate to high ΛR, and the expected limit reaches past 1 TeV. At the time of this writing, this is the most stringent experimental MUED limit in existence.

8.5 SUSY Interpretations

The 95% CL limits on the SIM via WZ and via $\widetilde{\ell}$ parameter spaces are shown in figure 8.5. Full CL_s maps are available in appendix B. Both limits have been set using a statistical combination of SRnoZa, b, c, and all SRZ-type regions.

The via WZ ($\widetilde{\ell}$) limit extends as high as $m_{\widetilde{\chi}^{\pm,0}_{1,2}}$ ~600 (310) GeV. By comparing these results to the blue curves in figure 8.5, both limits are seen to be considerably more stringent than those obtained from the 13 fb^{-1} version of this analysis [3].

As discussed in chapter 6, the region $\Delta m_{21} \sim m_Z$ is particularly challenging for SIM via WZ sensitivity due to the preponderance of on-shell Z decays. Sensitivity in this region may be improved in future analyses by reducing the granularity of the SR bins.

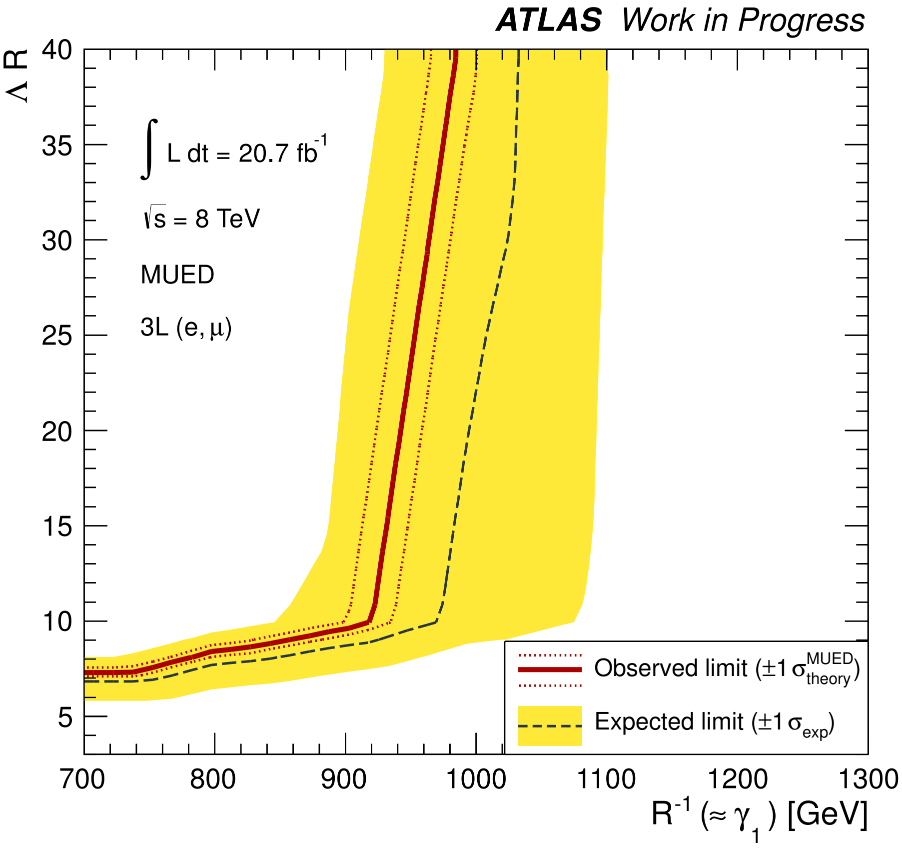

Figure 8.4: 95% CL exclusion limit placed on the MUED parameter space.

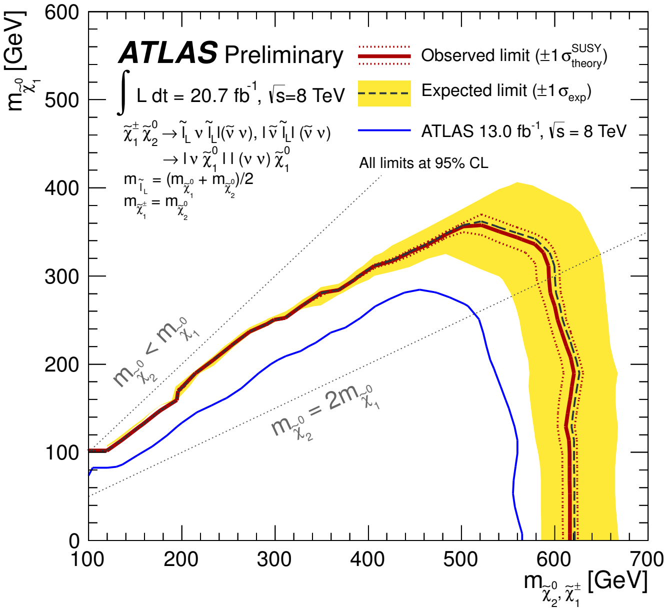

(a) Via $\widetilde{\ell}$

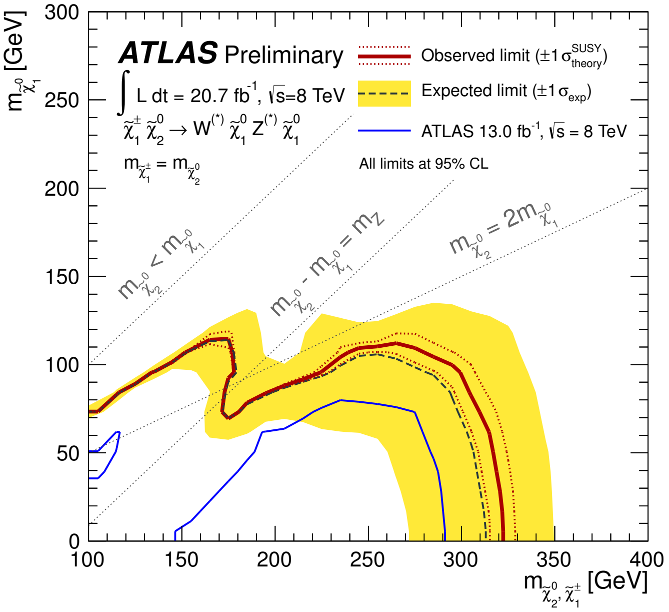

(b) Via WZ

Figure 8.5: 95% CL exclusion limits placed on the SIM via $\widetilde{\ell}$ (a) and via WZ (b) parameter spaces.

Chapter 9

Looking Ahead

At the time of this writing the LHC is being upgraded in preparation for a $\sim$14 TeV run which is set to begin in 2015. This run is projected to collect approximately 100 fb^{-1} by 2017. Another shutdown in 2018 will be used to upgrade the luminosity to roughly 2×10^{34} $\text{cm}^{-2}\text{s}^{-1}$, and a subsequent run until 2022 is expected to collect up to 300 fb^{-1}. A final proposed luminosity upgrade to 5×10^{34} $\text{cm}^{-2}\text{s}^{-1}$ (the so-called High Luminosity LHC) is planned to accrue 3000 fb^{-1} by 2030.

As was explained in chapter 2, MUED's R^{-1} parameter is bounded from above by cosmology: $R^{-1} \lesssim 1.4$ TeV. The limit shown in chapter 8 constrains this parameter from below: $R^{-1} \gtrsim 1$ TeV. This chapter presents a study which assesses the potential of the 14 TeV LHC to either discover MUED or close this 400 GeV gap, thereby simplifying the LHC inverse problem. Detailed 14 TeV studies for SUSY have already been performed by ATLAS [134].

A 14 TeV MUED grid was simulated with Herwig++, and the resulting cross sections are compared to their 8 TeV values in figure 9.1. It is seen that the 14 TeV cross section increases by at least an order of magnitude with respect to 8 TeV. The 14 TeV grid extends up to R^{-1} =1.8 TeV.

Using the approximate p_β-value of equation 6.3, an expected SRnoZd limit for MUED with 20.7 fb^{-1} of 14 TeV collisions is shown in figure 9.2. Several additional approximations have been used to obtain this limit. For simplicity, the background is assumed to be comprised entirely of the leading WZ and $t\bar{t}$ contributions. All quantities entering the WZ object and event selections are purely MC truth-level, but they have been smeared to match the various subdetector resolutions. The $t\bar{t}$ yield has been obtained by scaling the 8 TeV yield by the ratio of HATHOR–derived NNLO cross sections: $\sigma_{14\text{TeV}}/\sigma_{8\text{TeV}} \sim 4.1$. The total expected BG is 14 events, and a total uncertainty of 30% is assumed for the purpose of computing the significance. Despite these approximations, it is clear that 14 TeV analyses will be able to exclude MUED at the 95% CL with $\lesssim$21 fb^{-1} of data.

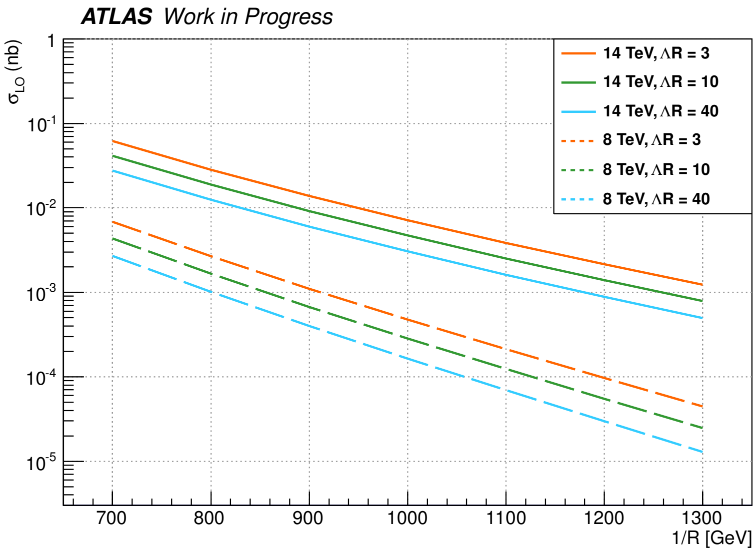

Figure 9.1: LO Herwig++ cross section comparison for MUED at 8 and 14 TeV. Note that a trilepton generator filter efficiency ∼5% has not been applied here.

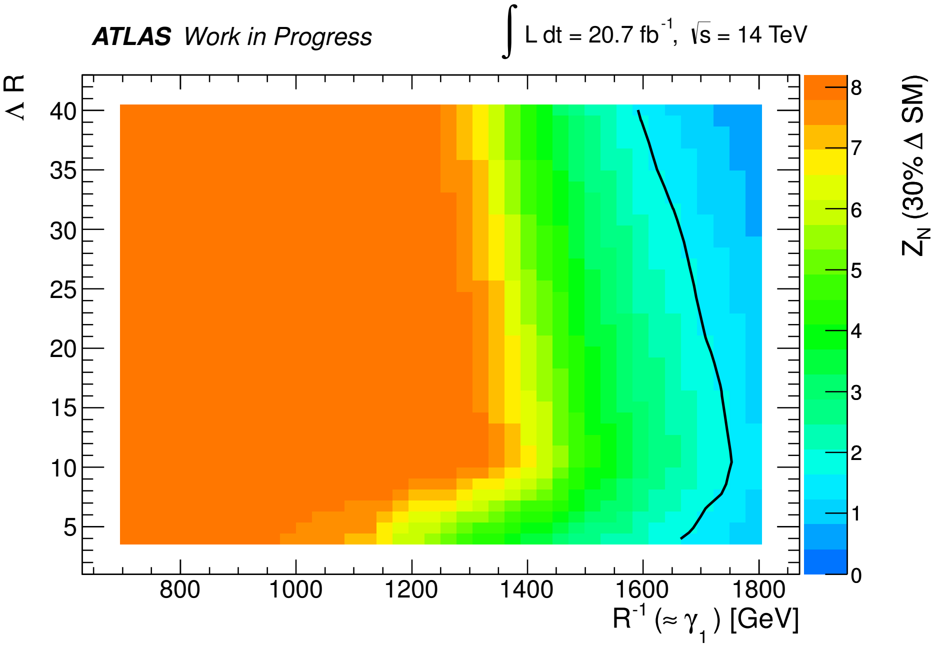

Figure 9.2: Approximate expected sensitivity to MUED with 20.7 fb^{-1} of 14 TeV collisions. The black contour indicates the 95% CL limit.

Chapter 10

Conclusion

The 20.7 fb^{-1} 2012 ATLAS dataset has been used to perform a search for EW SUSY and MUED in final states with three leptons and missing transverse momentum. No significant excess was observed in seven optimized signal regions. These null results were translated into 95% CL limits on the parameter spaces of SIM and MUED.

The MUED limit excludes orbifold compactification scales below ~950 GeV; this is the most stringent existing lower bound on the high ΛR regime of this model. WMAP data place an upper bound $R^{-1} \lesssim 1.4$ TeV. Preliminary studies were presented which suggest that sensitivity to scales up to ~1.7 TeV will be possible early in the 14 TeV LHC run.

SIM interpretations have been presented which constrain scenarios featuring direct production of weak gauginos in both light and heavy slepton regimes. The SIM via $\widetilde{\ell}$ (WZ) limit excludes lightest chargino and next-to-lightest neutralino masses as large as ~600 (310) GeV. Sensitivity past 1 TeV is expected in the $3\ell + \not{E}_T$ channel from the upcoming 14 TeV run [134].

Improvements to this analysis could conceivably be made by smoothing the SR bin granularity. This may enhance sensitivity to small and intermediate mass splitting regimes. Such scenarios include the low ΛR MUED region and the $\Delta m_{21} \sim m_Z$ SIM via WZ region. A natural extension of this work would be to include SRs which are sensitive to hadronic τ decays; this is currently under study by ATLAS. These improvements, however, would be minor ($\lesssim$100 GeV). Significant improvement over the results in this dissertation will be facilitated by increasing the CM energy of the LHC to 14 TeV.

Bibliography

[1] The ATLAS Collaboration. Search for supersymmetry in events with three leptons and missing transverse momentum in $\sqrt{s} = 7$ TeV pp collisions with the ATLAS detector. *Phys. Rev. Lett.*, 108:261804, 2012. → pages iii, 2, 74

[2] The ATLAS Collaboration. Search for direct production of charginos and neutralinos in events with three leptons and missing transverse momentum in $\sqrt{s} = 7$ TeV pp collisions with the ATLAS detector. *Phys. Lett. B*, 718:841, 2013. → pages iii, 2

[3] The ATLAS Collaboration. Search for direct production of charginos and neutralinos in events with three leptons and missing transverse momentum in 13.0 fb^{-1} of pp collisions at $\sqrt{s} = 8$ TeV with the ATLAS detector. *ATLAS-COM-CONF-2012-192*, 2012. → pages iii, 2, 128

[4] The ATLAS Collaboration. Search for direct production of charginos and neutralinos in events with three leptons and missing transverse momentum in 21 fb^{-1} of pp collisions at $\sqrt{s} = 8$ TeV with the ATLAS detector. *ATLAS-CONF-2013-035*, 2013. → pages iii, 2

[5] The ATLAS Collaboration. Search for direct production of charginos and neutralinos in events with three leptons and missing transverse momentum in $\sqrt{s} = 7$ TeV pp collisions with the ATLAS detector. *ATLAS-CONF-2012-077*, 2012. → pages iii

[6] ATLAS Collaboration. Observation of a new particle in the search for the Standard Model Higgs boson with the ATLAS detector at the LHC. *Phys. Lett. B*, 716:1, 2012. → pages 1, 5

[7] CMS Collaboration. Observation of a new boson at a mass of 125 GeV with the CMS experiment at the LHC. *Phys. Lett. B*, 716:30, 2012. → pages 1, 5

[8] D. Morrissey *et al.* Physics searches at the LHC. *Phys. Rept.*, 515:1, 2012. → pages 1

[9] C. Lin. Search for universal extra dimensions in the multi-lepton channel at the Tevatron. *CDF/THESIS/EXOTIC/PUBLIC/7980*, 2005. → pages 2, 18

[10] The ATLAS Collaboration. Search for squarks and gluinos with the ATLAS detector in final states with jets and missing transverse momentum and 20.3 fb^{-1} of $\sqrt{s} = 8$ TeV proton-proton collision data. *ATL-COM-PHYS-2012-1816*, 2012. → pages 2

[11] The ATLAS Collaboration. Search for supersymmetry with compressed mass spectra in events involving soft-leptons, jets plus missing transverse momentum at $\sqrt{s} = 8$ TeV. *ATL-COM-PHYS-2013-061*, 2013. → pages 2

[12] G. Belanger *et al.* Dark matter in UED: the role of the second KK level. *1012.2577*, 2010. → pages 2, 16

[13] A. Canepa. Search for chargino and neutralino at run II of the Tevatron collider. *CDF/THESIS/EXOTIC/PUBLIC/7980*, 2006. → pages 3

[14] The CMS Collaboration. Search for electroweak production of charginos, neutralinos, and sleptons using leptonic final states in pp collisions at 8 TeV. *CMS-PAS-SUS-13-006*, 2013. → pages 3

[15] The ATLAS Collaboration. Search for direct-slepton and direct-chargino production in final states with two opposite-sign leptons, missing transverse momentum and no jets in 20 fb^{-1} of pp collisions at $\sqrt{s} = 8$ TeV with the ATLAS detector. *ATLAS-CONF-2013-049*, 2013. → pages 3

[16] The ATLAS Collaboration. Search for electroweak production of supersymmetric particles in final states with at least two hadronically decaying taus and missing transverse momentum with the ATLAS detector in proton-proton collisions at $\sqrt{s} = 8$ TeV. *ATLAS-CONF-2013-028*, 2013. → pages 3

[17] The ATLAS Collaboration. Search for supersymmetry in events with four or more leptons in 21 fb^{-1} of pp collisions at $\sqrt{s} = 8$ TeV with the atlas detector. *ATLAS-CONF-2013-036*, 2013. → pages 3

[18] The LEP Collaborations. Combined LEP chargino results. *LEPSUSYWG/01-03.1, LEPSUSYWG/02-04.1*, 2000. → pages 3

[19] S. Glashow. Partial symmetries of weak interactions. *Nucl. Phys.*, 22:579, 1961. → pages 4

[20] S. Weinberg. A model of leptons. *Phys. Rev. Lett.*, 19:1264, 1967. → pages 4

[21] http://en.wikipedia.org/wiki/File:Standard_Model_of_Elementary_Particles.svg. Accessed 15/09/13. → pages 4

[22] T2K Collaboration. Evidence of electron neutrino appearance in a muon neutrino beam. *Phys. Rev. D*, 88:032002, 2013. → pages 5

[23] E. Bloom *et al.* High-energy inelastic $e - p$ scattering at 6° and 10°. *Phys. Rev. Lett.*, 23:930, 1969. → pages 5

[24] TASSO Collaboration. Evidence for planar events in e^+e^- annihilation at high energies. *Phys. Lett. B*, 86:243, 1979. → pages 5

[25] G. Arnison *et al.* Experimental observation of isolated large transverse energy electrons with associated missing energy at $s^{1/2} =$ 540 GeV. *Phys. Lett. B*, 122:103, 1983. → pages 5

[26] CDF Collaboration. Observation of top quark production in $p\bar{p}$ collisions with the Collider Detector at Fermilab. *Phys. Rev. Lett.*, 74:2626, 1995. → pages 5

[27] C. Burgess, G. Moore. *The Standard Model: a primer.* Cambridge University Press, 2007. → pages 6, 7

[28] R. Brout F. Englert. Broken symmetry and the mass of gauge vector mesons. *Phys. Rev. Lett.*, 13:321, 1964. → pages 7

[29] P. Higgs. Broken symmetries and the masses of gauge bosons. *Phys. Rev. Lett.*, 13:508, 1964. → pages 7

[30] M. Peskin, D. Schroeder. *An introduction to quantum field theory.* Westview Press, 1995. → pages 7

[31] G. ’t Hooft. Renormalizable Lagrangians for massive Yang-Mills fields. *Nucl. Phys. B*, 35:167, 1971. → pages 7

[32] M. Gell-Mann *et al.* *Supergravity.* North Holland, 1979. → pages 7

[33] F. Zwicky. Die rotverschiebung von extragalaktischen nebeln. *Helvetica Physica Acta*, 6:110, 1933. → pages 8

[34] The Planck Collaboration. Planck 2013 results. I. Overview of products and results. *Submitted to Astronomy and Astrophysics*, 2013. → pages 8

[35] S. Weinberg. Ambiguous solutions of supersymmetric theories. *Phys. Lett. B*, 62:111, 1976. → pages 8

[36] G. Nordstrom. *Z. Phys.*, 15:504, 1914. → pages 9

[37] T. Kaluza. *Math. Phys. K*, 1:966, 1921. → pages 9

[38] O. Klein. *Z. Phys.*, 37:895, 1926. → pages 9

[39] I. Bars *et al.* Gauged duality, conformal symmetry and space-time with two times. *Phys. Rev. D*, 58:066004, 1998. → pages 9

[40] T. Rizzo. Introduction to extra dimensions. *SLAC-PUB*, 14014, 2010. → pages 9

[41] N Arkani-Hamed *et al.* The hierarchy problem and new dimensions at a millimeter. *Phys. Lett. B*, 429:263, 1998. → pages 12

[42] L. Randall, R. Sundrum. A large mass hierarchy from a small extra dimension. *Phys. Rev. Lett.*, 83:3370, 1999. → pages 12

[43] B. Dobrescu *et al.* Bounds on universal extra dimensions. *Phys. Rev. D*, 64:035002, 2001. → pages 13, 17

[44] B. Bhattacherjee. Universal extra dimensions: Violation of Kaluza-Klein parity. *Phys. Rev. D*, 79:016006, 2009. → pages 13

[45] L. Nilse. Classification of 1D and 2D orbifolds. *arXiv:hep-ph/0601015v2*, 2006. → pages 14, 15

[46] C. Macesanu *et al.* Collider implications of universal extra dimensions. *Phys. Rev. D*, 66:015009, 2002. → pages 14, 18

[47] D. Dicus *et al.* Collider implications of Kaluza-Klein excitations of the gluons. *Phys. Rev. D*, 65:076007, 2002. → pages 14

[48] H. Cheng *et al.* Bosonic supersymmetry? Getting fooled at the LHC. *Phys. Rev. D*, 66:056006, 2002. → pages 15, 19

[49] T. Tait G. Servant. Is the lightest Kaluza-Klein particle a viable dark matter candidate? *Nucl. Phys. B*, 650:391, 2003. → pages 15

[50] H. Cheng *et al.* Kaluza-Klein dark matter. *Phys. Rev. Lett.*, 89:211301, 2002. → pages 16

[51] B. Dobrescu, E. Poppitz. Number of fermion generations derived from anomaly cancellation. *Phys. Rev. Lett.*, 87:031801, 2001. → pages 16

[52] T. Applequist *et al.* Neutrinos vis-a-vis the six-dimensional Standard Model. *Phys. Rev. D*, 65:105019, 2002. → pages 16

[53] N. Arkani-Hamed *et al.* Self-breaking of the Standard Model gauge symmetry. *Phys. Rev. D*, 62:096006, 2000. → pages 16

[54] C. Macesanu. The phenomenology of universal extra dimensions at hadron colliders. *Int. J. Mod. Phys.*, A21:2259, 2006. → pages 16

[55] The ATLAS Collaboration. Search for diphoton events with large missing transverse momentum in 7 TeV proton-proton collision data with the ATLAS detector. *Phys. Lett. B*, 718:411, 2012. → pages 16

[56] H. Cheng *et al.* Radiative corrections to Kaluza-Klein masses. *Phys. Rev. D*, 66:036005, 2002. → pages 18, 19

[57] R. Feynman. The behavior of hadron collisions at extreme energies. *High Energy Collisions: Third International Conference at Stony Brook, N.Y.*, page 237, 1969. → pages 20

[58] T. Sjöstrand *et al.* PYTHIA 6.4 physics and manual. *JHEP*, 05:026, 2006. → pages 20, 72

[59] Y.A. Gol'fand, E.P. Likhtman. *JETP Lett.*, 13:323, 1971. → pages 23

[60] D.V. Volkov, V.P. Akulov. *Phys. Lett. B*, 46:109, 1973. → pages 23

[61] J. Wess, B. Zumino. *Nucl. Phys. B*, 70:39, 1974. → pages 23, 26

[62] The ATLAS Collaboration. ATLAS: Detector and physics performance technical design report. Volume 2. *CERN-LHCC-99-15*, 1999. → pages 23, 44

[63] G. Bertone *et al.* Particle dark matter: Evidence, candidates and constraints. *Phys. Rept.*, 405:279, 2005. → pages 23

[64] S. Martin. A supersymmetry primer. *arXiv:hep-ph/9709356v6*, 2011. → pages 23, 31, 33

[65] S. Dimopoulos, H. Georgi. Softly broken supersymmetry and SU(5). *Nucl. Phys. B*, 193:150, 1981. → pages 23

[66] S. Dimopoulos, S. Raby. *Nucl. Phys. B*, 192:353, 1981. → pages 23

[67] E. Witten. *Nucl. Phys. B*, 188:513, 1981. → pages 23

[68] S. Weinberg. *The quantum theory of fields vol. 1: foundations.* Press Syndicate of the University of Cambridge, 1995. → pages 24

[69] L. Ryder. *Quantum field theory.* Cambridge University Press, 1996. → pages 27

[70] V. Kac. Lie superalgebras. *Adv. in Math*, 26:8, 1977. → pages 27

[71] S. Ferrara *et al.* Supergauge multiplets and superfields. *Phys. Lett. B*, 51:239, 1974. → pages 27

[72] M. Kuroda. Complete Lagrangian of MSSM. *arXiv:hep-ph/9902340v3*, 2005. → pages 28

[73] S. Vempati. Introduction to MSSM. *arXiv:hep-ph/0334v1*, 2012. → pages 28

[74] N. Seiberg, K. Intriligator. Lectures on supersymmetry breaking. *Class. Quant. Grav.*, 24:741, 2007. → pages 29

[75] S. Dimopoulos, D. Sutter. The supersymmetric flavor problem. *Nucl. Phys. B*, 452:496, 1995. → pages 29

[76] W. Beenakker *et al.* The production of charginos/neutralinos and sleptons at hadron colliders. *Phys. Rev. Lett.*, 83:3780, 1999. → pages 31, 72

[77] G. Farrar, P. Fayet. Phenomenology of the production, decay, and detection of new hadronic states associated with supersymmetry. *Phys. Lett. B*, 76:575, 1978. → pages 32

[78] H. Goldberg. *Nucl. Phys. B*, 50:1419, 1983. → pages 33

[79] R. Barbier *et al.* R-parity violating supersymmetry. *Phys. Rept.*, 420:1, 2005. → pages 33

[80] S. Dawson. Introduction to the physics of Higgs bosons. *BNL-61012*, 1994. → pages 34

[81] M. Papucci *et al.* Natural SUSY endures. *DESY-11-193*, 2011. → pages 35

[82] J. Alwall *et al.* Simplified models for a first characterization of new physics at the LHC. *Phys. Rev. D*, 79:075020, 2009. → pages 35

[83] N. Arkani-Hamed *et al.* Supersymmetry and the LHC inverse problem. *JHEP*, 0608:070, 2006. → pages 38

[84] G. Moortgat-Pick *et al.* Early spin determination at the LHC? *Phys. Lett. B*, 699:158, 2011. → pages 39

[85] O. Brüning *et al.* LHC design report. *CERN-2004-003-V-1*, 2004. → pages 40, 41

[86] The CMS Collaboration. CMS physics: Technical design report volume 1: Detector performance and software. *CERN-LHCC-2006-001*, 2006. → pages 40

[87] LHC Experiments Committee. LHCb: Technical proposal. *CERN-LHCC-98-004*, 1998. → pages 40

[88] The ALICE Collaboration. The ALICE experiment at the CERN LHC. *JINST*, 3:08002, 2008. → pages 40

[89] http://lhc.web.cern.ch/lhc/LHCUnder.pdf. Accessed 17/09/13. → pages 41

[90] J. Wenninger *et al.* Operation of the LHC at high luminosity and high stored energy. *CERN-ATS-2012-101*, 2012. → pages 41

[91] https://twiki.cern.ch/twiki/bin/view/AtlasPublic/LuminosityPublicResults. Accessed 05/12/13. → pages 41, 73

[92] The ATLAS Collaboration. ATLAS: Detector and physics performance technical design report. Volume 1. *CERN-LHCC-99-14*, 1999. → pages 44

[93] The ATLAS Collaboration. The ATLAS experiment at the CERN Large Hadron Collider. *JINST*, 3:08003, 2008. → pages 44, 45, 46, 47, 49, 50, 52, 55

[94] The ATLAS Collaboration. ATLAS inner detector: Technical design report. Volume 2. *CERN-LHCC-97-17*, 1997. → pages 45, 46

[95] V. Ginzburg, I. Frank. *Zh. Eksp. Teor. Fiz.*, 16:15, 1946. → pages 46

[96] D. Green. *High P_T Physics at Hadron Colliders.* Cambridge University Press, 2005. → pages 50

[97] The ATLAS Collaboration. Performance of the ATLAS trigger system in 2010. *Eur. Phys. J. C*, 72:1849, 2011. → pages 55

[98] The ATLAS Collaboration. Measurement of the inelastic proton-proton cross-section at $\sqrt{s} = 7$ TeV with the ATLAS detector. *Nature Commun.*, 2:463, 2011. → pages 55

[99] https://twiki.cern.ch/twiki/bin/view/AtlasPublic/CombinedSummaryPlots. Accessed 20/09/13. → pages 55

[100] I. Bird *et al.* LHC computing grid. Technical design report. *CERN-LHCC-2005-24*, 2005. → pages 57

[101] The ATLAS Collaboration. Electron performance measurements with the ATLAS detector using the 2010 LHC proton-proton collision data. *Eur. Phys. J C*, 72:1909, 2012. → pages 59, 60, 61

[102] The ATLAS Collaboration. Calorimeter clustering algorithms: Description and performance. *ATLAS-COM-LARG-2008-003*, 2008. → pages 59, 65

[103] The ATLAS Collaboration. Expected performance of the ATLAS experiment: Detector, trigger, and physics. *CERN-OPEN-2008-020*, 2008. → pages 62, 63

[104] The ATLAS Collaboration. Preliminary results on the muon reconstruction efficiency, momentum resolution, and momentum scale in ATLAS 2012 *pp* collision data. *ATLAS-CONF-2013-088*, 2013. → pages 63

[105] https://twiki.cern.ch/twiki/bin/viewauth/AtlasProtected/QualityDefinitionStaco. Accessed 25/09/13. → pages 64

[106] M. Cacciari *et al.* The anti-k_t jet clustering algorithm. *JHEP*, 0804:063, 2008. → pages 66

[107] S. Ellis, D. Soper. Successive combination jet algorithm for hadron colliders. *Phys. Rev. D*, 48:3160, 1993. → pages 66

[108] The ATLAS Collaboration. ATLAS calorimeter response to single isolated hadrons and estimation of the calorimeter jet scale uncertainty. *ATLAS-CONF-2010-052*, 2010. → pages 66

[109] D. Miller *et al.* Pile-up jet energy scale corrections using the jet-vertex fraction method. *ATLAS-COM-PHYS-2009-180*, 2009. → pages 66

[110] The ATLAS Collaboration. Commissioning of the ATLAS high-performance b-tagging algorithms in the 7 TeV collision data. *ATLAS-CONF-2011-102*, 2011. → pages 67

[111] J. Beringer *et al.* (Particle Data Group). *Phys. Rev. D*, 86:010001, 2012. → pages 68, 82

[112] The ATLAS Collaboration. Performance of the missing transverse energy reconstruction and calibration in proton-proton collisions at a center-of-mass energy of 7 TeV with the ATLAS detector. *ATLAS-CONF-2010-057*, 2010. → pages 68

[113] The ATLAS Collaboration. Performance of the missing transverse energy reconstruction in ATLAS with 2011 proton-proton collisions at $\sqrt{s} = 7$ TeV. *ATLAS-COM-PHYS-2012-445*, 2012. → pages 69

[114] The GEANT4 Collaboration. *Nucl. Instrum. Meth. A*, 506:250, 2003. → pages 71

[115] T. Gleisberg *et al.* Event generation with SHERPA 1.1. *JHEP*, 0902:007, 2009. → pages 72

[116] J. Campbell *et al.* Vector boson pair production at the LHC. *JHEP*, 1107:018, 2011. → pages 72

[117] S. Frixione *et al.* Matching NLO QCD computations with parton shower simulations: The POWHEG method. *JHEP*, 0711:070, 2007. → pages 72

[118] M. Aliev *et al.* Hathor hadronic top and heavy quarks cross section calculator. *Compute. Phys. Commun.*, 182:1034, 2011. → pages 72

[119] J. Alwall *et al.* MadGraph 5: Going beyond. *JHEP*, 1106:128, 2011. → pages 72

[120] S. Frixione, B. Webber. The MC@NLO 3.2 event generator. *CERN-PH-TH-2006-012*, 2006. → pages 72

[121] M. Mangano *et al.* The Monte Carlo event geerator AcerMC versions 2.0 to 3.8 with interfaces to PYTHIA 6.4, HERWIG 6.5 and ARIADNE 4.1. *Compute. Phys. Commun.*, 184:919, 2013. → pages 72

[122] H. Lai *et al.* New parton distributions for collider physics. *Phys. Rev. D*, 82:074024, 2010. → pages 72

[123] M. Bahr *et al.* Herwig++ physics and manual. *Eur. Phys. J. C*, 58:639, 2008. → pages 72

[124] J. Linnemann. Measures of significance in HEP and astrophysics. *arXiv:physics/0312059v2*, 2003. → pages 78

[125] The ATLAS Collaboration. Measurement of the top quark pair production cross section with ATLAS in pp collisions at $\sqrt{s} = 7$ TeV. *Eur. Phys. J. C*, 71:1577, 2011. → pages 99

[126] J. Butterworth *et al.* Single boson and diboson production cross sections in pp collisions at $\sqrt{s} = 7$ TeV. *ATL-COM-PHYS-2010-695*, 2010. → pages 107

[127] A. Kardos *et al.* Top quark pair production in association with a Z-boson at NLO accuracy. *Phys. Rev. D*, 85:054015, 2012. → pages 107

[128] G. Khoriauli. Study of systematic uncertainties of single top production at ATLAS. *Nuovo Cim. B*, 123:1327, 2008. → pages 108

[129] The ATLAS Collaboration. Improved luminosity determination in pp collisions at $\sqrt{s} = 7$ TeV using the ATLAS detector at the LHC. *Eur. Phys. J. C*, 73:2518, 2013. → pages 109

[130] A. Read. Presentation of search results: The CLs technique. *J. Phys. G: Nucl. Part. Phys.*, 28:2693, 2002. → pages 119, 123

[131] R. Bruneliere *et al.* Setting exclusion limits in ATLAS supersymmetry searches with a likelihood ratio based method. *ATL-COM-PHYS-2011-004*, 2011. → pages 123

[132] G. Cowan *et al.* Asymptotic formulae for likelihood-based tests of new physics. *Eur. Phys. J. C*, 71:1554, 2011. → pages 124

[133] The ATLAS Collaboration. Procedure for the LHC Higgs boson search combination in Summer 2011. *ATL-PHYS-PUB-2011-011*, 2011. → pages 126

[134] The ATLAS Collaboration. Prospects for benchmark supersymmetry searches at the high luminosity LHC with the ATLAS detector. *ATLAS-PHYS-PUB-2013-011*, 2013. → pages 131, 134

Appendix A

Monte Carlo-Based Background Estimate

A fully Monte Carlo-based BG estimate technique has been used for SRnoZd and for optimization of all SRs. All samples used for this estimate are described in chapter 5. This appendix contains detailed tabulated information about the yields at each stage of the cutflow (tables A.1 through A.3) as well as validation of the method (table A.4).

Note that tables A.1 and A.3 express statistical uncertainties only. These are computed using a Poisson assumption. Each sample contributes a yield

$$N_s = \sum_i^{N_s^p} w_i \pm \sqrt{\sum_j^{N_s^p} w_j^2}, \tag{A.1}$$

where w_i are the MC event weights, and N_s^p events from sample s passed the relevant cuts. The yields and uncertainties are then scaled to their corresponding values at 20.7 fb^{-1} with a factor 20.7 fb^{-1}/L_{MC}, where L_{MC} is the sample luminosity. The "total" entries in the tables are then obtained by adding yields linearly and adding uncertainties in quadrature. A subtlety arises when a cut removes all events from a given sample: Quoting an exactly vanishing error for such a sample is obviously inaccurate. The prescription used here is to report the yield as $0.0^{+1.1}_{-0.0} \times \frac{20.7}{L_{MC}}$, where 1.1 is the parameter of a Poisson distribution for which observing zero events is a 1σ fluctuation. In case of a composite yield, the minimum L_{MC} is conservatively chosen.

Table A.1: MC yield estimates and statistical uncertainties for reducible and irreducible SM backgrounds at all stages of the SRnoZa,b,c cutflows. Note that the small overlap of SRnoZa,b with SRnoZc has not been removed here.

				SRnoZa			**SRnoZb**	**SRnoZc**	
Selection	**3ℓ**	b-veto	Z-veto	$\not{E}_T > 50$ GeV	$m_{\ell\ell} < 60$ GeV	$\not{E}_T > 75$ GeV	$60 < m_{\ell\ell} < 81$ GeV	$m_T > 110$ GeV	$p_T^3 > 30$ GeV
$t\bar{t} + Z$	52.88±1.83	3.71±0.50	0.77±0.20	0.34±0.12	0.18±0.11	0.19±0.09	0.10±0.07	0.16±0.09	0.08±0.06
$t\bar{t} + W$	25.44±1.35	1.43±0.32	1.15±0.29	0.61±0.2	0.1±0.1	0.47±0.18	0.13±0.09	0.13±0.09	0.13±0.09
ZZ	1565.04±10.21	1435.69±9.72	1018.88±8.20	37.8±1.47	13.91±0.88	4.98±0.55	1.86±0.33	0.59±0.19	0.25±0.14
$Tri - boson$	16.27±0.20	11.64±0.17	8.32±0.15	5.49±0.12	1.80±0.07	3.46±0.11	0.76±0.04	1.78±0.07	0.81±0.05
WZ	2399.69±16.31	2044.15±14.91	404.39±6.60	152.82±4.05	50.11±2.28	60.11±2.54	20.03±1.49	8.67±0.94	2.12±0.44
Σ SM irreducible	4059.32±19.37	3496.63±17.81	1433.52±10.54	197.04±4.31	66.10±2.45	69.21±2.61	22.9±1.53	11.33±0.98	3.40±0.47
$t\bar{t}$	249.53±5.73	51.45±2.64	42.72±2.41	25.67±1.85	10.46±1.18	14.79±1.41	4.26±0.75	4.43±0.77	0.6±0.3
t	14.29±2.55	10.13±2.18	7.27±1.86	4.11±1.42	0.32±0.78	1.23±0.92	0.2±0.2	0.00±0.29	0.00±0.29
WW	6.8±0.64	4.06±0.48	3.61±0.46	1.71±0.32	0.55±0.18	0.83±0.22	0.15±0.1	0.35±0.14	0.07±0.04
$Z + LF$	2223.53±95.81	2051.53±91.63	1184.67±69.08	29.52±10.08	13.09±6.96	0.00±9.87	0.00±9.87	0.00±9.87	0.00±9.87
$Z + HF$	600.5±28.86	448.27±24.95	91.02±10.4	6.28±2.5	0.85±0.85	0.00±1.44	0.00±1.44	0.00±1.44	0.00±1.44
$W + j$	0.0±0.00023	0.0±0.00023	0.0±0.00023	0.0±0.00023	0.0±0.00023	0.0±0.00023	0.0±0.00023	0.0±0.00023	0.0±0.00023
Σ SM reducible	3094.65±100.26	2565.45±95.03	1329.30±69.92	67.28±10.65	25.27±7.15	16.85±10.07	4.61±9.97	4.78±10.01	0.67±9.98
Total Bkg.	7153.97±102.12	6062.07±96.69	2762.81±70.71	264.32±11.49	91.38±7.56	86.07±10.40	27.51±10.08	16.12±10.08	4.07±9.99
sm sleptons 500,0	28.5±0.5	24.9±0.4	24.1±0.4	23.2±0.4	0.7±0.1	22.1±0.4	0.7±0.1	19.2±0.4	18.4±0.4
Z_N (15% ΔSM)	0.03	0.03	0.06	0.5	0.0	1.4	0.0	3.4	5.7
sm Z, W 250,0	40.0±0.7	36.4±0.7	2.0±0.2	1.7±0.2	0.3±0.1	1.4±0.1	0.8±0.1	0.8±0.1	0.4±0.1
Z_N (15% ΔSM)	0.04	0.04	0.01	0.03	0.0	0.1	0.0	0.0	0.0

Table A.2: MC yield estimates and statistical uncertainties for reducible and irreducible SM backgrounds at all stages of the SRnoZd cutflow.

							SRnoZd
Selection	3ℓ	SFOC	b-veto	Z-veto	$\not{E}_T$ >120 GeV	20< $m_{\ell\ell}$ <81 GeV	N_j ≥3
$t\bar{t}+Z$	52.88±1.83	51.54±1.81	3.71±0.50	0.77±0.20	0.08±0.06	0.08±0.06	0.00±0.05
$t\bar{t}+W$	25.44±1.35	19.53±1.19	1.43±0.32	1.15±0.29	0.30±0.15	0.06±0.06	0.06±0.06
ZZ	1565.04±10.21	1559.05±10.19	1435.69±9.72	1018.88±8.20	0.60±0.19	0.34±0.14	0.07±0.06
$Triboson$	16.27±0.20	12.72±0.17	11.64±0.17	8.32±0.15	1.06±0.05	0.46±0.030	0.009±0.004
WZ	2399.69±16.31	2385.01±16.25	2044.15±14.91	404.39±6.60	15.06±1.28	6.55±0.82	0.35±0.02
Σ SM irreducible	4059.32±19.37	4027.85±19.31	3496.63±17.81	1433.52±10.54	17.1±1.3	7.49±0.84	0.49±0.10
$t\bar{t}$	249.53±5.73	189.87±5.01	51.45±2.64	42.72±2.41	3.42±0.68	2.41±0.57	0.57±0.30
t	14.29±2.55	13.22±2.49	10.13±2.18	7.27±1.86	0.0±0.3	0.0±0.3	0.0±0.3
WW	6.80±0.64	5.38±0.57	4.06±0.48	3.61±0.46	0.31±0.14	0.0±0.1	0.0±0.1
$Z+LF$	2223.53±95.81	2214.40±95.59	2051.53±91.63	1184.67±69.08	0.00±0.01	0.00±0.01	0.00±0.01
$Z+HF$	600.50±28.86	599.02±28.84	448.27±24.95	91.02±10.40	0.0±0.1	0.0±0.1	0.0±0.1
$W+j$	0.0±0.00023	0.0±0.00023	0.0±0.00023	0.0±0.00023	0.0±0.00023	0.0±0.00023	0.0±0.00023
Σ SM reducible	3094.65±100.26	3021.89±100.01	2565.45±95.03	1329.30±69.92	3.73±0.76	2.41±0.66	0.57±0.44
Tot BG	7153.97±102.12	7049.74±101.85	6062.07±96.69	2762.81±70.71	20.83±1.51	9.90±1.07	1.06±0.45

Table A.3: MC yield estimates and statistical uncertainties for reducible and irreducible SM backgrounds at all stages of the SRZ-type cutflows.

			SRZa	**SRZb**	**SRZc**	
Selection	Z req.	75< $\not{E}_T$ <120 GeV	m_T <110 GeV	m_T >110 GeV	$\not{E}_T$ > 120 GeV	m_T >110 GeV
$t\bar{t}+Z$	2.9±0.5	0.53±0.19	0.43±0.17	0.10±0.09	0.51±0.20	0.10±0.10
$t\bar{t}+W$	0.27±0.14	0.12±0.09	0.00±0.05	0.12±0.09	0.004±0.004	0.004±0.004
ZZ	417±5	9.8±0.8	8.9±0.8	0.95±0.25	2.0±0.4	0.39±0.16
$Tri-boson$	3.33±0.08	0.97±0.04	0.536±0.032	0.433±0.029	0.549±0.026	0.290±0.018
WZ	1640±13	254±5	235±5	18.7±1.4	77.8±2.9	5.0±0.7
Σ SM irreducible	2063±14	265±5	245±5	20.3±1.4	80.9±2.9	5.8±0.7
$t\bar{t}$	8.7±1.1	2.7±0.6	2.2±0.5	0.46±0.27	0.58±0.25	0.24±0.17
t	2.9±1.1	1.0±0.7	1.0±0.7	0.00±0.29	0.00±0.29	0.00±0.29
WW	0.45±0.14	0.06±0.05	0.06±0.05	0.00±0.05	0.07±0.05	0.05±0.05
$Z+LF$	867±60	16±8	8±5	8±6	0±4	0±4
$Z+HF$	357±23	0.0±1.4	0.0±1.4	0.0±1.4	0.00±1.4	0.00±1.4
$W+j$	0.00±0.00023	0.00±0.00023	0.00±0.00023	0.00±0.00023	0.00±0.00023	0.00±0.00023
Σ SM reducible	1236±64	20±8	11±6	9±6	0.7±4.2	0.30±4.18
Total Bkg.	3299±66	285±10	256±8	29±6	82±5	6±4
sm sleptons 500,0	0.8±0.1	0.06±0.02	0.008±0.007	0.05±0.02	0.7±0.1	0.7±0.1
Z_N (15% ΔSM)	0.0	0.0	0.01	0.0	0.0	0.0
sm Z,W 250,0	34.4±0.7	9.2±0.4	4.7±0.3	4.6±0.3	17.7±0.5	12.0±0.4
Z_N (15% ΔSM)	0.1	0.2	0.1	0.5	1.1	3.6

Table A.4: Validation region predictions compared to data observations. Errors are statistical and systematic.

Selection	VRnoZa	VRnoZb	VRZa	VRZb
Triboson	1.4±1.4	0.5±0.5	0.6±0.6	0.26±0.27
ZZ	128±87	4.5±2.8	108±23	6.9±2.2
$t\bar{t}V$	2.9±1.2	21±7	7.4±2.6	26±8
WZ	110±21	34±15	545±89	138±38
Σ SM irreducible	242±90	60±16	662±92	171±39
$t\bar{t}$	25±4	78±8	7.7±1.4	13.3±2.22
t	1.6±1.1	2.0±0.9	0.7±0.8	0.6±0.9
WW	0.63±0.26	0.96±0.32	0.06±0.15	0.18±0.17
$V+j$	168±58	4±4	294±69	15±6
Σ SM reducible	195±58	84±10	302±69	29±7
Σ SM	437±107	145±19	964±115	200±40
Data	463	141	1131	171

Appendix B

Complete CL_s Maps

The limit contours shown in chapter 8 are isolines drawn through $CL_s = 0.05(\pm 1\sigma)$. Complete sets of observed CL_s values are shown for SIM in figure B.1 and for MUED in figure B.2. Values between grid points are obtained with linear interpolation.

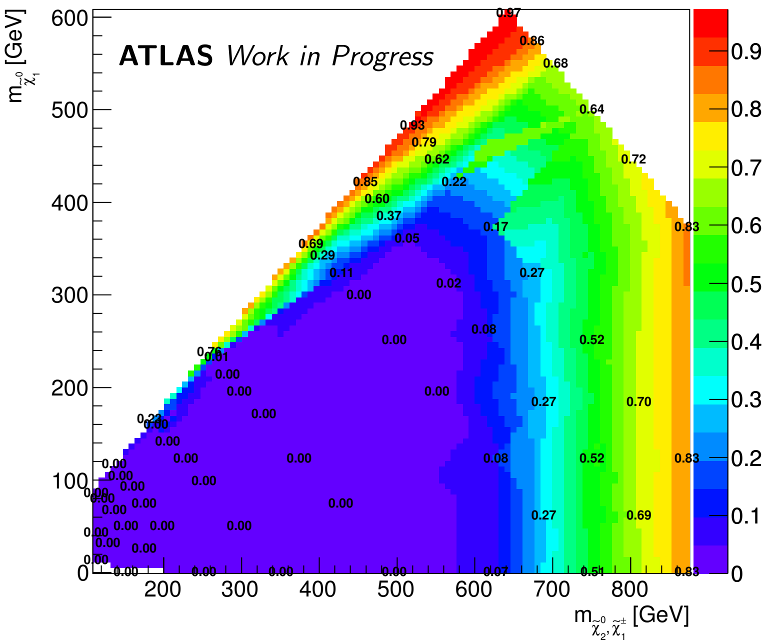

(a) SIM via $\widetilde{\ell}$

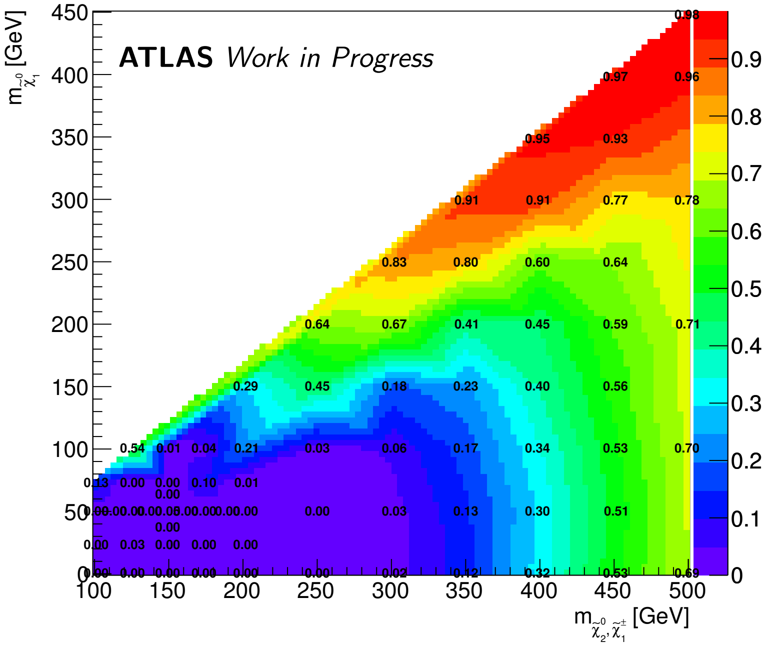

(b) SIM via WZ

Figure B.1: Observed CL_s values across both SIM grids.

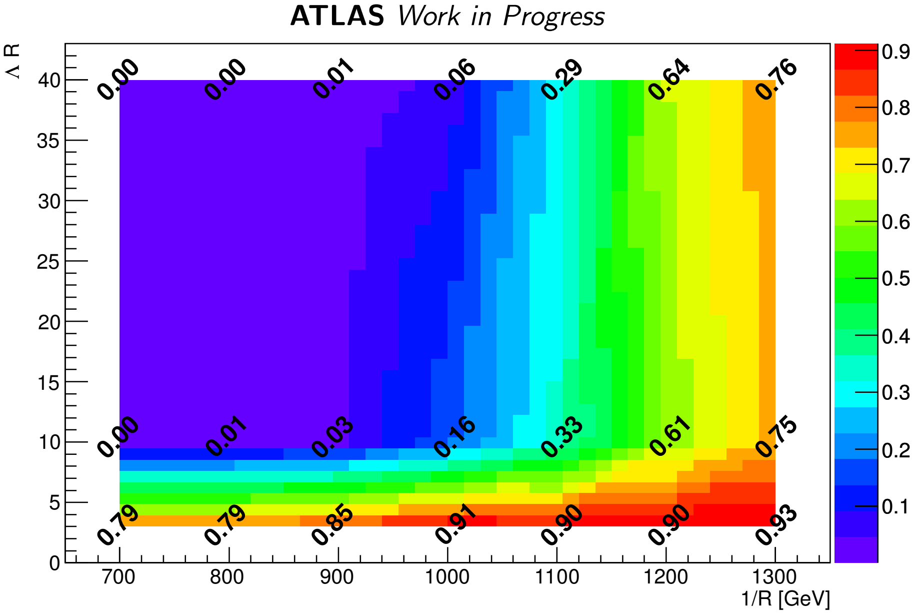

Figure B.2: Observed CL_s values across the MUED grid.